

The Pennsylvania State University
Department of Materials Science and Engineering

**THE INFLUENCE OF CLAMPING AND RESIDUAL STRESS ON SCALING EFFECTS
IN $\text{Pb}(\text{Zr}_{0.3}\text{Ti}_{0.7})\text{O}_3$ THIN FILMS FOR PIEZOMEMS APPLICATIONS**

A Dissertation in
Your Graduate Major
by
Lyndsey M. Denis

© 2019 Lyndsey M. Denis

Submitted in Partial Fulfillment
of the Requirements
for the Degree of

Doctor of Philosophy

August 2019

The dissertation of Lyndsey M. Denis was reviewed and approved* by the following:

Susan Trolier-McKinstry
Professor of Ceramic Science and Engineering and Electrical Engineering
Dissertation Advisor
Chair of Committee

Clive Randall
Professor of Materials Science and Engineering

Roman Engel-Herbert
Associate Professor of Materials Science and Engineering, Chemistry, and Physics

Michael Lanagan
Professor of Engineering Science and Mechanics

Jacob Jones
Special Member
Professor of Materials Science and Engineering
North Carolina State University

Suzanne Mohny
Professor of Materials Science and Engineering and Electrical Engineering
Chair, Intercollege Graduate Degree Program in Materials Science and Engineering

*Signatures are on file in the Graduate School

Abstract

Ferroelectric thin films such as lead zirconate titanate (PZT) have high dielectric and piezoelectric properties which can be utilized in actuators, sensors, transducers, and energy harvesters in microelectromechanical systems (MEMS). A small film thickness enables low voltage operation of such devices; however, property degradation limits the extent that the film thickness can be reduced while maintaining performance. This dissertation describes the impact that different electrical and mechanical boundary conditions have on the dielectric properties of PZT thin films for a variety of thicknesses (ranging from 0.27 to 1.11 μm). Specifically, variations in elastic layer thickness, substrate clamping, residual stress and domain state were investigated. A novel approach to quantitatively deconstruct the relative permittivity into three contributions (intrinsic, reversible extrinsic and irreversible extrinsic) was developed using a combination of X-ray diffraction and Rayleigh analysis. This work aims to determine which factors are associated with scaling effects in tetragonal $\{001\}$ textured $\text{Pb}_{0.99}(\text{Zr}_{0.3}\text{Ti}_{0.7})_{0.98}\text{Nb}_{0.02}\text{O}_3$ (PZT 30/70) thin films.

It is generally accepted that scaling effects play a key role in the suppression of ferroelectric responses in thin films ($< 1 \mu\text{m}$), though the type and extent of this contribution is still debated. Scaling effects refer to the size-induced degradation of properties at length scales exceeding those associated with the ferroelectric stability limit. For a blanket PZT 30/70 film clamped to a Si substrate, the thickness dependence of the irreversible and reversible Rayleigh coefficients was investigated using Rayleigh analysis. The irreversible Rayleigh coefficient was found to be thickness dependent. By

partially releasing the films from the substrate, the suppression of extrinsic contributions to the relative permittivity was alleviated. A greater increase in the irreversible Rayleigh coefficient was observed for thicker films (1.11 μm) compared to thinner films (0.56 μm – 0.27 μm). Therefore, substrate clamping contributes to scaling effects. After the films were partially declamped from the substrate, the irreversible contributions increased up to 23% in Nb-doped films and became more frequency-dependent (by up to 29%).

Defects in a low-dielectric, Mn-doped seed layer also suppressed the extrinsic as well as the intrinsic contributions to the relative permittivity and contributed to the observed thickness dependence in the irreversible and reversible Rayleigh coefficients. The influence of the seed layer on dielectric properties was accounted for using a capacitor in series model. The suppressed frequency dependence in the clamped films was attributed to the pinning of irreversible domain walls active at lower frequencies. Both the seed layer and substrate clamping contributed to the pinning of irreversible domain walls.

The thickness dependence of intrinsic and extrinsic contributions to the dielectric properties was elucidated from a combination of X-ray diffraction and Rayleigh analysis. *In situ* synchrotron X-ray diffraction was used to understand the influence of residual stress and substrate clamping on the domain state, ferroelastic domain reorientation and electric-field-induced strain in PZT 30/70 thin films. A thickness-dependent in-plane tensile stress developed in clamped, blanket PZT films during processing which dictates the domain structure even after poling. Defects and thermal stresses contribute to the greater in-plane tensile stress in the thinner films, resulting in this thickness dependence.

However, after the films were partially de-clamped from the substrate and annealed, the residual stress was alleviated. As a result, the thickness dependence of the volume fraction of *c*-domains largely disappeared, and the out-of-plane *d*-spacings for both *a* and *c*-domains increased in the thinnest film.

By poling the films, irreversible changes in the domain state and domain structure were induced as a result of 90° domain reorientation, domain coarsening, and lattice strain. Upon poling, thicker films experienced a greater coarsening of *c*-domains which resulted in reduced domain wall densities and a larger change in the reversible Rayleigh coefficient. The volume fraction of *c*-domains was used to calculate the intrinsic relative permittivity; the reversible Rayleigh coefficient was then used to separate the intrinsic and the reversible extrinsic contributions. The reversible extrinsic response contributed to more than 70% of the overall relative permittivity and was thickness dependent even after poling and upon release.

Some PiezoMEMS devices, such as cantilevers and fixed-fixed beams, operate in a partially released state. For these devices, the thickness of the passive layer is known to tune the rigidity, deflection and resonance frequency for tailored device performance. However, as the rigidity of the device increases, at some point the ferroelastic response of the active layer will be suppressed. Therefore, the influence of passive layer thickness on the performance of the active layer is of interest.

The deflection of cantilevers and fixed-fixed beams with a tetragonal {001} PZT 30/70 active layer and a SiO₂ elastic layer in an IrO₂/PZT/PbTiO₃/Pt/TiO₂/SiO₂ device stack was characterized experimentally and by finite element modeling. Differences in

the magnitude of the tip displacement were attributed to the variances in rigidity of the device stack associated with different SiO₂ thicknesses. It was found that bending of the cantilevers was dictated by the competing integrated stresses of the IrO₂ top electrode and the SiO₂ elastic layer. Upon release, the PZT films showed increased reversible Rayleigh coefficients but decreased irreversible Rayleigh coefficients, regardless of SiO₂ thickness (2.035 and 0.76 μm), for both cantilever and fixed-fixed beam geometries. These data suggest that upon release, at least some of the domain walls transition from irreversible to reversible motion. For cantilevers and fixed-fixed beams with the thinner SiO₂ layers, the electroded PZT region deflected downward, placing PZT under further in-plane tension. This was correlated with a further decrease in the irreversible and reversible domain wall motion contributions to the relative permittivity.

TABLE OF CONTENTS

List of Figures.....	x
List of Tables	xvi
Acknowledgements	xvii
Chapter: 1 Introduction and Background.....	1
1.1 Piezoelectrics	1
1.2 Ferroelectrics	2
1.3 Lead Zirconate Titanate	4
1.4 Ferroelectric Domain Structure and Formation	5
1.5 Rayleigh Analysis.....	7
1.6 X-ray Diffraction	9
1.7 Residual Stresses in Thin Films.....	12
1.8 Scaling Effects.....	13
Chapter: 2 Thickness Dependent Response of Domain Wall Motion in Declamped {001} Pb(Zr_{0.3}Ti_{0.7})O₃ Thin Films	17
2.1 Introduction	17
2.2 Experimental Procedure.....	20
2.2.1 Film Synthesis and Nanofabrication	20
2.2.2 Characterization.....	25
2.2.3 Capacitor in Series Model	27
2.3 Results	29
2.3.1 Thickness Dependence of Polarization Hysteresis in Declamped Films.....	29
2.3.2 Irreversible Contributions to Permittivity	31
2.3.2.1 Thickness Dependence in Clamped Films	31
2.3.2.2 Thickness Dependence in Released Films	33
2.3.3 Frequency Dependence of α_ϵ	35
2.3.4 Intrinsic and Reversible Contributions to Permittivity.....	36
2.3.4.1 Thickness Dependence in Clamped Films	36
2.3.4.2 Thickness Dependence of Released Films	37
2.3.5 Frequency Dependence of $\epsilon_{\text{initial}}$	38
2.4 Discussion.....	40

2.4.1	Capacitor-in-Series Model.....	40
2.4.2	Substrate Clamping Effects	42
2.5	Conclusions	43
Chapter: 3 Residual Stress and Ferroelastic Domain Reorientation in Declamped {001} Pb(Zr_{0.3}Ti_{0.7})O₃ Films.....		44
3.1	Introduction	44
3.2	Experimental Procedure.....	47
3.2.1	Film Synthesis and Nanofabrication	47
3.2.2	X-ray Measurements and Analysis.....	49
3.3	Results and Discussion	53
3.3.1	Thickness Dependence of the Domain State	53
3.3.2	Thickness Dependence of Residual Stress	57
3.3.3	Rayleigh poling study.....	67
3.4	Conclusions	73
Chapter: 4 Influence of Elastic Layer Thickness on Mechanical and Ferroelastic Behavior of PiezoMEMS Beams		75
4.1	Introduction	75
4.2	Fabrication.....	79
4.3	Modeling.....	82
4.4	Characterization.....	83
4.5	Results and Discussion	84
4.5.1	Influence of Stress and Thickness on Cantilever Tip Deflection	84
4.5.2	FEA Modeling of Cantilever Tip Deflection.....	87
4.5.3	Influence of Etch Process on Fixed-Fixed Beam Buckling.....	92
4.5.4	Impact of Nanofabrication and Tip Deflection on Electrical Properties	95
4.6	Conclusions	100
Chapter: 5 Conclusions		102
Chapter: 6 Future Work		107
6.1	Depth Profiling using X-ray Diffraction.....	107
6.1.1	Glancing-incidence X-ray Diffraction.....	107
6.1.2	X-ray Nanodiffraction	111
6.1.3	In Situ X-ray Microscopy	113
6.2	Application of Relative Permittivity Deconstruction	115

6.2.1	Assessing the Possibility of a Critical Film Thickness.....	115
6.2.2	Permittivity Deconstruction for Various Compositions	116
6.3	TEM Analysis of Domain Structure	117
6.4	Detecting Dead-layers using Curie-Weiss Behavior	117
References.....		119
Appendix.....		145
	Matlab Codes for Data Processing	145
A.1.	Capacitor in Series Seed Layer Correction.....	145
A.2.	Rayleigh Analysis for Large Frequency Sweeps.....	148
A.3.	File Conversion to Matlab Files from .diel.....	150

List of Figures

- Figure 1-1:** A comparison of the cubic paraelectric phase and tetragonal ferroelectric phase of the perovskite crystal structure ABO_3 . The displacement is exaggerated for clarity.3
- Figure 1-2:** The $PbTiO_3$ - $PbZrO_3$ binary sub-solidus phase diagram with an overlay comparison of the dielectric constant (K) vs. mole % of $PbTiO_3$ measured at room temperature, adapted from B. Jaffe *et al.*[15] A maximum in K is observed near the morphotropic phase boundary. The monoclinic phase is not shown.5
- Figure 1-3:** The intrinsic and extrinsic response to an applied electric field. The intrinsic response is associated with the displacement of the central cation parallel to the applied field, resulting in the distortion of the unit cell. The extrinsic response is the movement of interfaces such as 90° and 180° domain walls in a tetragonal system.6
- Figure 1-4:** Polarization vs. electric field (P-E) hysteresis loop of a polycrystalline and single crystal ferroelectric ceramic. The polycrystalline P-E loop was measured on a $\{001\}$ -textured, $1.11 \mu m$ tetragonal $Pb(Zr_{0.3}Ti_{0.7})O_3$ thin film. Schematics A-F represent different domain states during a P-E cycle for an appropriately oriented single crystal with only 180° domain walls present.7
- Figure 1-5:** A diagram of reversible motion of a domain wall within a deep potential energy well and irreversible motion of a domain wall within a shallow potential energy well within a potential energy landscape of a ferroelectric material.9
- Figure 1-6:** (a) An XRD pattern showing the change in the 002 and 200 peak position during application of an electric field for a $\{001\}$ -textured, $1.11 \mu m$ tetragonal $Pb(Zr_{0.3}Ti_{0.7})O_3$ thin film. (b) A complimentary schematic showing the change in the out-of-plane d -spacings of a and c -domains during application of electric field in the out-of-plane direction with crystallographic representations of the d -spacings with respect to the spontaneous polarization direction (c). The dashed lines in (b) correspond to the original shape. The red dashed lines in (c) correspond to the original shape. 10
- Figure 1-7:** The thickness dependence of the relative permittivity ($\epsilon_{r,33}$) and piezoelectric coefficient (d_{33}) measured at room temperature of a variety of ferroelectric materials including polycrystalline and epitaxial PZT thin films with either morphotropic or tetragonal composition, polycrystalline PLaZT of various compositions, and other PZT-based and lead-free materials for a variety of processing conditions. Figure taken from Ihlefeld *et al.*[34] 14
- Figure 1-8:** (a) A diagram of the low dielectric permittivity regions (light blue) along the film-substrate interface, film surface and grain boundaries within a thin film with columnar grains. As the film thickness or grain size is scaled down, the volume fraction of the low dielectric permittivity regions increases. (b) and (c) shows the thickness dependence of the relative permittivity (ϵ_r) as a result of the scaling of film thickness and grain size, respectively. This figure is adapted from Ihlefeld *et al.*[34] 15

- Figure 2-1:** X-ray diffraction patterns depicting the dependence of the preferred orientation of the 1% Mn-doped PZT 30/70 Mitsubishi Materials seed layer on the spin rates for chemical solution deposition.21
- Figure 2-2:** Schematic of the layer-by-layer crystallization steps used to grow PZT 30/70 thin films ranging in thickness from 0.27 μm to 1.1 μm for (a) films doped with 2% Nb and (b) films doped with 1% Mn. The cross section of the Pt/PZT/Pt/TiO₂/SiO₂/Si stack is also shown.22
- Figure 2-3:** Top-down micrographs of PZT 30/70 thin films for thickness ranging from 0.27 μm to 1.1 μm showing the distribution of grain sizes. A cross-sectional micrograph of the 0.56 μm PZT thin film on a Pt electrode illustrating columnar grain growth of the film. There is no evidence of porosity or secondary phases.....22
- Figure 2-4:** (a) A top down view of the Pt electrode for each release state: clamped or 0% released, 25% released, 50% released and 75% released. The different degrees of release were achieved by varying the density of the etch pits within one electroded region. (b) 3-D cross-sectional schematics of the release structures including the etch pits that run vertically through the Pt/PZT/Pt/TiO₂/SiO₂ stack and the 100 μm diameter etch trench that was undercut into the Si substrate below each etch pit region (not to scale). (c) An optical microscope image of the top down view of part of a released electrode and (d) a cross-sectional micrograph of the released Pt/PZT/Pt/TiO₂/SiO₂ stack suspended above the etch trench.24
- Figure 2-5:** Phase pure X-ray diffraction patterns of tetragonal {001} textured PZT 30/70 thin films doped with 2% Nb and thicknesses ranging from 0.27 μm to 1.1 μm (a, b). The peak fitting of the 002/200 peaks for the 1.1 μm film is shown (c). The normalized volume fraction of c-domains (v_{002}) is also shown as a function of film thickness (d). Note: error bars are smaller than the symbol size.....26
- Figure 2-6:** (a) Measured relative permittivity vs. a.c. field and (b) frequency dispersion of the Rayleigh parameter α_e and $\epsilon_{\text{initial}}$ for clamped the seed layer of 0.06 μm thickness and 1% Mn-doped PZT 30/70 composition. The frequency dispersion of the Rayleigh parameter α_e (c) and $\epsilon_{\text{initial}}$ (d) for clamped 0.38-0.35 μm 1% Mn-doped PZT 30/70 films grown using PSU-made sol gel compared to a clamped 0.35 μm 1% Mn-doped PZT 30/70 film grown using Mitsubishi Materials solution is also shown. The Mitsubishi Materials solution was exclusively used for growth of the 0.06 μm seed layer.....28
- Figure 2-7:** Polarization vs. electric field hysteresis loops of clamped 2% Nb-doped PZT 30/70 thin films of varying thickness ranging from 0.27 μm to 1.1 μm30
- Figure 2-8:** The change in P–E hysteresis loops of 2% Nb-doped PZT 30/70 thin films between the clamped and 75% released states for (a) 1.11 μm , (b) 0.38 μm , and (c) 0.27 μm thick films. The evolution of the P–E loop for the 0.38 μm thick film is also shown for clamped, 25%, 50% and 75% released states.31
- Figure 2-9:** Frequency dispersion of the Rayleigh parameter α_e as a function of film thickness ranging from 0.27 μm to 1.1 μm for PZT 30/70 thin films doped with 2%

Nb in the clamped state before applying the capacitor in series model (Seed + Film) (a), in the clamped state after applying the model (Film) (b) and in the 75% released state after applying the model (c).....	32
Figure 2-10: A micrograph of the torn electroded regions extending from the etch pit after global released.	34
Figure 2-11: Frequency dispersion of the Rayleigh parameter α_e as a function of release state including clamped or 0% released, 25% released, 50% released and 75% released from the substrate for 0.27 μm thick PZT 30/70 thin film doped with 2% Nb.....	35
Figure 2-12: Frequency dependence (B) of the Rayleigh parameter α_e as a function of film thickness for PZT 30/70 thin films doped with 2% Nb (a) for the clamped state before applying the capacitor in series model (Seed + Film), the clamped state after applying the model (Film), and the 75% release state after applying the model. The dashed and dotted boxes represent values of $B(\alpha_e)$ for the 0.27 and 0.56 μm films, respectively. Complementary frequency dispersion of the Rayleigh parameter α_e are also shown for thickness 0.27 μm (b) and 0.56 μm (c).	35
Figure 2-13: Frequency dispersion of the Rayleigh parameter $\varepsilon_{\text{initial}}$ as a function of film thickness ranging from 0.27 μm to 1.1 μm for PZT 30/70 thin films doped with 2% Nb in the clamped state before applying the capacitor in series model (Seed + Film) (a), in the clamped state after applying the model (Film) (b) and in the 75% released state after applying the model (c).....	37
Figure 2-14: Frequency dispersion of the Rayleigh parameter $\varepsilon_{\text{initial}}$ as a function of release state including clamped or 0% released, 25% released, 50% released and 75% released from the substrate for 0.27 μm thick PZT 30/70 thin film doped with 2% Nb.	38
Figure 2-15: Frequency dependence (B) of the Rayleigh parameter $\varepsilon_{\text{initial}}$ as a function of film thickness for PZT 30/70 thin films doped with 2% Nb for the clamped state before applying the capacitor in series model (Seed + Film), the clamped state after applying the model (Film) and the 75% release state after applying the model.	39
Figure 2-16: The change in the Rayleigh parameters α_e (a-b) and $\varepsilon_{\text{initial}}$ (c-d) as a function of film thickness for PZT 30/70 thin films doped with 2% Nb. (a, c) Represents the change after applying the capacitor in series model. (b, d) Represents the change upon release.....	41
Figure 3-1: (a) A schematic of the applied electric field cycles during the in situ XRD study, (b) 2D diffraction image of the PZT 30/70 thin film with labeled reflections, (c) an example of the changes in peak intensity during application of electric field for the 1.11 μm PZT film, and (d) Asymmetric Pearson VII fits of the 002 and 200 reflections of the 1.11 μm PZT film at 0^*E_c	50
Figure 3-2: (a) The volume fraction of <i>c</i> -domains (v_{002}) as a function of applied electric field is shown for 2% Nb-doped PZT 30/70 thin films of thicknesses 0.27 μm , 0.56	

<p>μm, and $1.11 \mu\text{m}$ in the clamped state and in the released state. The 75% released $1.11 \mu\text{m}$ thick film exceeded a threshold current of 1×10^{-4} Amps/cm² at electric fields exceeding $2 * E_c$. Therefore, the data for the released $1.11 \mu\text{m}$ film above $1.5 * E_c$ were removed. (b) The fraction of 90° domain reorientation (η_{002}) as a function of applied electric field is also shown for the clamped state and the released state.</p>	54
<p>Figure 3-3: The evolution of the normalized volume fraction of c-domains (v_{001}) during layer-by-layer crystallization for 2% Nb-doped PZT 30/70 thin films processed via chemical solution deposition for thicknesses ranging from ~ 80 nm (1 layer) to ~ 500 nm (6 layers).</p>	55
<p>Figure 3-4: The d-spacing for the 002 (a) and 200 reflections (b) (d_{002} and d_{200}, respectively) as a function of applied electric field increment for 2% Nb-doped PZT 30/70 thin films of thicknesses $0.27 \mu\text{m}$, $0.38 \mu\text{m}$, $0.56 \mu\text{m}$, and $1.11 \mu\text{m}$ in the clamped state and the 75% released state are shown.</p>	58
<p>Figure 3-5: The thickness dependence of d-spacing for the 200 reflection (d_{200}) for 2% Nb-doped PZT 30/70 thin films of thicknesses $0.27 \mu\text{m}$, $0.56 \mu\text{m}$, and $1.11 \mu\text{m}$ at room temperature (30°C) and above the tetragonal to cubic phase transition temperature (500°C).....</p>	59
<p>Figure 3-6: The d-spacing for the 002 and 200 reflections (d_{002} and d_{200}, respectively) as a function of applied electric field increment for 2% Nb-doped PZT 30/70 thin films of thicknesses (a,e) $0.27 \mu\text{m}$, (b,f) $0.38 \mu\text{m}$, (c,g) $0.56 \mu\text{m}$, and (d,h) $1.11 \mu\text{m}$ in the clamped state and the 75% released state are shown and compared to d-spacing values for their bulk counterparts.....</p>	62
<p>Figure 3-7: (a) The full width half maximum (FWHM) for the 002 and 200 reflections as a function of applied electric field is plotted for 2% Nb-doped PZT 30/70 thin films of thicknesses $1.11 \mu\text{m}$. (b) FWHM for the 200 reflection as a function of applied electric field is plotted for clamped films of thicknesses ranging from $0.27 \mu\text{m}$ to $1.11 \mu\text{m}$ (left); and FWHM for the 200 reflection as a function of applied electric field is plotted for the $0.27 \mu\text{m}$ film for all release states (right).</p>	63
<p>Figure 3-8: A model of the domain structure within one grain before (left) and after (right) poling to $3 * E_c$. In general, the volume fraction of c-domains increases, and the c-domains coarsen upon application of electric field.</p>	64
<p>Figure 3-9: The crystallite size and microstrain as a function of film thickness for 2% Nb-doped PZT 30/70 thin films in the clamped, unpoled state.</p>	65
<p>Figure 3-10: Frequency dispersion of the Rayleigh parameter α_c as a function of film thickness ranging from $0.27 \mu\text{m}$ to $1.11 \mu\text{m}$ for 2% Nb-doped PZT 30/70 thin films in the clamped state for unpoled (a) and poled (b) films, as well as in the 75% released state for unpoled (c) and poled (d) films.</p>	68
<p>Figure 3-11: Frequency dispersion of the Rayleigh parameter $\varepsilon_{\text{initial}}$ as a function of film thickness ranging from $0.27 \mu\text{m}$ to $1.11 \mu\text{m}$ for 2% Nb-doped PZT 30/70 thin films</p>	

- in the clamped state for unpoled (a) and poled (b) films, as well as in the 75% released state for unpoled (c) and poled (d) films.70
- Figure 3-12:** The intrinsic ($\epsilon_{r,intrinsic}$) and reversible, extrinsic ($\epsilon_{r,extrinsic}$) contributions to the permittivity as a function of film thickness ranging from 0.27 μm to 1.11 μm for 2% Nb-doped PZT 30/70 thin films in the clamped and 75% released state for unpoled (a), as well as in the clamped state for unpoled and poled films (b).71
- Figure 3-13:** The intrinsic ($\epsilon_{r,intrinsic}$), reversible and irreversible extrinsic ($\epsilon_{r,extrinsic}$) contributions to the permittivity as a function of film thickness ranging from 0.27 μm to 1.11 μm for 2% Nb-doped PZT 30/70 thin films in the clamped state for unpoled (a) and poled films (b), as well as in the 75% released state for unpoled (c) and poled films (d).73
- Figure 4-1:** A schematic illustrating the dimensions and film stack of the fixed-fixed beams, including a top down view of the patterned features (a) and side view of the device stack (b) with a SEM image of the device with a 2.035 μm SiO₂ elastic layer. Also shown is a schematic listing of the dimensions and film stack for cantilevers of lengths ranging from 250 μm to 50 μm , including a top down view of the patterned features (c) and side view of the device stack (d) with a SEM image of cantilevers with a 2.035 μm SiO₂ elastic layer.80
- Figure 4-2:** Vertical displacement of a cantilever across the length (x-position) of a 250 μm long beam for a device with a 2.035 μm thick SiO₂ elastic layer and a 0.76 μm thick SiO₂ elastic layer. The cantilever displacements were determined using the optical profilometry images inset in the graph for each device.85
- Figure 4-3:** A cross-sectional schematic of the thermal residual stress that develops post-processing for a multilayered device, with a 0.76 μm thick SiO₂ layer and a 2.035 μm thick SiO₂ layer, processed on a Si substrate. The z-position of the neutral axis is shown for each device.86
- Figure 4-4:** The mesh used for FEA simulations of the multilayered PiezoMEMS device.88
- Figure 4-5:** A 2-D COMSOL model of the tip deflection of a 250 μm long cantilever, and a schematic cross-section showing the residual stress in each layer after deflection for a device with a 2.035 μm thick SiO₂ elastic layer and a 0.76 μm thick SiO₂ elastic layer.89
- Figure 4-6:** (a) The linear relationship between the residual stress ratio ($\sigma_{PZT}/\sigma_{SiO_2}$) and the PZT Young's Modulus (E_{PZT}) plotted for a device with a 2.035 μm thick SiO₂ elastic layer and a 0.76 μm thick SiO₂ elastic layer. The comparison is shown for two different SiO₂ Young's Modulus (E_{SiO_2}): 60 GPa and 100 GPa. Contour plots of σ_{PZT} vs. σ_{SiO_2} for a variety of cantilever tip displacements for a device with a 2.035 μm thick SiO₂ elastic layer (b, d) and a 0.76 μm thick SiO₂ elastic layer (c, e) for σ_{SiO_2} for 900 MPa and 1100 MPa.90
- Figure 4-7:** The vertical deflection of fixed-fixed beams across the length (x-position) of a ~1,000 μm long beam for a device with a 2.035 μm thick SiO₂ elastic layer and a

0.76 μm thick SiO_2 elastic layer. The buckling and vertical deflection of the fixed-fixed beams were determined using the optical profilometry images inset in the graph for each device.	93
Figure 4-8: A cross-sectional schematic of the neutral axis and bending moment (M) is shown across the length of a fixed-fixed beam with a 0.76 μm thick SiO_2 layer and a 2.035 μm thick SiO_2 layer.	95
Figure 4-9: Optical profilometry image of a fixed-fixed beam device with a 2.035 μm SiO_2 layer that is partially and non-uniformly released after an interrupted XeF_2 etch.	95
Figure 4-10: Polarization vs. electric field (P-E) hysteresis loops of an unpoled (a) clamped PZT 30/70 thin film, (b) cantilever and (c) fixed-fixed beam for a device with a 2.035 μm thick SiO_2 elastic layer and a 0.76 μm thick SiO_2 elastic layer. P-E loops of a poled fixed-fixed beam for devices with the different SiO_2 elastic layer thicknesses are also shown (d). Complementary optical profilometry images are shown for each device.	96
Figure 4-11: Frequency dispersion of the Rayleigh parameter α_e of a (a) clamped PZT 30/70 thin film, (b) cantilever and (c) fixed-fixed beam for a device with a 2.035 μm thick SiO_2 elastic layer and a 0.76 μm thick SiO_2 elastic layer. Also included is the frequency dispersion of the Rayleigh parameter $\epsilon_{\text{initial}}$ of a (d) clamped PZT 30/70 thin film, (e) cantilever and (f) fixed-fixed beam for a device with a 2.035 μm thick SiO_2 elastic layer and a 0.76 μm thick SiO_2 elastic layer.	99
Figure 6-1: Grazing incidence XRD patterns of polycrystalline PZT 35/65 thin films. The evolution of the phase coexistence of tetragonal and rhombohedral phases as a function of incidence angle (i.e. film depth) is shown. This figure was taken from M. B. Kelman <i>et al.</i> [143].	110
Figure 6-2: Schematics comparing techniques for using nanoprobe X-ray diffraction in (a) transmission mode and (b) grazing incidence angle reflectance mode in order to achieve depth profiling of strain and domain distributions in a multilayered ferroelectric thin film.	112
Figure 6-3: A diagram of the experimental set up for multi-scale 3D imaging of strain and structure using dark-field X-ray microscopy. Figure taken from H. Simons <i>et al.</i> [157].	114

List of Tables

Table 2-1: Etch conditions for released structures	23
Table 2-2: Frequency dependence of Rayleigh parameter α_e (cm/kV)	39
Table 2-3: Frequency dependence of Rayleigh parameter $\epsilon_{\text{initial}}$	39
Table 3-1: Microstructure and Electrical Properties for Clamped PZT 30/70 Films	48
Table 4-1: Film Thickness and Material Properties of Device Layers	82

Acknowledgements

I would like to extend my most sincere gratitude to my advisor Professor Susan Trolier-McKinstry for the mentorship and guidance that she provided during my PhD studies. Throughout my time at Penn State, I've grown intellectually and in self-sufficiency as a researcher. This is due largely to the hands-on instruction and motivation that Dr. McKinstry provided, while still giving me the freedom to gain my own experiences and connections. I am very appreciative of the high expectations she holds for her students which pushed me to improve myself every day. In particular, I'm most thankful for the opportunity to learn and adopt her exemplary techniques for effective teaching, a passion that we both share. Hopefully, in the future, I will have the opportunity to implement this teaching style in my own classroom.

A special thank you to my undergraduate advisor Professor Jacob Jones who has continuously invested in my success over the last 10 years, even remotely as my collaborator at NCSU. As a freshman undergraduate student, I was eager to gain knowledge in materials science and hands-on experience working in a laboratory. Thankfully, he saw my potential, valued my assertiveness and offered me an undergraduate research position in his lab. From this time onward, my love for ceramic processing and my appreciation for the complexity of ferroelectric materials grew, ultimately fueling my desire to obtain my Ph.D. in this field.

Over the last 5 years, I have had the privilege of conducting multiple experiments at national laboratories such as Argonne National Laboratory in Chicago and the European

Synchrotron Radiation Facility in Grenoble, France. The success of these experiments would not have been possible without the beamline scientists and beamtime members. In particular, I would like to thank Yang Ren, Olaf Borkiewicz, Guy Jennings, Rick Spence, Phil Ryan, and Dmitry Chernyshov for their time during the set up and implementation of the experiments. They also provided invaluable understanding of ferroelectrics, intellectual conversation and suggestions for data interpretation. Additionally, I would like to thank the individual members of the team, which most often included Giovanni Esteves, Hanhan Zhou, and Julian Walker, among others. The long hours in the car, at the synchrotron facilities and during night shifts were made exponentially better by the light-hearted nature, great sense of humor, and unwavering commitment of these friends and colleagues.

I am very grateful for the opportunity to work with colleagues at the Army Research Laboratory, such as Ron Polcawich, Ryan Rudy, and Jeffrey Pulskamp. Additionally, I would like to thank Brian Power and Joel Martin of the Army Research Laboratory and Steven Isaacson of General Technical Services for their assistance in the nanofabrication of the PiezoMEMS devices used in Chapter 4 of this thesis. The experience that I've gained through this project have helped pave the way towards the start of my career as a research scientist in a DoD lab.

I would also like to thank past and present STM group members. I was very fortunate to have senior group members who voluntarily provided equipment training, processing advice, wisdom, scientific ideas and constructive criticism throughout my Ph.D. In particular, I would like to thank Trent Borman, Kathleen Coleman, Nicole Hall, Chris

Cheng, Tianning Liu and Dixiong Wang for their shared ideas, conference companionship and continued friendship.

The research conducted during my Ph.D. would not have been possible without the training and guidance provided by the Nanofabrication and MCL staff. I wanted to particularly thank Nichole Wonderling for the many hours she spent with me in the XRD room calibrating an instrument, analyzing data, perfecting sample alignment, and designing new and fun attachments for the XRD tools. I also want to thank Beth Jones, Mike Labella and Bill Drawl for all their help with sample fabrication, sputtering and photolithography. I have been truly blessed to work in such a friendly and family-like environment created through the kindness and generosity of the MCL and Nanofab staff.

Thank you to my thesis committee, Professor Clive Randall, Dr. Roman Engel-Herbert, Professor Michael Lanagan, and Professor Jacob Jones who have supported and challenged me throughout my Ph.D. They have had uncompromising, high expectations for the quality of my thesis, education and research, which has led to my exponential growth as a scientist. For this, I am grateful.

Although my family does not hold degrees in the STEM field and may not understand the details of my dissertation, they have whole-heartedly supported me through my graduate studies. I am so incredibly blessed to have their constant love and praise. I know that, no matter which path I take from here on, they will be nothing but proud.

Through my time at Penn State, I have made lasting friendships with so many people. I would like to thank those that ate lunch with me almost every day in the third-

floor commons of MSC. We enjoyed a great view and the ability to share our daily frustrations, joys and accomplishments. I would also like to thank the Saturday game night group for forcing me to set aside research and studying to spend time with friends and learn a new board game. Thank you for fueling my love for themed parties, wine and cheese nights, experimental baking, among other things. I also want to acknowledge a close group of friends that I call my cohortians. You have been my family away from home. Finally, I would like to thank my fiancée who I met my first year at Penn State. Since the start of our Ph.D. program, he has been by my side as a study partner, friend, and confidante. I'm so glad to have shared this experience with him and look forward to the rest of our lives together.

I gratefully acknowledge funding from the National Science Foundation (DMR-1410907, DMR-1409399, DGE-1255832) and a National Science Foundation Graduate Research Fellowship Program, the U.S. Army Research Office, U.S. Department of Energy under contract No. DE-AC02-06CH11357, the Alfred P. Sloan Foundation and the Pennsylvania State University's Institute for CyberScience Advanced CyberInfrastructure (ICS-ACI).

Chapter: 1 Introduction and Background

1.1 Piezoelectrics

Piezoelectrics are a type of electroceramic that exhibit the ability to interconvert mechanical and electrical energies. There are two types of piezoelectric effects: the direct effect and the converse effect.[1] The direct effect describes the materials ability to develop dielectric displacement (D_i) when subject to an applied mechanical stress (σ_{jk}), as shown in Equation 1-1.

$$D_i = d_{ijk}\sigma_{jk} \quad 1-1$$

In all tensor relationships mentioned, such as that in Equation 1-1, the tensor is described in an orthogonal coordinate system and utilizes summation over repeated indices.[2] The piezoelectric coefficient (d_{ijk}) can be used to describe the linear relationship between stress and polarization. In order for a material to exhibit piezoelectricity, a non-centrosymmetric crystal structure, i.e. a crystal structure that lacks a center of symmetry, is needed. Piezoelectric sensors take advantage of the direct effect, whereas the converse effect is utilized in actuator applications. The converse effect describes the material's ability to mechanically strain (x_{ij}) in response to an applied electric field (E_k), as shown in Equation 1-2.

$$x_{ij} = d_{kij}E_k \quad 1-2$$

This coupling allows for multi-functionality and enables the advancement of many modern technologies. For example, thin film piezoelectrics combined with silicon technology leads to miniaturized mechanical devices such as microelectromechanical

systems (MEMS) including sensors, actuators, switches and transducers.[3][4][5][6][7][8][9][10][11][12]

For insulating materials, a polarization is induced via application of an electric field. As a result, charge is collected on the surface of the material. The total charge density (i.e. the dielectric displacement, D_i) can be related to the induced polarization (P_i) and applied electric field using Equation 1-3.

$$D_i = \varepsilon_0 E_i + P_i \quad 1-3$$

The constant ε_0 represents the dielectric permittivity of a vacuum (8.854×10^{-12} F/m). Like the dielectric displacement, the induced polarization is also dependent on the applied electric field, as shown in Equation 1-4, where χ_{ij} is the dielectric susceptibility.

$$P_i = \varepsilon_0 \chi_{ij} E_j \quad 1-4$$

By combining Equation 1-3 and Equation 1-4, a relationship between the dielectric displacement and the applied electric field can be obtained, as shown in Equation 1-5.

$$D_i = (1 + \chi_{ij}) \varepsilon_0 E_j \quad 1-5$$

The permittivity (ε_{ij}) of the dielectric is defined in Equation 1-6. The relative permittivity is normalized relative to that of a vacuum: $\varepsilon_r = \frac{\varepsilon_{ij}}{\varepsilon_0}$.

$$\varepsilon_{ij} = (1 + \chi_{ij}) \varepsilon_0 \quad 1-6$$

1.2 Ferroelectrics

Ferroelectrics are a type of piezoelectric that exhibit a spontaneous polarization (P_s) which is reorientable with an applied electric field along crystallographically defined

directions.[13] Polarization reversal is commonly utilized in non-volatile FRAM to write memory. Ferroelectricity can only occur in materials that are non-centrosymmetric and have a unique polar axis. Axes of the orthogonal coordinate system (x , y , z) are oriented (where possible) along crystallographic axes of a material, with the z -axis typically defined along the polarization direction or normal to a thin film's surface. Atomistically, the polarization arises from a separation of the center of positive and negative charge in a unit cell. In a tetragonal perovskite crystal structure with chemical formula ABO_3 , P_s occurs along the z -axis in which the central cation (B) is displaced relative to the anion (O) octahedra. **Figure 1-1** shows an example of a perovskite crystal structure in the cubic (non-polar) paraelectric phase, in which P_s does not exist, and the tetragonal (polar) ferroelectric phase, in which P_s results from the displacement of the Ti central cation along the long axis of the unit cell.

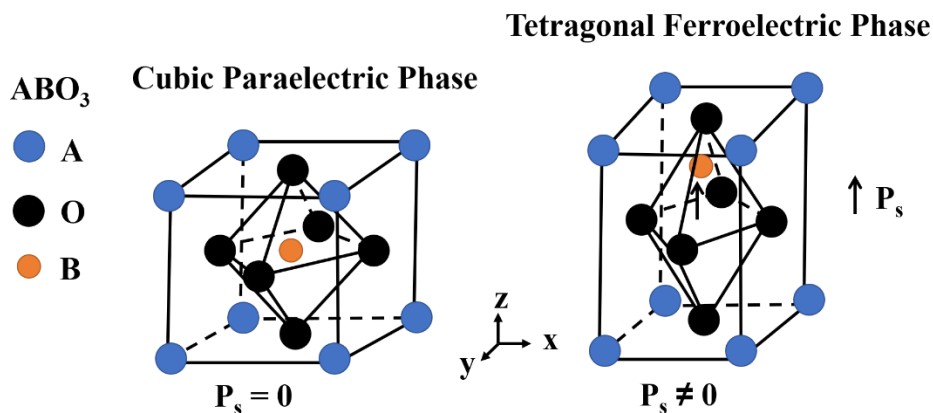


Figure 1-1: A comparison of the cubic paraelectric phase and tetragonal ferroelectric phase of the perovskite crystal structure ABO_3 . The displacement is exaggerated for clarity.

1.3 Lead Zirconate Titanate

Lead-based perovskites such as $\text{Pb}(\text{Zr}_x\text{Ti}_{1-x})\text{O}_3$ (PZT) are common ferroelectric materials used in PiezoMEMS technology for their relatively high dielectric and piezoelectric properties compared to non-ferroelectric, piezoelectric materials.[14] For these and other applications, ferroelectrics are incorporated into thin films which can be scaled by reducing film thickness to reduce operation voltage.

PZT is a solid solution of ferroelectric PbTiO_3 and antiferroelectric ZrTiO_3 . As such, the crystal structure of PZT changes with composition. A Zr:Ti ratio of less than 52:48 will result in a tetragonal crystal structure with $P4mm$ symmetry; whereas, a Zr:Ti ratio that is between 56:44 and 95:05 will result in a rhombohedral crystal structure with $R3m$ symmetry, as shown in the phase diagram of **Figure 1-2**. [15] At the morphotropic phase boundary, where the Zr:Ti ratio is ~52:48, multiple phases exist, resulting in structural instability and enhanced dielectric and piezoelectric properties, as shown for the dielectric constant (K) in **Figure 1-2**. [15][16]

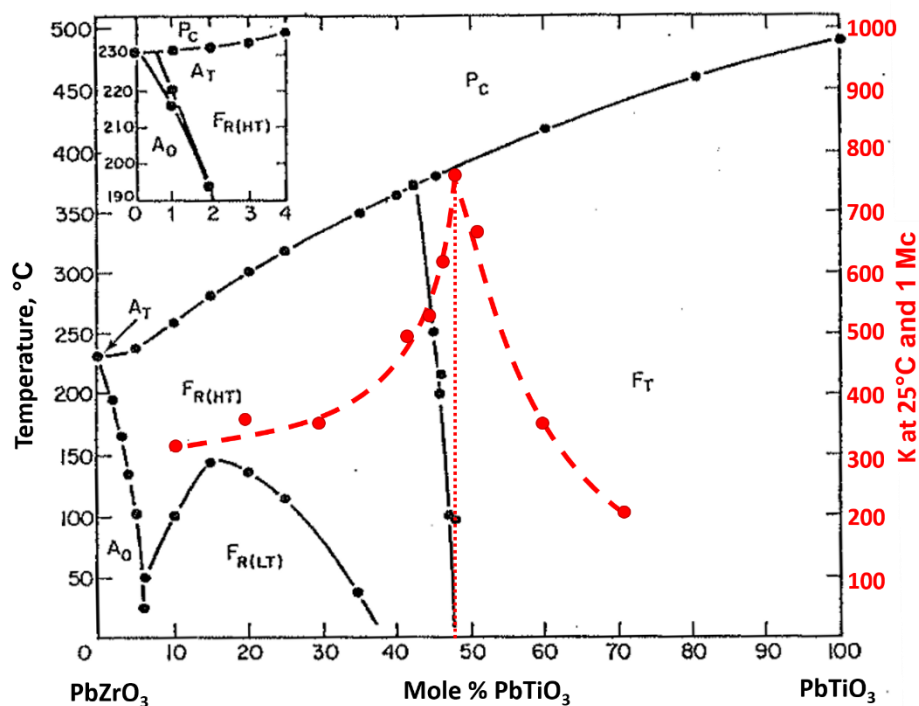


Figure 1-2: The PbTiO_3 - PbZrO_3 binary sub-solidus phase diagram with an overlay comparison of the dielectric constant (K) vs. mole % of PbTiO_3 measured at room temperature, adapted from B. Jaffe *et al.*[15] A maximum in K is observed near the morphotropic phase boundary. The monoclinic phase is not shown.

1.4 Ferroelectric Domain Structure and Formation

Although ferroelectrics have P_s defined along the unique polar axis, the orientation of P_s can vary within the material. Regions of uniform polarization within a ferroelectric are called domains and are separated by 180° or non- 180° domain walls.[17] For example, 180° domain walls separate domains with P_s that are oriented 180° from each other. In a perfect tetragonal ferroelectric, 90° domain walls are the only non- 180° domain walls that exist and separate domains with P_s that are oriented 90° from each other, as shown in **Figure 1-3**. In tetragonal ferroelectric thin films, the term c -domains is used to describe domains in which the P_s is oriented out-of-plane (normal to the film surface). In contrast, the term a -domains is used to describe domains in which the P_s is oriented in-the-plane of the film.

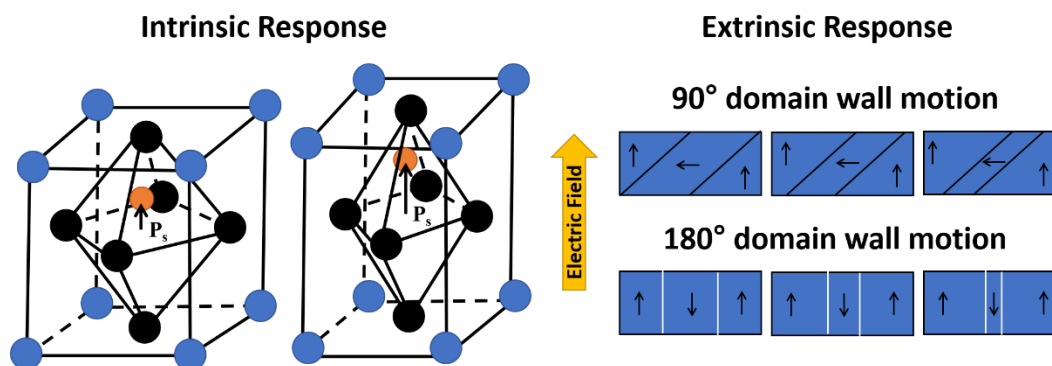


Figure 1-3: The intrinsic and extrinsic response to an applied electric field. The intrinsic response is associated with the displacement of the central cation parallel to the applied field, resulting in the distortion of the unit cell. The extrinsic response is the movement of interfaces such as 90° and 180° domain walls in a tetragonal system.

By switching the direction of the applied electric field, P_s can be switched from $-P$ to $+P$, represented by the ferroelectric polarization vs. electric field hysteresis loop (P-E loop), as shown in **Figure 1-4**. [18][19] At low applied alternating-current (ac) electric fields, there is a linear relationship between polarization and field amplitude (segment AB in the figure). This is an intrinsic response, in which the electric field further displaces the center of positive and negative charge in domains with P_s parallel to the applied electric field, resulting in a distortion of the unit cell. If a large enough field is applied, P_s oriented at an angle to the applied field direction will be reoriented parallel to the applied field direction. This is an extrinsic response, resulting in a nonlinear increase in polarization with the applied electric field (segment BC in the figure). As domains with P_s parallel to the applied field direction nucleate and grow, domain wall motion occurs. Due to its piezoelectric properties, a lattice strain can occur during non-180° domains reorientation, known as ferroelectric/ferroelastic domain reorientation, since domains switch between dissimilar unit cell dimensions. In contrast, 180° domain reorientation or ferroelectric domain orientation does not result in changes in strain of the unit cell. Finally, at high

fields, the P-E loop saturates when all domains have been reoriented to the applied electric field, resulting in a mono-domain material.

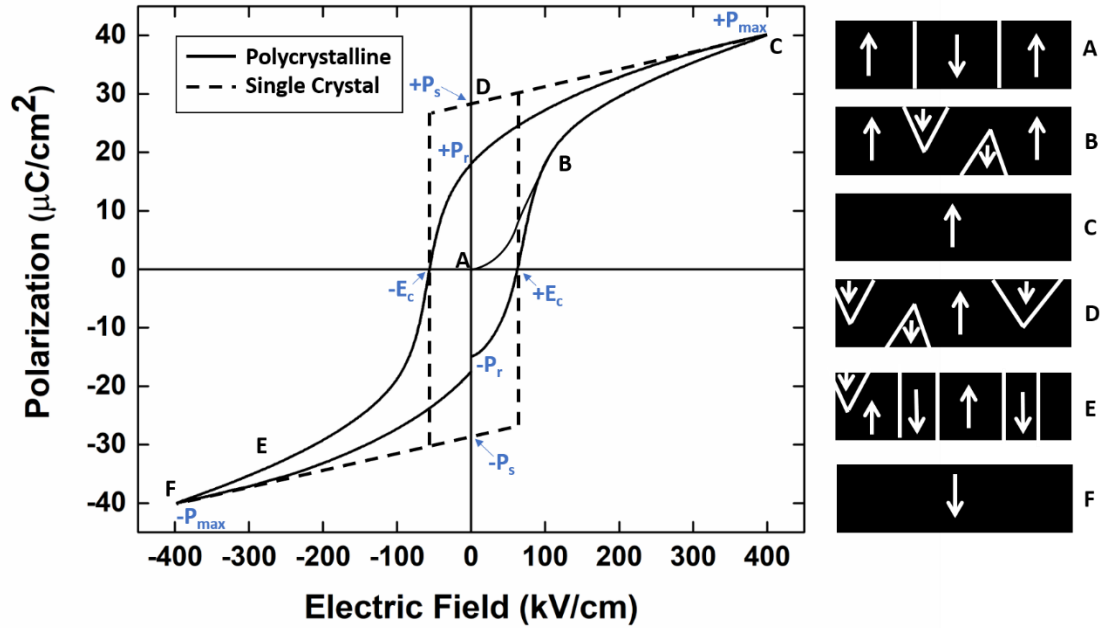


Figure 1-4: Polarization vs. electric field (P-E) hysteresis loop of a polycrystalline and single crystal ferroelectric ceramic. The polycrystalline P-E loop was measured on a {001}-textured, 1.11 μm tetragonal $\text{Pb}(\text{Zr}_{0.3}\text{Ti}_{0.7})\text{O}_3$ thin film. Schematics A-F represent different domain states during a P-E cycle for an appropriately oriented single crystal with only 180° domain walls present.

1.5 Rayleigh Analysis

The nonlinearity in the relative permittivity along with the hysteresis in the polarization can be quantified at sub-coercive, alternating current (ac) electric fields using the Rayleigh law, as shown in Equation 1-7 and 1-8.[20][21]

$$P(E) = \varepsilon_0(\varepsilon_{initial} + \alpha_\varepsilon E_0)E \pm \frac{\alpha_\varepsilon}{2} \varepsilon_0(E_0^2 - E^2) \quad 1-7$$

$$\varepsilon_r = \varepsilon_{initial} + \alpha_\varepsilon E_0 \quad 1-8$$

Equation 1-7 describes the nonlinear dependence of the polarization (P) on the driving field (E), where $E = E_0 \sin(\omega t)$, E_0 is the driving field amplitude, $\varepsilon_{initial}$ is the reversible dielectric Rayleigh coefficient and α_ε is the irreversible Rayleigh coefficient. $\varepsilon_{initial}$ arises from the reversible extrinsic contributions as well as the intrinsic contributions to the permittivity. α_ε is associated with the irreversible movement of interfaces, i.e. domain walls or phase boundaries over a potential energy barrier within a random potential energy landscape.[21] The complex potential energy landscape is dictated by local strains and internal electric fields that exist within the material as a result of defects and residual stresses, as shown in **Figure 1-5**. At low applied electric fields, domain walls oscillate reversible within a deep potential energy minima. If a large enough electric field is applied, however, the potential energy barrier for domain wall motion can be overcome, resulting in irreversible movement of domain walls from one minimum to another. To quantify the irreversible and reversible domain wall motion contributions to the relative permittivity, the potential energy landscape needs to remain constant, which is typically achieved by limiting the applied electric field amplitude to half the coercive field ($E_0 < 0.5 * E_c$). Chapter 2 uses Rayleigh analysis to describe the film thickness dependence of domain wall motion contributions in a clamped, blanket film and how the thickness dependence changes when the film is released from the substrate. Although Rayleigh analysis can be used to separate irreversible extrinsic contributions from the overall response, the technique is unable to differentiate the intrinsic response from the reversible extrinsic response, and is therefore limited.

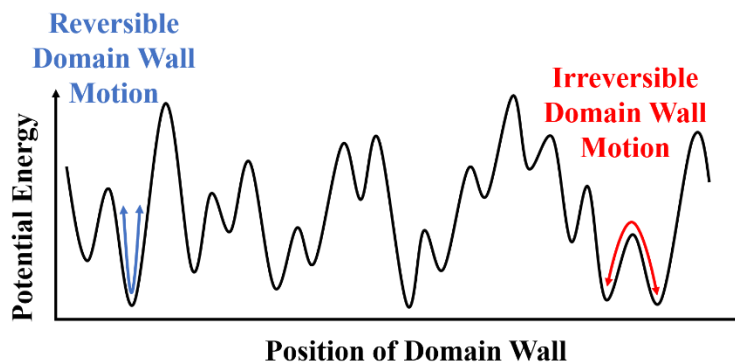


Figure 1-5: A diagram of reversible motion of a domain wall within a deep potential energy well and irreversible motion of a domain wall within a shallow potential energy well within a potential energy landscape of a ferroelectric material.

1.6 X-ray Diffraction

X-ray diffraction (XRD) is used for characterizing a variety of material properties related to crystallographic structure including phase, orientation, crystallite size, domain distributions, lattice strain and microstrain. Synchrotron sources offer high brilliance X-rays and advanced X-ray optics which are useful for irradiating a small volume of material, such as thin films, or spatially small features, such as electroded features on MEMS devices. Additionally, synchrotron facilities provide advanced detectors which enable time-resolved diffraction of crystallographic changes stimulated by external electric fields.

The application of an electric field while measuring XRD patterns *in situ* can provide additional information about the electromechanical response in ferroelectric materials including electric field induced lattice strain and ferroelectric/ferroelastic domain reorientation. An intrinsic response to an applied electric field will result in lattice strain and is indicated by the shifting of the peak positions in an XRD pattern. For example, in a $\{001\}$ textured tetragonal perovskite ferroelectrics in which only a and c -domains exist, the peak position of the $00l$ reflection will decrease to lower 2θ positions (higher d -

spacing); whereas that of the $h00$ reflection will increase to higher 2θ positions (lower d -spacing) during application of an electric field oriented normal to the film surface, as shown in **Figure 1-6**. These peak shifts correspond to the increase of the out-of-plane d -spacing of the c -domains and the decrease of the out-of-plane d -spacing of the a -domains in response to the applied electric field.

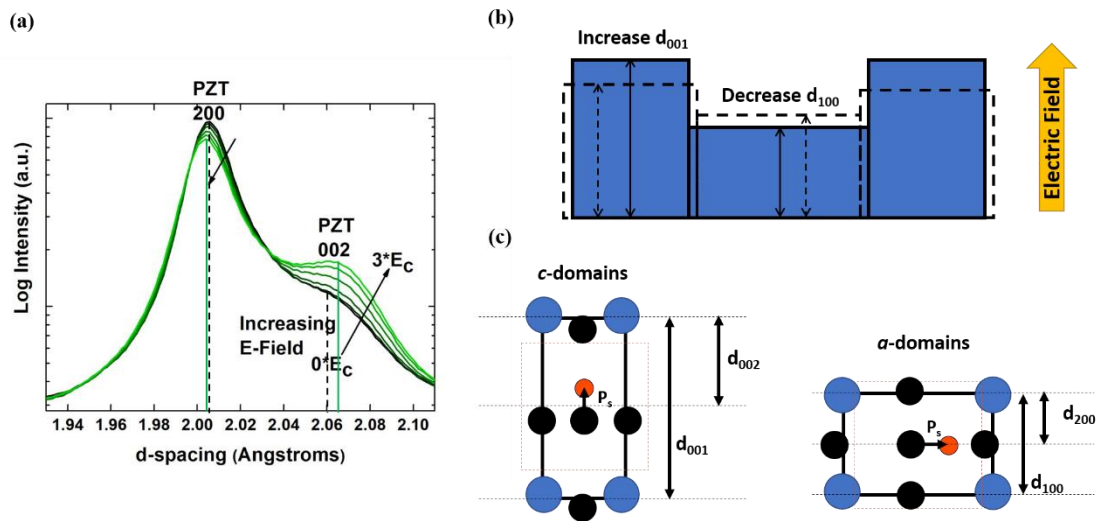


Figure 1-6: (a) An XRD pattern showing the change in the 002 and 200 peak position during application of an electric field for a $\{001\}$ -textured, $1.11 \mu\text{m}$ tetragonal $\text{Pb}(\text{Zr}_{0.3}\text{Ti}_{0.7})\text{O}_3$ thin film. (b) A complimentary schematic showing the change in the out-of-plane d -spacings of a and c -domains during application of electric field in the out-of-plane direction with crystallographic representations of the d -spacings with respect to the spontaneous polarization direction (c). The dashed lines in (b) correspond to the original shape. The red dashed lines in (c) correspond to the original shape.

An extrinsic response to an applied electric field will result in ferroelastic domain reorientation and is indicated by the change in integrated peak intensity. For a $\{001\}$ textured tetragonal perovskite ferroelectrics in which only a and c -domains exist, ferroelastic 90° domain reorientation (η_{002}) can be calculated as the electric field induced change in the volume fraction of c -domains in the direction normal to the film surface (v_{002}), as shown in Equation 1-9.

$$\eta_{002} = \nu_{002} - \nu_{002}^{0field} \quad 1-9$$

ν_{002} is determined from the integrated intensities of the 002 and 200 reflections, using Equation 1-10.[22][23]

$$\nu_{002} = \frac{\frac{I_{002}}{I'_{002}}}{\frac{I_{002}}{I'_{002}} + 2 \frac{I_{200}}{I'_{200}}} \quad 1-10$$

The term I_{hkl} represents the integrated intensity of the hkl reflection where $00l$ represents c -domain reflections and $h00$ represents a -domain reflections. I'_{hkl} represents the reference intensity from the powder diffraction file ($I'_{002}=109$ and $I'_{200}=249$ for PZT 30/70).[24]

XRD can be coupled with Rayleigh analysis to deconvolute the intrinsic contributions from the reversible, extrinsic contributions to the relative permittivity represented in the reversible Rayleigh coefficient $\varepsilon_{initial}$. Based on the volume fraction of a -domains and c -domains measured during XRD, intrinsic relative permittivity values can be calculated using Equation 1-11 which accounts for the inherent dielectric anisotropy of a tetragonal PZT film.

$$\varepsilon_{r,intrinsic} = \nu_{200} * (\chi_{11} + 1) + \nu_{002} * (\chi_{33} + 1) \quad 1-11$$

In this equation, ν_{002} is the volume fraction of c -domains determined from diffraction measurements. The free dielectric susceptibility values were taken from reference [25]. The reversible, extrinsic contributions to the relative permittivity can be determined using Equation 1-12, in which $\varepsilon_{initial}^{0Hz}$ is the extrapolated reversible Rayleigh coefficient at 0 Hz.

$$\varepsilon_{r,extrinsic} = \varepsilon_{initial}^{0 Hz} - \varepsilon_{r,intrinsic} \quad 1-12$$

The irreversible, extrinsic contributions to the relative permittivity can be determined using the irreversible Rayleigh coefficient, α_ε , as shown in Equation 1-13.

$$\varepsilon_{r,extrinsic}^{irreversible} = \alpha_\varepsilon E_0 \quad 1-13$$

Rayleigh analysis in combination with XRD can quantify the suppression of extrinsic contributions to the relative permittivity, such as the pinning of domain walls due to the presence of structural defects and residual stresses. This method is used in Chapter 3 to understand how residual stress and substrate clamping influences the film thickness dependence of reversible domain wall motions contributions and intrinsic contributions, individually.

1.7 Residual Stresses in Thin Films

Polycrystalline PZT thin films have suppressed dielectric and piezoelectric properties compared to their bulk ceramic counterparts. The suppressed properties are in part due to the residual stresses that develop within the film during processing that limit electromechanical behavior and ultimately inhibit domain wall motion. As a result, the extrinsic contributions to the relative permittivity is reduced. The total residual stress (σ_{tot}) in a film is comprised of both thermal (σ_{th}) and intrinsic (σ_i) stresses, as shown in Equation 1-14.[26]

$$\sigma_{tot} = \sigma_{th} + \sigma_i \quad 1-14$$

The thermal stress develops upon cooling below the transition temperature from the paraelectric cubic phase to the room temperature ferroelectric tetragonal phase. σ_{th} is

related to the thermal expansion coefficient mismatch between the film (α_f) and the substrate (α_s), as shown in Equation 1-15.

$$\sigma_{th} = \frac{E_f}{(1 - \nu_f)} (\alpha_f - \alpha_s) \Delta T \quad 1-15$$

E_f and ν_f are the Young's modulus and Poisson's ratio of the film, and ΔT is the temperature processing window used during film synthesis. In contrast, intrinsic stresses are related to microstructural and/or crystallographic flaws such as line defects or non-stoichiometric defects that form during film deposition and crystallization. In a PiezoMEMS device such as a cantilever or fixed-fixed beam geometry, residual stress and thickness of each layer in a multilayered device can have a major impact on the mechanical and ferroelastic properties of the device, discussed in Chapter 4.

1.8 Scaling Effects

In addition to residual stresses, other factors can contribute to the suppression of the dielectric and piezoelectric properties in PZT thin films and are exacerbated as film thickness decreases. The thickness dependent degradation of the piezoelectric and dielectric properties at small length scales (typically between 10 nm and 1 μ m) is known as scaling effects, as shown in **Figure 1-7**. Scaling effects can be caused by thickness-dependent variations in residual stresses, grain size, interfacial passive layers, substrate clamping, electrode screening, depolarization fields, non-stoichiometric defect concentrations, domain distributions and domain wall mobility. [27][28][29][30][31][32][33]

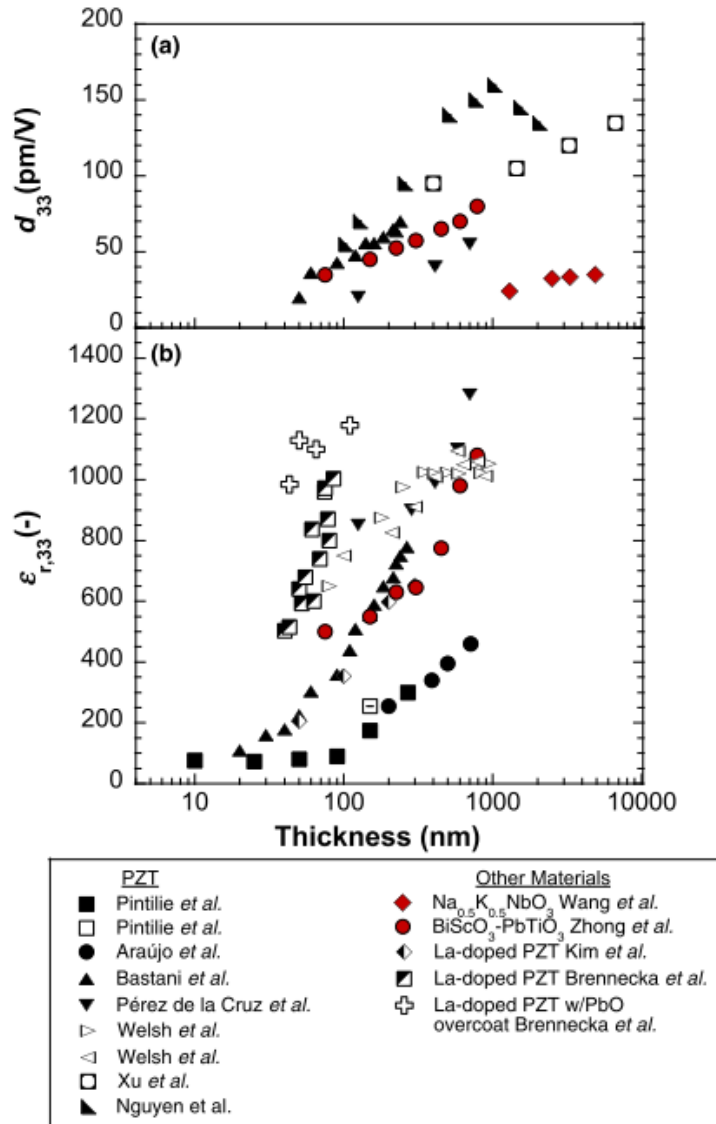


Figure 1-7: The thickness dependence of the relative permittivity ($\epsilon_{r,33}$) and piezoelectric coefficient (d_{33}) measured at room temperature of a variety of ferroelectric materials including polycrystalline and epitaxial PZT thin films with either morphotropic or tetragonal composition, polycrystalline PLaZT of various compositions, and other PZT-based and lead-free materials for a variety of processing conditions. Figure taken from Ihlefeld *et al.*[34]

Typically, in PZT thin films, a low dielectric permittivity interfacial layer exists at the film-substrate interface and/or film surface due to lead loss to the substrate and ambient, respectively, during crystallization. In a thick film, the interfacial layers make up a small volume fraction of the overall film and have little consequence on the film properties.

However, as film thickness decreases, the volume fraction of the thin film that is made of the low permittivity interfacial layers increases. Since the layers act as capacitors in series, scaling down the film thickness ultimately degrades the dielectric constant. Grain boundaries also act as low dielectric regions due to their high concentration of defects and structural flaws. As film thickness decreases, studies have shown that grain size also decreases. As a result, the volume fraction of grain boundaries within a thin film increases, lowering the dielectric constant. Therefore, grain size effects can also exacerbate the degradation of the dielectric and piezoelectric properties as film thickness decreases. A comparison of scaling effects associated with grain size vs. interfacial passive layers is shown in **Figure 1-8**.

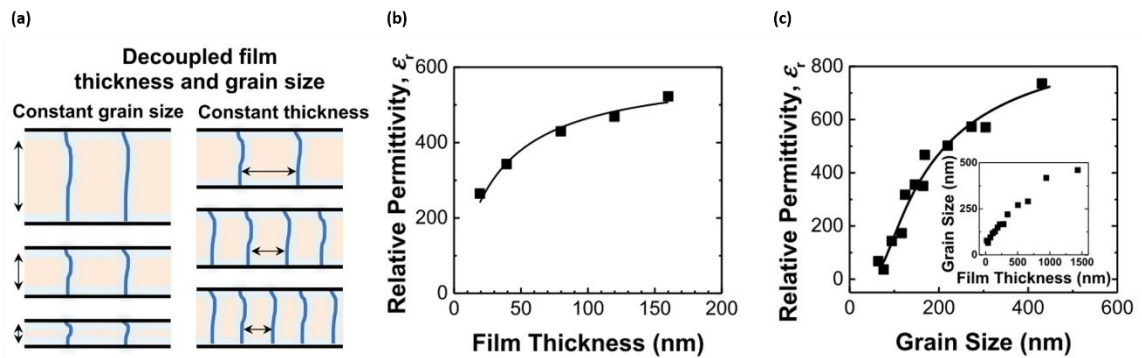


Figure 1-8: (a) A diagram of the low dielectric permittivity regions (light blue) along the film-substrate interface, film surface and grain boundaries within a thin film with columnar grains. As the film thickness or grain size is scaled down, the volume fraction of the low dielectric permittivity regions increases. (b) and (c) shows the thickness dependence of the relative permittivity (ϵ_r) as a result of the scaling of film thickness and grain size, respectively. This figure is adapted from Ihlefeld *et al.*[34]

Due to the electromechanical nature of ferroelectrics, the factors that contribute to scaling effects are often interconnected. For example, variations in residual stresses can result in variations in domain distributions. PZT thin films processed on Si substrate are under tensile residual stresses due to the thermal expansion coefficient mismatch between the film and the substrate. The tensile residual stress forms upon cooling below the

transition temperature of PZT. Therefore, the residual stress dictates the domain distribution that forms, favoring higher volume fractions of a -domains with the long axis of the unit cell in the plane of the film to better accommodate the in-plane tensile stress. Both the in-plane tensile stress and the predominantly a -domain state will suppress the dielectric and piezoelectric properties of PZT thin films. Residual stresses can mechanically suppress domain wall motion or domain wall mobility. Additionally, reduced domain wall densities, due to a predominantly a -domain state, can limit the extrinsic contributions to the relative permittivity. To minimize or prevent the property degradation in thin films at small length scales, it is necessary to investigate how these factors influence each other in order to determine the underlying mechanisms behind scaling effects.

Chapter: 2 Thickness Dependent Response of Domain Wall Motion in Declamped {001} $\text{Pb}(\text{Zr}_{0.3}\text{Ti}_{0.7})\text{O}_3$ Thin Films

Portions of this chapter are reproduced from: L. M. Denis, G. Esteves, J. Walker, J. L. Jones, and S. Trolier-McKinstry, "Thickness dependent response of domain wall motion in declamped {001} $\text{Pb}(\text{Zr}_{0.3}\text{Ti}_{0.7})\text{O}_3$ thin films," *Acta Mater.*, **151**, 243-252, (2018).

2.1 Introduction

Ferroelectric thin films such as $\text{Pb}(\text{Zr}_x\text{Ti}_{1-x})\text{O}_3$ (PZT) have high dielectric and piezoelectric properties which can be utilized in actuators, sensors, transducers, and energy harvesters in microelectromechanical systems (MEMS).[4][8] A small film thickness is necessary when high capacitance density (including thin film multilayer ceramic capacitors) or low voltage operation is required.[35][36][37] However, thickness-dependent property degradation limits the extent that the film thickness can be reduced while maintaining the performance of such devices.[34][38]

Scaling effects are the size-induced degradation of piezoelectric, ferroelectric and dielectric properties at length scales (typically between 10 nm and 1 μm) exceeding those associated with the thermodynamic stability limits for a ferroelectric phase (~ 1 nm).[34][39] Scaling effects in ferroelectric films are caused by: substrate clamping, residual stresses, dislocations, interfacial passive layers, electrode screening, depolarization fields, changes in grain size, a higher concentration of defects at the film-substrate interface, or thickness-dependent changes in the domain wall population and/or changes in the domain wall mobility.[27][28][29][30][31][32][33] Additionally, scaling effects can be exacerbated by processing. Conversely, size effects are caused by the

suppression of the intrinsic contribution to the material response as length scales approach the limits of thermodynamic stability for a ferroelectric phase (~ 1 nm). Examples of suppressed intrinsic contribution include the reduction of ferroelectric distortions, polarization, piezoelectric coefficients, and permittivity.

Scaling effects are manifested in the degradation of the longitudinal piezoelectric coefficient and relative permittivity as a function of film thickness. This phenomenon is evident for both epitaxial and polycrystalline ferroelectric films of various compositions.[34] In most Pb-based perovskites, the relative permittivity ($\epsilon_{r,33}$) starts to decay significantly below a film thickness of ~ 100 nm; however, in some cases, gradual decreases in the permittivity start in films as thick as ~ 1 μm .[40] Since the degradation of $\epsilon_{r,33}$ occurs at film thicknesses much greater than the ferroelectric stability limit, the property degradation at these lengths scales is attributed to extrinsic scaling effects.[41][42] In particular, it is observed that ferroelastic non- 180° domain wall motion is suppressed as thickness decreases.

The nonlinearity in the relative permittivity along with the hysteresis in the polarization can be quantified at sub-coercive, ac electric fields using the Rayleigh law, defined in Equation 1-7 and 1-8 of Chapter 1 in this thesis.[20][21] In short, $\epsilon_{initial}$ is the reversible dielectric Rayleigh coefficient and arises from the reversible extrinsic contributions as well as the intrinsic contributions to the permittivity. α_ϵ is the irreversible Rayleigh coefficient and is associated with the irreversible movement of interfaces, i.e. domain walls or phase boundaries, over a potential energy barrier within a random potential energy landscape.[21]

Numerous reports on PZT 52/48 [43][44][45][46][47][48] and PZT 30/70 [49] demonstrate that the α_ε decreases in films of thicknesses below $\sim 1 \mu\text{m}$, indicating that the irreversible domain wall motion contribution to the permittivity is suppressed. These prior results were obtained for continuous films on rigid substrates. However, in many MEMS devices, the film is at least partially released. The release state may change the thickness dependence of α_ε and associated scaling effects, since substrate clamping is known to suppress the extent of non-180° domain wall motion in ferroelectric thin films.[50][51] Therefore, there is a need to investigate the influence of substrate clamping on the thickness-dependent extrinsic contribution to the relative permittivity.

For a fixed film thickness, the clamping of the film can be alleviated in several ways. First, island structures with high aspect ratios allow the structures to be partially declamped, thus, increasing 90° domain wall mobility and doubling the remanent polarization of PZT at high applied electric fields.[50][52] Additionally, piezoelectrically-active, ferroelectric nanotubes with high aspect ratios have been created via vacuum infiltration of macroporous Si templates (aspect ratio of $>10:1$)[10] or a bottom-up nanomanufacturing method (aspect ratio of $5:1$)[53]. The high aspect ratios in these studies were chosen such that substrate clamping effects could be minimized. Declamping can also be achieved by releasing diaphragm structures from the underlying substrate.[54][55] The resulting increase in dielectric properties were attributed to lower potential energy barriers which allowed enhanced irreversible domain wall motion and an increase in α_ε for the released film. Synchrotron diffraction of films $> 1 \mu\text{m}$ in thickness demonstrate that released films show higher levels of non-180° domain reorientation under field.[51] However, released cantilevers still demonstrate thickness dependent remanent polarization

and piezoelectric properties attributed to residual stresses. These residual stresses are commonly associated with the thermal expansion coefficient mismatch between the film and the substrate and/or the presence of a thin layer at the film-substrate interface with a low dielectric constant.[56] In this work, scaling effects have been investigated in PZT films $< 1 \mu\text{m}$ thick in both clamped and partially released states relevant to MEMS devices.

2.2 Experimental Procedure

2.2.1 Film Synthesis and Nanofabrication

Tetragonal, {001} textured polycrystalline $\text{Pb}(\text{Zr}_{0.3}\text{Ti}_{0.7})\text{O}_3$ (PZT 30/70) thin films doped with 2% Nb were fabricated via chemical solution deposition (CSD) as described elsewhere.[57][58] The solution was deposited onto a Pt/TiO₂/SiO₂/Si stack to produce films with thickness ranging from 0.27 to 1.11 μm . Prior to the deposition of the film, a 0.08 M PbO layer was spin coated onto the Pt then dried (1 min. at 150°C and 2 min. at 250°C) and pyrolyzed (10 min. at 400°C). This PbO layer was not crystallized. The underlying layer of PbO provided excess lead at the film-substrate interface which minimized lead loss to the substrate during crystallization. A commercial PZT-E1 sol-gel solution (Mitsubishi Materials Corporation, Tokyo, Japan) of composition $\text{Pb}(\text{Zr}_{0.3}\text{Ti}_{0.7})\text{O}_3$ with 10 mol% lead excess, doped with 1 mol% Mn and a concentration of 10 wt% PZT was used to promote {001} texturing. This solution was deposited onto the PbO layer at 2000 rpm, dried (2 min. at 150°C), pyrolyzed (5 min. at 300°C), and crystallized in a rapid thermal annealer (RTA) (1 min. at 700°C in flowing O₂ gas at 2 SLPM and a ramp rate of 10°C/s). As shown in **Figure 2-1**, a spin speed of 2000 rpm produced the best {001} texturing of the seed layer; this corresponds to a seed layer thickness of ~60 nm. Above

this critical thickness, {111} texture developed; below this critical thickness, {110} texture was observed. Similar results have been obtained for seeding of undoped PZT 52/48 films from Mitsubishi Materials solutions.[59][60]

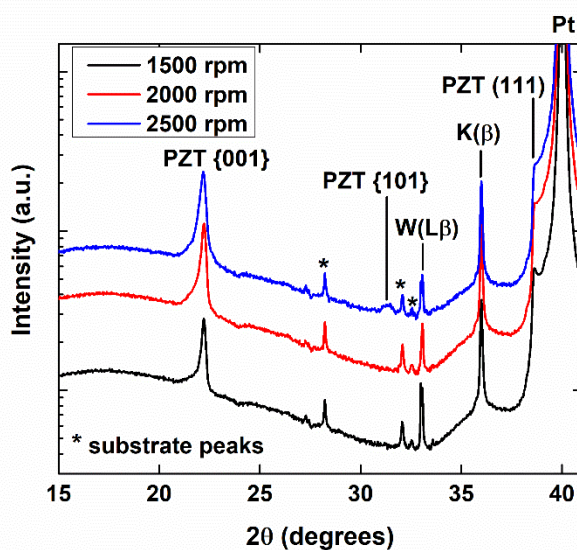


Figure 2-1: X-ray diffraction patterns depicting the dependence of the preferred orientation of the 1% Mn-doped PZT 30/70 Mitsubishi Materials seed layer on the spin rates for chemical solution deposition.

After crystallization of the seed layer, 0.4M PZT 30/70 sol-gel with 12 mol% lead excess and doped with 2 mol% Nb was spin coated at either 3000 rpm or 1500 rpm, dried (2 min. at 250°C), pyrolyzed (5 min. at 400°C), crystallized in the RTA (1 min. at 700°C in flowing O₂ gas at 2 SLPM and a ramp rate of 10°C/s) and repeated until the desired overall film thickness was obtained. To obtain high quality films with similar grain size distributions, the processing conditions were optimized for the desired film thickness as needed. As the overall film thickness decreases, the number of deposited layers must be decreased to keep the spin speed and layer thickness constant. However, as the number of deposited layers decreases, there is an increased probability of forming a pin hole in the film which will result in a decreased electrode yield. To combat this, the number of

deposited layers was increased in thinner films ($< 0.56 \mu\text{m}$ thick). Increasing the spin speed from 1500 rpm to 3000 rpm decreased the thickness of each layer and allowed more layers to be deposited for a given film thickness. This method was also employed by Bastani *et al.* to obtain thin insulating PZT films.[29] **Figure 2-2** shows a schematic of the thickness series. The long pyrolysis step enabled the growth of high-density films with lateral grain sizes of 50-150 nm, as shown in the field emission scanning electron microscopy (FESEM) images in **Figure 2-3**.

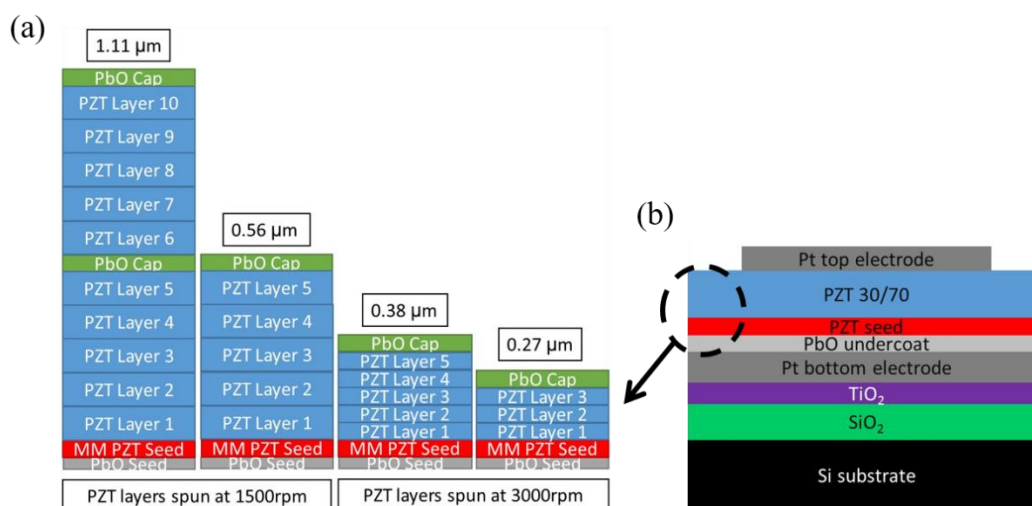


Figure 2-2: Schematic of the layer-by-layer crystallization steps used to grow PZT 30/70 thin films ranging in thickness from 0.27 μm to 1.1 μm for (a) films doped with 2% Nb and (b) films doped with 1% Mn. The cross section of the Pt/PZT/Pt/TiO₂/SiO₂/Si stack is also shown.

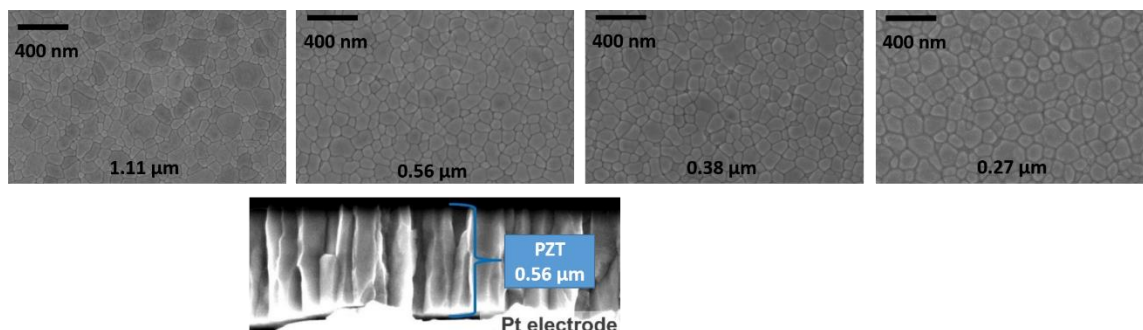


Figure 2-3: Top-down micrographs of PZT 30/70 thin films for thickness ranging from 0.27 μm to 1.1 μm showing the distribution of grain sizes. A cross-sectional micrograph of the 0.56 μm PZT thin film on a Pt electrode illustrating columnar grain growth of the film. There is no evidence of porosity or secondary phases.

To provide excess lead to the surface of the film, after every 5 crystallized layers of PZT 30/70, a 0.08M PbO layer was spin coated at 6000rpm, dried (1 min. at 150°C and 2 min. at 250°C) and crystallized in the RTA (1 min. at 700°C in 2 SLPM O₂ gas at a ramp rate of 10°C/s). The PbO crystallization steps are also shown in **Figure 2-2**, labeled as ‘PbO cap’. This converted lead-deficient surface pyrochlore (or fluorite) phases to the desired perovskite phase[61], and improved {001} texturing for both series of samples.

Large area platinum top electrodes (3.5 mm x 0.7 mm) were defined photolithographically and sputtered onto the PZT using RF magnetron sputtering. Part of the electroded area of the films was released from the substrate by dry etching 600 μm x 146 μm pits through the Pt/PZT/Pt/TiO₂/SiO₂ stack using an Ulvac NE-550 inductively coupled high-density plasma etch tool. The exposed Si substrate was then etched via an isotropic Xactic XeF₂ e1 vapor etch tool until a 100 μm diameter trench was formed, as discussed elsewhere.[51][54] The conditions of the etch recipes for these two steps are listed in **Table 2-1**. The sample was annealed at 400°C for 30 minutes before and after the XeF₂ etch step to remove residual moisture and reduce etch damage. The density of the etch pits within one electroded area dictated the percent of electroded area that was released from the substrate (fully clamped or 0% released, 25% released, 50% released and 75% released), as illustrated in **Figure 2-4** (a). The suspended electroded area above the trench represents a declamped region of the film, as shown in **Figure 2-4** (b). An optical microscope image of the top down view of a released electrode and a cross-sectional FESEM micrograph of the released Pt/PZT/Pt/TiO₂/SiO₂ stack suspended above the etch trench are shown in **Figure 2-4** (c) and (d), respectively.

Table 2-1: Etch conditions for released structures

Material	Chamber Pressure	Gas Chemistry	Forward Power	Etch Rate
Pt/PZT/Pt/TiO ₂	5 mTorr	30 sccm Cl ₂ 40 sccm Ar	300 W at MHz 0 W at MHz	Pt: 1,500 sec/ μ m PZT: 300 sec/ μ m
SiO ₂	5 mTorr	50 sccm CF ₄	300 W at MHz	240 sec/ μ m
Si	2 mTorr	XeF ₂	-	6 sec/ μ m

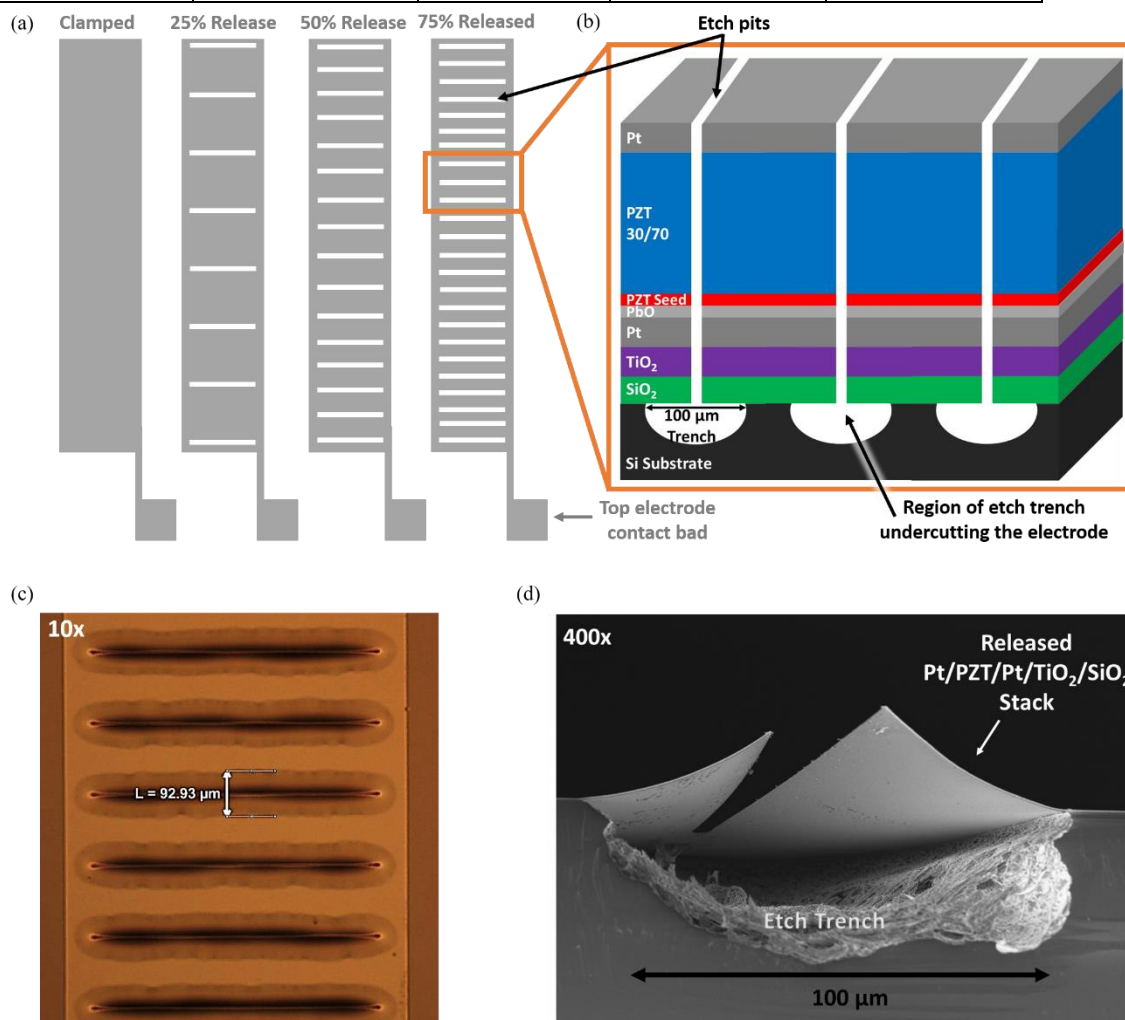


Figure 2-4: (a) A top down view of the Pt electrode for each release state: clamped or 0% released, 25% released, 50% released and 75% released. The different degrees of release were achieved by varying the density of the etch pits within one electroded region. (b) 3-D cross-sectional schematics of the release structures including the etch pits that run vertically through the Pt/PZT/Pt/TiO₂/SiO₂ stack and the 100 μ m diameter etch trench that was undercut into the Si substrate below each etch pit region (not to scale). (c) An optical microscope image of the top down view of part of a released electrode and (d) a cross-sectional micrograph of the released Pt/PZT/Pt/TiO₂/SiO₂ stack suspended above the etch trench.

2.2.2 Characterization

The orientation and phase of the film was determined from X-ray diffraction (XRD) patterns taken using a lab source diffractometer (*PANalytical Empyrean*), as shown in **Figure 2-5** (a, b). Lotgering factors ranged from 90% to 100% depending on the film thickness, with Lotgering factors closer to 100% for films below $\sim 0.5 \mu\text{m}$. The volume fraction of *c*-domains (v_{002}) of a sample in the as-processed state was calculated from the integrated intensities of the 002 and 200 XRD peaks using LIPRAS (*Line-Profile Analysis Software*).[62] An example of the peak fitting for the $1.1 \mu\text{m}$ film is shown in **Figure 2-5** (c) and the corresponding normalized v_{002} values are shown in **Figure 2-5** (d). The peaks were fit using an asymmetric Pearson VII function which takes into account the peak asymmetry and approximates the diffuse scattering.[63]

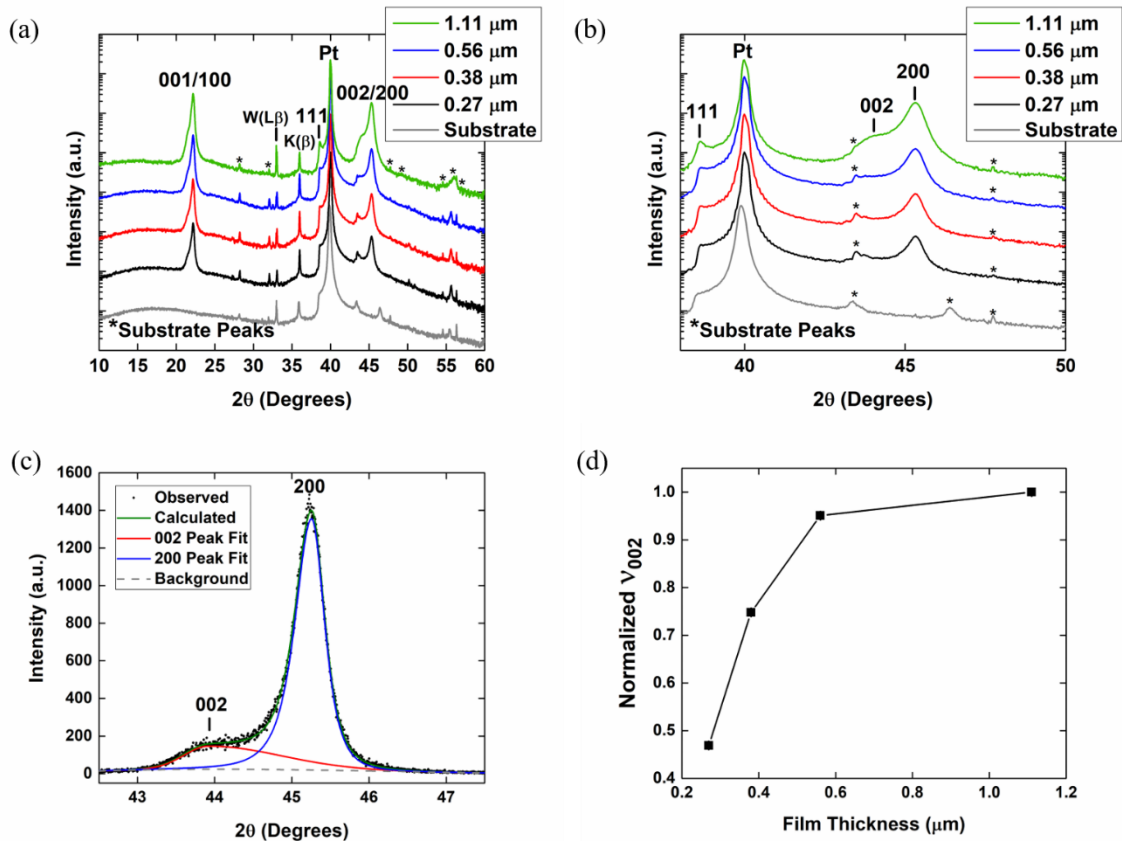


Figure 2-5: Phase pure X-ray diffraction patterns of tetragonal {001} textured PZT 30/70 thin films doped with 2% Nb and thicknesses ranging from 0.27 μm to 1.1 μm (a, b). The peak fitting of the 002/200 peaks for the 1.1 μm film is shown (c). The normalized volume fraction of c-domains (v_{002}) is also shown as a function of film thickness (d). Note: error bars are smaller than the symbol size.

v_{002} was calculated using Equation 1-10, as described in Chapter 1 of this thesis.[22][23] By using the ratio of integrated intensities over a reference intensity, the structure factors for the 002 and 200 reflections in a tetragonal system are accounted for. Error of v_{002} was calculated using an error propagation method that accounts for the integrated intensity error generated from peak fitting using LIPRAS.

Polarization vs. electric field (P–E) hysteresis loops were measured at a frequency of 10 Hz using a *Radiant Precision Ferroelectric Tester* for both clamped films and 75% released films. Further electrical characterization in the form of Rayleigh analysis was

conducted on both clamped and released films at frequencies ranging from 50 Hz to 4 kHz with applied AC electric fields up to $0.5 \cdot E_c$ (where E_c is the coercive field). These measurements were taken using a *Hewlett Packard 4284A LCR meter*. The samples were subject to an anneal at 400°C for 30 min. and an aging time of 24 hours prior to the Rayleigh measurements. The aging process was consistent across all samples prior to Rayleigh analysis. Error was calculated using an error propagation method that accounts for the error associated with a 95% confidence interval of the linear fit of the Rayleigh parameter as a function of applied AC electric field.

2.2.3 Capacitor in Series Model

To minimize the influence that the seed layer has on the Rayleigh analysis, a capacitor in series model was applied to the permittivity data, as shown in Equation 2-1 in terms of capacitance (C) and Equation 2-2 in terms of the dielectric constant (k).

$$\frac{1}{C} = \frac{1}{C_f} + \frac{1}{C_s} \quad 2-1$$

$$\frac{k}{t} = \frac{k_f}{t_f} + \frac{k_s}{t_s} \quad 2-2$$

where C represents the measured capacitance, C_s is the measured capacitance of the seed layer, C_f is the capacitance of the balance of the ferroelectric film and t is the total thickness.[29][64][65][66][67] C_s was not extracted from a linear relationship between C^{-1} vs. film thickness at zero thickness. Since the volume fraction of *c*-domains is not constant as a function of film thickness, the standard extrapolation will not accurately predict the interface capacitance, since it does not account for the thickness-dependent change of domain state. Rather, C_s is the capacitance

of the seed layer, measured as a function of ac electric field for frequencies ranging from 50 to 4,000 Hz, as shown in **Figure 2-6** (a). Dispersion curves of the Rayleigh parameters for the seed layer are also reported in **Figure 2-6** (b-c). The seed layer has a dielectric constant of 510 (measured at 1 kHz and 30 mV), which is $\sim 25\%$ less than that of the $0.35\ \mu\text{m}$ PZT film of the same composition and measurement conditions. To check the quality of the Mitsubishi Materials solution used for the seed layer, a $0.38\ \mu\text{m}$ thick film was grown using this solution. The measured Rayleigh parameters of the Mitsubishi Materials $0.38\ \mu\text{m}$ film were comparable to that of a 2-MOE-based sol gel film of $0.38\ \mu\text{m}$ thickness, as shown in **Figure 2-6**, for the same composition and a common seed layer. This comparison indicates that the suppressed properties of the $0.06\ \mu\text{m}$ seed layer, shown in **Figure 2-6** (b-c), are due to scaling effects.

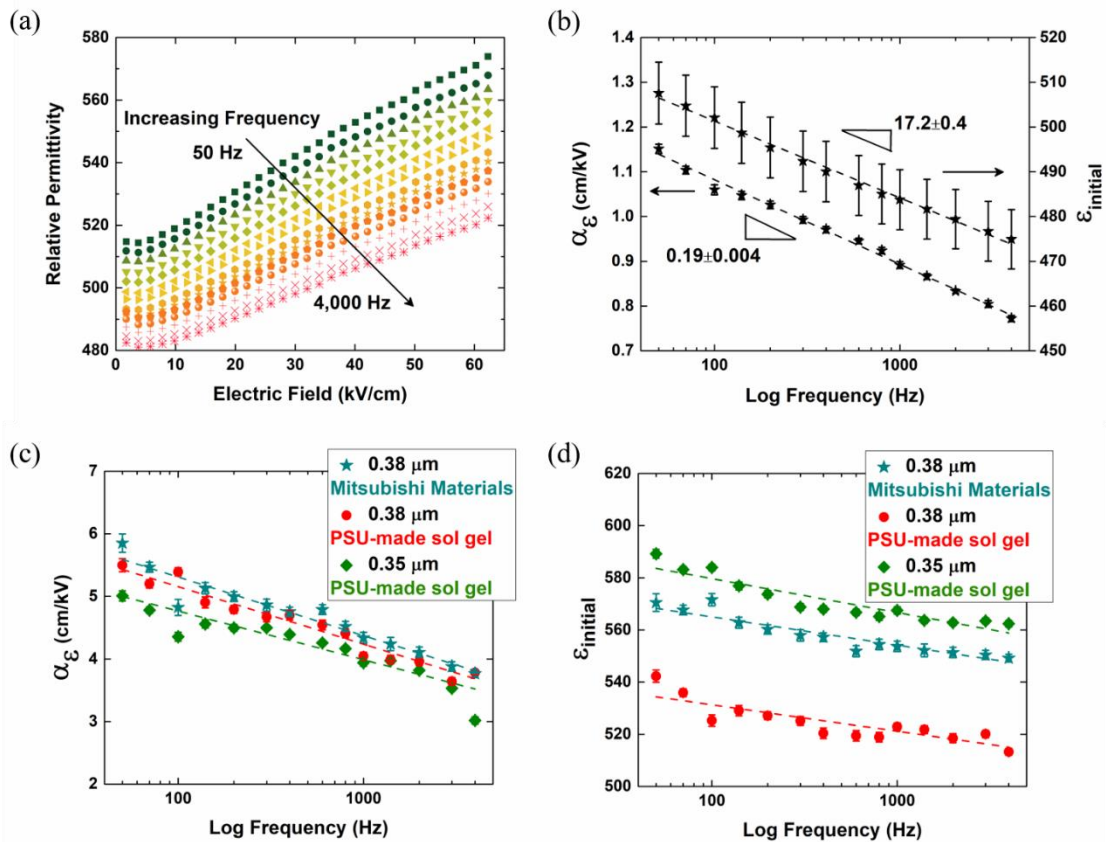


Figure 2-6: (a) Measured relative permittivity vs. a.c. field and (b) frequency dispersion of the Rayleigh parameter α_ϵ and $\epsilon_{\text{initial}}$ for clamped the seed layer of $0.06\ \mu\text{m}$ thickness and 1% Mn-doped PZT 30/70 composition. The frequency dispersion of the Rayleigh parameter α_ϵ (c) and $\epsilon_{\text{initial}}$ (d) for clamped $0.38\text{-}0.35$

μm 1% Mn-doped PZT 30/70 films grown using PSU-made sol gel compared to a clamped $0.35 \mu\text{m}$ 1% Mn-doped PZT 30/70 film grown using Mitsubishi Materials solution is also shown. The Mitsubishi Materials solution was exclusively used for growth of the $0.06 \mu\text{m}$ seed layer.

2.3 Results

2.3.1 Thickness Dependence of Polarization Hysteresis in Declamped Films

Figure 2-7 shows the P-E loops for the 2% Nb-doped PZT 30/70 thickness series. The coercive field (E_c) ranges from 54 to 63 kV/cm. The films exhibited remanent polarization (P_r) values ranging from 11 to $18 \mu\text{C}/\text{cm}^2$. P_r is defined here to be the polarization remaining in the material when the electric field is reduced to zero after applying a maximum electric field of 400 kV/cm in the positive electric field direction. The relatively small polarizations are a result, in part, of the largely a -domain state of the films resulting from the thermally induced tensile stress state of the PZT film grown on a Si substrate.[68] In general, as film thickness increases, the maximum polarization (P_{max}) and P_r increase, characteristic of the scaling effect. Upon release, P_r and P_{max} both increase for a given thicknesses, as shown in **Figure 2-8** for (a) 1.11, (b) 0.38 and (c) $0.27 \mu\text{m}$ 2% Nb-doped films. This is most clearly seen in **Figure 2-8** (b), which shows the changes in the P–E loop of $0.38 \mu\text{m}$ film for each release state (0%, 25%, 50% and 75%). Interestingly, the thinnest film ($0.27 \mu\text{m}$) shows the smallest increase in P_r after being 75% released from the substrate. This suggests that other mechanisms are involved in pinning domains in the film (e.g., potentially higher defect concentrations, higher grain boundary concentrations, or higher residual stresses in the film that are not relieved upon release).

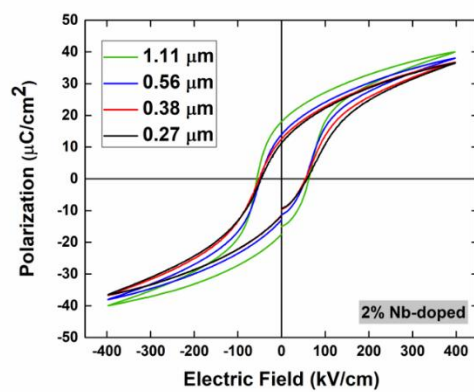


Figure 2-7: Polarization vs. electric field hysteresis loops of clamped 2% Nb-doped PZT 30/70 thin films of varying thickness ranging from 0.27 μm to 1.1 μm .

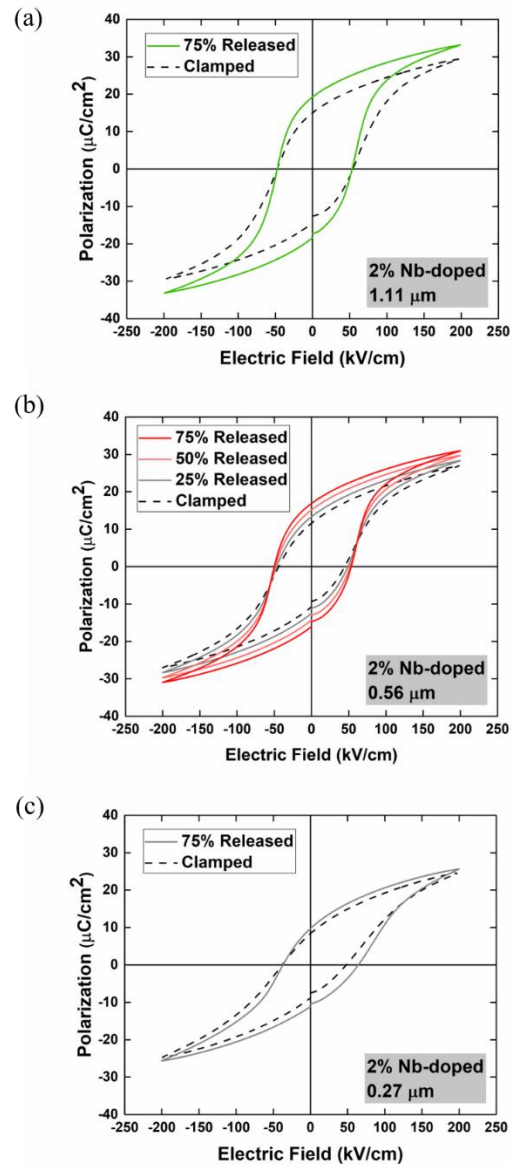


Figure 2-8: The change in P–E hysteresis loops of 2% Nb-doped PZT 30/70 thin films between the clamped and 75% released states for (a) 1.11 μm , (b) 0.38 μm , and (c) 0.27 μm thick films. The evolution of the P–E loop for the 0.38 μm thick film is also shown for clamped, 25%, 50% and 75% released states.

2.3.2 Irreversible Contributions to Permittivity

2.3.2.1 Thickness Dependence in Clamped Films

Rayleigh analysis was used to characterize extrinsic contributions to the relative permittivity in the form of irreversible domain wall motion. For clamped Nb-doped films,

the irreversible contribution to the permittivity, α_ε , decreases as film thickness decreases with thickness ranging from 1.11 μm to 0.27 μm . This thickness dependence of α_ε is shown in **Figure 2-9** (a).

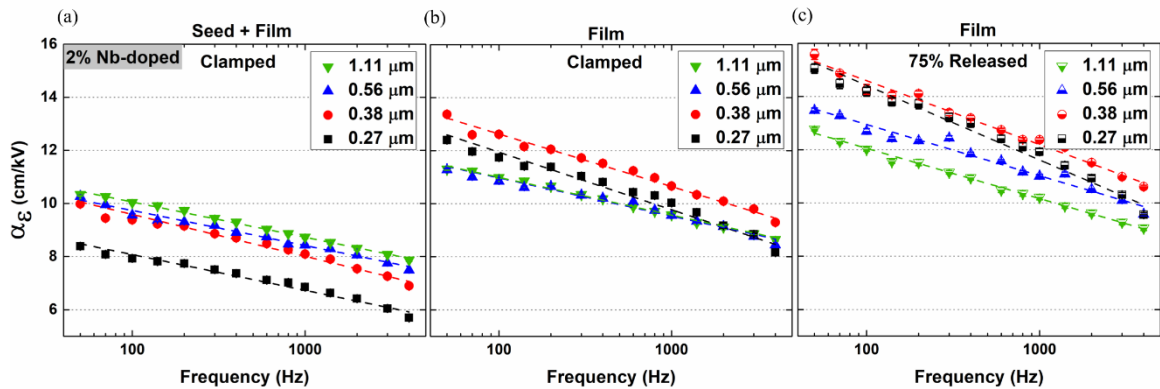


Figure 2-9: Frequency dispersion of the Rayleigh parameter α_ε as a function of film thickness ranging from 0.27 μm to 1.11 μm for PZT 30/70 thin films doped with 2% Nb in the clamped state before applying the capacitor in series model (Seed + Film) (a), in the clamped state after applying the model (Film) (b) and in the 75% released state after applying the model (c).

Rayleigh parameters of the PZT film, after application of the capacitor-in-series model, were calculated for each film thickness. For simplicity, the Rayleigh parameters prior to applying the capacitor in series model are labeled as ‘Seed + Film’ in **Figure 2-9** (a), and the data after applying the capacitor in series model are labeled as ‘Film’ in **Figure 2-9** (b). For the Nb-doped films, the seed layer has a large effect on the irreversible Rayleigh coefficient. The α_ε for the PZT film alone is 51% larger than the α_ε measured for the film in series with the seed layer. The difference in α_ε occurs over the entire frequency range for each film thickness.

Without the influence of the seed layer, α_ε values for the 1.11 and 0.56 μm films converge, which suggests that these films have comparable domain wall pinning effects.

However, the thickness dependence of α_ε is still present in thicknesses below 0.56 μm . Additionally, the α_ε values for the 1.11 and 0.56 μm films are lower than those for 0.38 and 0.27 μm films at low frequencies. The origin of this difference is unknown but could be related to a difference in stress level associated with the domain state, as discussed in Chapter 3 of this thesis.

2.3.2.2 Thickness Dependence in Released Films

To assess whether the suppression of α_ε is influenced by substrate clamping, Rayleigh parameters were obtained for films that were partially released from the substrate. Prior to the Rayleigh measurements, the films were subject to high applied electric fields (up to $3 \cdot E_c$) to induce tearing of the diaphragms and create globally released regions.[51] All films exhibited tearing of the diaphragms with variations in the number of tears and the angle of the tear with respect to the horizontal length of the etch pits. However, most electrodes have one tear at each end of the diaphragm regardless of film thickness. The tear typically occurs at the curved ends of the rounded, beam-like etch pits and propagates horizontally towards the electrode edges, shown in the FESEM micrograph of **Figure 2-10**. *In situ* synchrotron XRD measurements confirm that, upon global release, enhanced ferroelastic reorientation occurs in PZT 30/70 thin films compared to either local released or clamped states. The enhanced properties in a globally released film are due to the reduction in the average, global tensile stress of the film.[51] After global release, all samples were annealed at 400°C for 30 min. and aged for 24 hours prior to Rayleigh analysis.

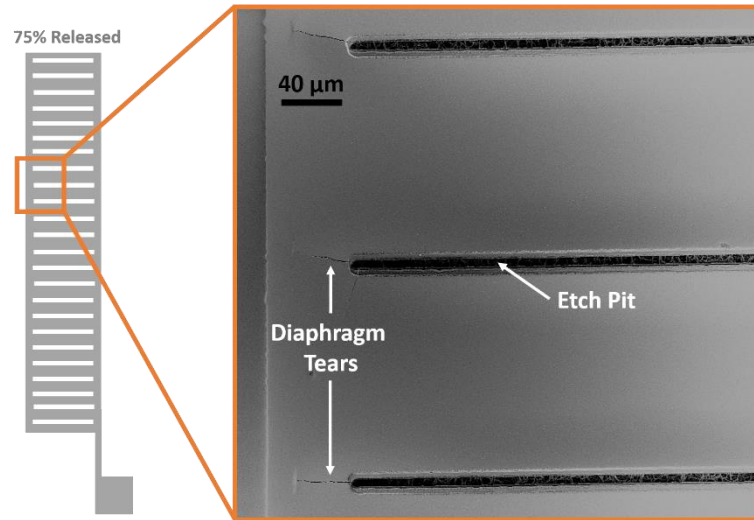


Figure 2-10: A micrograph of the torn electroded regions extending from the etch pit after global released.

To isolate the influence of substrate clamping on the thickness dependence, the trends in α_ε were analyzed for a 75% released film after applying the capacitor in series model. Upon 75% release, α_ε increases by up to 23%, with larger changes for the thinner films, shown in **Figure 2-9** (c) for Nb-doped films. Additionally, the evolution of α_ε with increasing release state is shown for 0.27 μm 2% Nb-doped film in **Figure 2-11**.

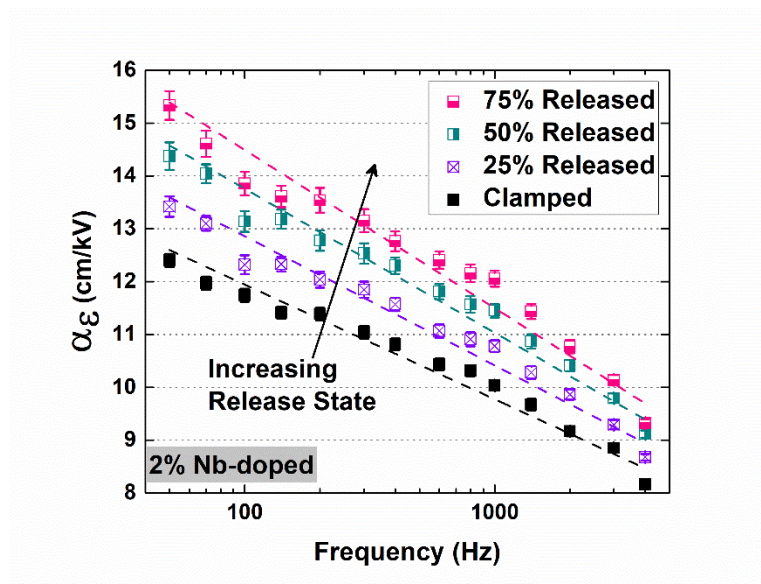


Figure 2-11: Frequency dispersion of the Rayleigh parameter α_ε as a function of release state including clamped or 0% released, 25% released, 50% released and 75% released from the substrate for 0.27 μm thick PZT 30/70 thin film doped with 2% Nb.

2.3.3 Frequency Dependence of α_ε

After applying the capacitor in series model to a clamped Nb-doped film, the greatest increase in α_ε occurs at low frequencies, shown in **Figure 2-12**. This indicates that changes in α_ε are also frequency-dependent as well as thickness-dependent. The frequency dependence (B_{α_ε}) of the Rayleigh coefficient α_ε was extracted from fits to Equation 2-3.

$$\alpha_\varepsilon = \alpha_{\varepsilon,i} - B_{\alpha_\varepsilon} \log f \quad \text{for frequencies in Hz} \quad 2-3$$

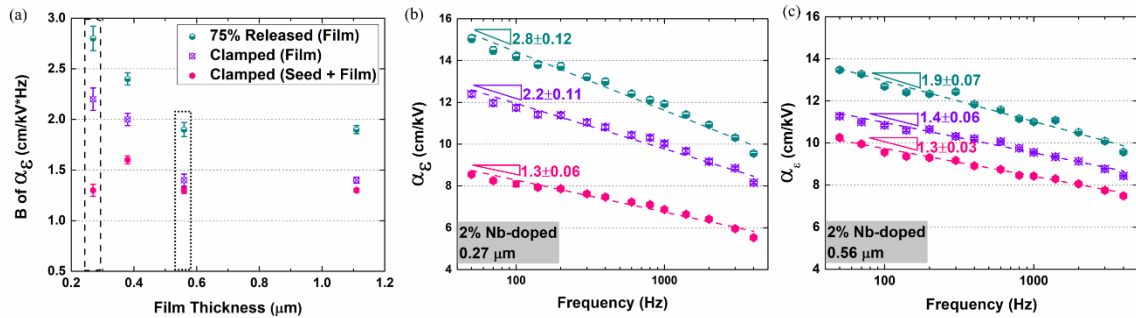


Figure 2-12: Frequency dependence (B) of the Rayleigh parameter α_ε as a function of film thickness for PZT 30/70 thin films doped with 2% Nb (a) for the clamped state before applying the capacitor in series model (Seed + Film), the clamped state after applying the model (Film), and the 75% release state after applying the model. The dashed and dotted boxes represent values of $B(\alpha_\varepsilon)$ for the 0.27 and 0.56 μm films, respectively. Complementary frequency dispersion of the Rayleigh parameter α_ε are also shown for thickness 0.27 μm (b) and 0.56 μm (c).

The frequency dependence in α_ε is unknown, but it is speculated that it may be related to the differences in the mobility of domain wall clusters of different sizes. Domain walls tend to move in clusters; [45][54] larger clusters may be active at lower frequencies. As frequency rises, the size of the responding cluster may drop. This would account for the frequency dependence in α_ε at these comparatively low frequencies, as shown in **Figure**

2-12. It is notable that the frequency dependence observed here at well below the $\sim 1 - 10$ GHz range at which motion of individual domain walls would be expected to freeze out.

After applying the capacitor in series model, B_{α_ε} increases, shown in **Figure 2-12** (a) for Nb-doped films. Additionally, larger changes in B_{α_ε} are observed for films below $0.5 \mu\text{m}$ in thickness. This is highlighted in the comparison between the $0.27 \mu\text{m}$ and $0.54 \mu\text{m}$ films, shown in **Figure 2-12** (b-c). A $\sim 69\%$ increase in the frequency dependence of α_ε occurs for a $0.27 \mu\text{m}$ Nb-doped film (b) compared to a $\sim 8\%$ increase for $0.56 \mu\text{m}$ Nb-doped film (c).

Upon 75% release from the substrate, B_{α_ε} increases further for all film thicknesses, as shown in **Figure 2-12** (a) for Nb-doped films. Upon release, a greater increase in α_ε occurs at low frequencies, resulting in an increase in B_{α_ε} . However, the change in B_{α_ε} upon release does not vary greatly with film thickness.

2.3.4 Intrinsic and Reversible Contributions to Permittivity

2.3.4.1 Thickness Dependence in Clamped Films

The thickness dependence in the intrinsic response and the reversible contributions to the dielectric response is represented in the Rayleigh parameter $\varepsilon_{initial}$. For clamped Nb-doped PZT films, $\varepsilon_{initial}$ varies non-monotonically as a function of film thickness, shown in **Figure 2-13** (a), presumably because of differences in the film domain state. The volume fraction of c -domains (ν_{002}) increases as film thickness increases from 0.27 to $1.11 \mu\text{m}$ for 2% Nb-doped films, as shown in **Figure 2-5** (d). This higher concentration of c -domains in thicker films is consistent with findings from the literature.[69] The resulting

decrease in the intrinsic contribution to the relative permittivity is reflected in the decrease in the $\epsilon_{initial}$ above $0.38 \mu\text{m}$.

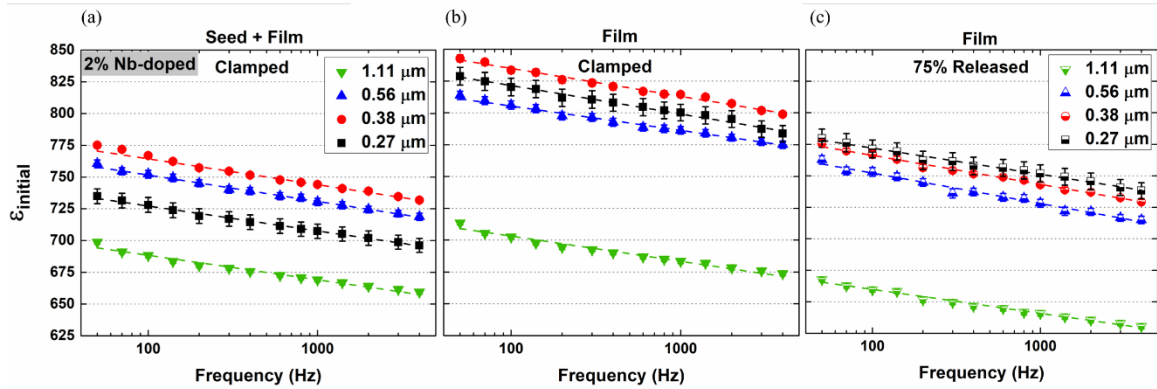


Figure 2-13: Frequency dispersion of the Rayleigh parameter $\epsilon_{initial}$ as a function of film thickness ranging from $0.27 \mu\text{m}$ to $1.1 \mu\text{m}$ for PZT 30/70 thin films doped with 2% Nb in the clamped state before applying the capacitor in series model (Seed + Film) (a), in the clamped state after applying the model (Film) (b) and in the 75% released state after applying the model (c).

Rayleigh parameters for clamped, Nb-doped PZT films without the influence of the seed layer are shown in **Figure 2-13** (b). $\epsilon_{initial}$ increases after the applying the capacitor in series model by up to 13%. $\epsilon_{initial}$ values for the 0.56 , 0.38 and $0.27 \mu\text{m}$ films approach convergence, suggesting that the films have comparable domain populations, as well as comparable reversible domain wall contributions to $\epsilon_{initial}$. However, the $1.11 \mu\text{m}$ film maintains much lower $\epsilon_{initial}$ values due to the greater volume fraction of c -domains.[70]

2.3.4.2 Thickness Dependence of Released Films

Figure 2-13 (c) shows the influence of 75% release on $\epsilon_{initial}$ for the thickness series of Nb-doped films. Upon release, $\epsilon_{initial}$ decreases as film thickness increases from 0.27 to $1.11 \mu\text{m}$. This thickness dependence of $\epsilon_{initial}$ for the 75% released film is influenced by intrinsic contributions, i.e. the change in volume fraction of c -domains as a function of thickness, since an increasing volume fraction of c -domains will decrease the permittivity.

Interestingly, $\epsilon_{initial}$ decreases with increasing release state for a given film thickness, as shown in **Figure 2-14** for the 0.27 μm film doped with 2% Nb. It has previously been reported that the release process itself does not change the volume fraction of c -domains at zero applied electric field.[51] Therefore, the observed decrease in $\epsilon_{initial}$ upon release may suggest that there is a shift of at least some of the domain walls from reversible motion in a clamped film to irreversible motion in a released film.

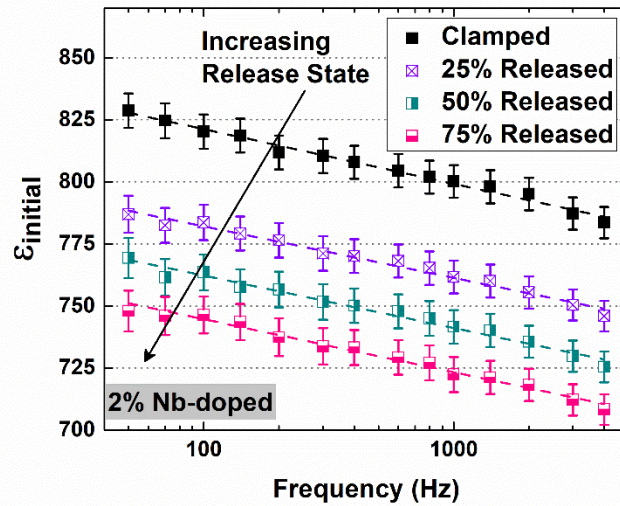


Figure 2-14: Frequency dispersion of the Rayleigh parameter $\epsilon_{initial}$ as a function of release state including clamped or 0% released, 25% released, 50% released and 75% released from the substrate for 0.27 μm thick PZT 30/70 thin film doped with 2% Nb.

2.3.5 Frequency Dependence of $\epsilon_{initial}$

Removing the influence of the seed layer by applying the capacitor in series model produces little to no change in $B_{\epsilon_{initial}}$, regardless of film thickness, as shown in **Figure 2-15**. Upon 75% release from the substrate, there is little to no change in $B_{\epsilon_{initial}}$, regardless of film thickness, also shown in **Figure 2-15**. Notably, the changes in B_{α_ϵ} upon release exceed changes in $B_{\epsilon_{initial}}$. The frequency dependence of nonlinearity for α_ϵ and $\epsilon_{initial}$

are listed in **Table 2-2** and **Table 2-3**, respectively, for all film thicknesses in the clamped state before the capacitor in series model was applied, the clamped state after the model was applied and the 75% release state after the model was applied.

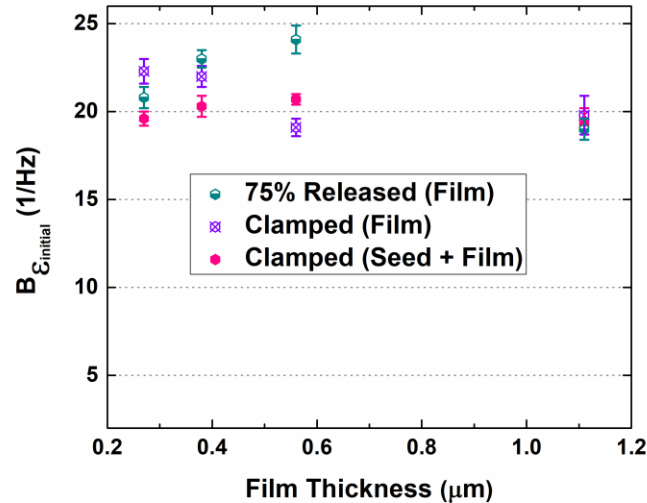


Figure 2-15: Frequency dependence (B) of the Rayleigh parameter $\epsilon_{\text{initial}}$ as a function of film thickness for PZT 30/70 thin films doped with 2% Nb for the clamped state before applying the capacitor in series model (Seed + Film), the clamped state after applying the model (Film) and the 75% release state after applying the model.

Thickness (μm)	Clamped (Seed + Film)		Clamped (Film)		75% Released (Film)	
	A	B	A	B	A	B
1.11	12.7 ± 0.06	1.3 ± 0.02	13.8 ± 0.07	1.4 ± 0.03	15.8 ± 0.12	1.9 ± 0.04
0.56	12.4 ± 0.11	1.3 ± 0.03	13.8 ± 0.19	1.4 ± 0.06	16.8 ± 0.22	1.9 ± 0.07
0.38	12.7 ± 0.13	1.6 ± 0.04	16.6 ± 0.19	2.0 ± 0.06	19.4 ± 0.19	2.4 ± 0.06
0.27	10.8 ± 0.18	1.3 ± 0.06	16.3 ± 0.32	2.2 ± 0.11	20.0 ± 0.36	2.8 ± 0.12

Thickness (μm)	Clamped (Seed + Film)		Clamped (Film)		75% Released (Film)	
	A	B	A	B	A	B
1.11	727 ± 2.4	19.3 ± 0.9	742 ± 2.7	19.8 ± 1.1	698 ± 1.6	19.0 ± 0.6
0.56	793 ± 0.9	20.7 ± 0.3	843 ± 1.5	19.1 ± 0.5	800 ± 2.3	24.1 ± 0.8
0.38	805 ± 1.8	20.3 ± 0.6	879 ± 1.8	22.0 ± 0.6	812 ± 1.4	23.0 ± 0.5
0.27	766 ± 1.2	19.6 ± 0.4	866 ± 2.1	22.3 ± 0.7	813 ± 1.7	20.8 ± 0.6

2.4 Discussion

2.4.1 Capacitor-in-Series Model

The difference in α_ε ($\Delta\alpha_\varepsilon$) between the total measured response and the response after applying a capacitor in series model represents the decoupling of the film properties and the seed layer properties, as shown in **Figure 2-16** (a). The increase in α_ε after applying the model suggests that the seed layer contributes directly to the pinning of irreversible domain walls and/or it reduces the field across the balance of the film (which commensurately reduces the domain wall contributions to the properties). Defect dipoles associated with the Mn doping of the seed layer PZT solution, such as $Mn''_{Ti} - V_O''$ or $Mn'_{Ti} - V_O''$, are assumed to be present and create internal electric fields that pin domain walls. Additionally, larger increases in α_ε were observed for the thinner films which are more influenced by the seed layer properties in which the seed layer makes up a larger fraction of the total thickness.

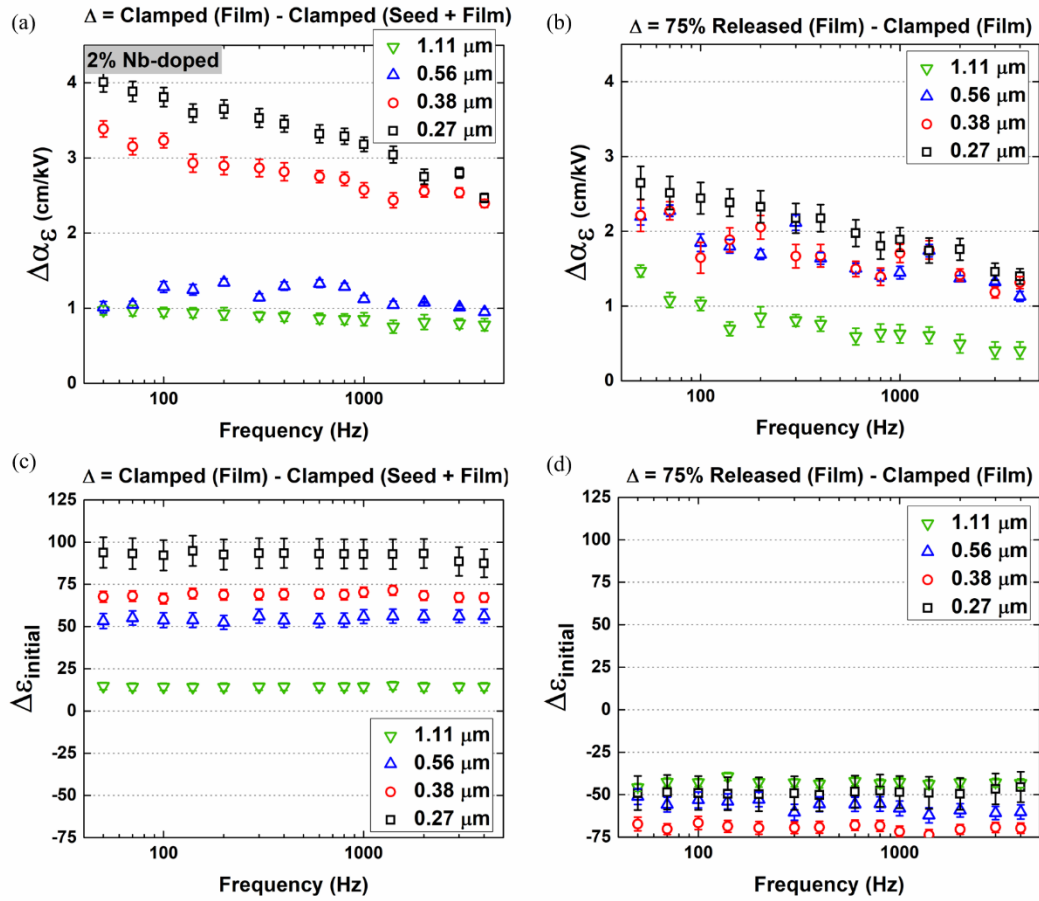


Figure 2-16: The change in the Rayleigh parameters α_ϵ (a-b) and $\epsilon_{\text{initial}}$ (c-d) as a function of film thickness for PZT 30/70 thin films doped with 2% Nb. (a, c) Represents the change after applying the capacitor in series model. (b, d) Represents the change upon release.

For the 1.11 and 0.56 μm films, $\Delta\alpha_\epsilon$ is larger at lower frequencies compared to higher frequencies, relating to an increase in B_{α_ϵ} . A larger $\Delta\alpha_\epsilon$ at lower frequencies indicates that the seed layer preferentially influences the mobility or density of slower moving irreversible domain walls that are active at lower frequencies. In contrast, $\Delta\epsilon_{\text{initial}}$ does not vary as a function of frequency, as shown in **Figure 2-16** (c). $\Delta B_{\epsilon_{\text{initial}}}$ are representative of changes in the reversible domain wall contributions, as intrinsic contributions should be constant in this frequency range. Therefore, the lack of change in

$B_{\epsilon_{initial}}$ compared to that for $B_{\alpha_{\epsilon}}$ indicates that the seed layer has a greater impact on irreversible domain wall motion compared to reversible domain wall motion.

2.4.2 Substrate Clamping Effects

In general, α_{ϵ} increases upon 75% release from the substrate. It is proposed that the potential energy barrier for irreversible domain wall motion decreases upon release, the concentration of pinning sites due to substrate clamping decreases upon release which allows for an increase in domain wall motion, or the mobility of existing domain walls increase. $\Delta\alpha_{\epsilon}$ upon release is greater for thinner films compared to thicker films, as shown in **Figure 2-16** (b). Strain relaxation upon release from the substrate could be a possible explanation for this trend. Due to the thermal expansion coefficient mismatch between the PZT film and the Si substrate, an in-plane tensile strain in the PZT film develops upon cooling, with a greater amount of thermally-induced strain reported in thinner films compared to thicker films.[33][71] Variations in the thermal strain as a function of film thickness could also explain the observed change in ν_{002} of a clamped film as film thickness increases.

Additionally, $\Delta\alpha_{\epsilon}$ is larger at lower frequencies compared to higher frequencies, as reflected by an increase in $B_{\alpha_{\epsilon}}$ upon release. This confirms that substrate clamping also preferentially influences the mobility or density of slower moving irreversible domain walls, contributing to the suppression of $B_{\alpha_{\epsilon}}$. Upon release, either the mobility of the existing domain walls active at lower frequencies rises, or some of the slower moving domain walls are depinned. This is not the case for reversible domain wall motion

contributions. Upon release, $\Delta\varepsilon_{initial}$ does not vary as a function of frequency, as shown in **Figure 2-16** (d). Since the changes in frequency dependence are representative of changes in the reversible domain wall motion contributions, substrate clamping also has a greater impact on irreversible domain wall motion compared to reversible domain wall motion.

2.5 Conclusions

Rayleigh analysis was used to investigate the influence of substrate clamping on the extrinsic contribution to the relative permittivity of PZT thin films doped with 2% Nb for a film thickness range of 0.27 μm to 1.1 μm . These results indicate that both the seed layer and substrate clamping accounted for a substantial apparent suppression of the extrinsic contribution to the relative permittivity. It was found that irreversible domain wall motion contributions to the relative permittivity (α_ε) decrease as film thickness decreases, consistent with findings in the literature. The suppression of α_ε is partially recoverable by (1) removing the influence of the seed layer via a capacitor in series model and (2) reducing the substrate clamping. The need for a capacitor in series model to account for the seed layer properties will depend explicitly on processing conditions and, therefore, should always be checked. After removing the influence of a Mn-doped seed layer, the α_ε for the PZT film alone is 51% larger than the α_ε measured for the film in series with the seed layer; this is attributed to the film having a higher irreversible domain wall motion contribution to the permittivity compared to the seed layer. Upon 75% release from the substrate, α_ε increased further by up to 23%. Finally, the frequency dependence of α_ε increases upon release due to depinning of slower moving irreversible domain walls.

Chapter: 3 Residual Stress and Ferroelastic Domain Reorientation in Declamped {001} Pb(Zr_{0.3}Ti_{0.7})O₃ Films

3.1 Introduction

Ferroelectric materials are utilized in applications such as actuators, sensors and nonvolatile memory.[3] Typically, the dielectric and piezoelectric responses in ferroelectric thin films are suppressed relative to their bulk counterparts due to a combination of small grain sizes, thermal strains, clamping due to the substrate, and the potential for a high concentration of defects. [33][38][34][72][73][74]

In ferroelectrics, residual stresses can dictate preferred domain distributions.[75] In many ferroelectric films, the substrate has a strong influence on the domain configuration.[76] For example, preferential out-of-plane polarization can be achieved for relaxed, tetragonal Pb(Zr_xTi_{1-x})O₃ (PZT) films grown on sapphire, MgO or LaAlO₃, which have a larger coefficient of thermal expansion compared to PZT. [74][75][76][77] This type of domain configuration is ideal for applications such as FeRAM which utilize out-of-plane polarization switching for memory.[78]

Since the coefficient of thermal expansion (α_{CTE}) of Si (2.6 ppm/°C) is less than that of PZT in the paraelectric phase (6.7-9.4 ppm/°C depending on composition),[75] PZT films processed on Si are under an in-plane tensile stress, favoring orientation of the spontaneous polarization in-plane (e.g. producing preferentially *a* domain, rather than *c* domain films).[77][79] Moreover, local stresses can form at the film-bottom electrode interface that differ from the average residual stress, complicating the understanding. Griggio *et al.* proposed that these local strains can be partially relieved by removing the

film from the substrate.[54] The residual stress state of PZT films on Si is also reported to depend on the number of deposited layers or film thickness [30] and is correlated with variations in domain patterns.[31][80] The apparent variation in the stress state as a function of film thickness may also be associated with changes in the stress state of the underlying thermal oxide layer or Pt-bottom electrode during subsequent annealing.[81][82]

Differences in the intrinsic and extrinsic contributions to the relative permittivity (ϵ_r) will result from differences in the domain orientation state, domain wall densities, and the mobility of domain walls. This, in turn, contributes to the apparent scaling effects in the functional properties.[29][34][83] For example, PZT films which have predominately a -domains will have a larger out-of-plane intrinsic contribution to ϵ_r , possibly at the expense of a reduced 90° domain wall density and reduced extrinsic contributions to ϵ_r . [76] Therefore, variations in the in-plane stress state of PZT films can result in a thickness dependence in the domain state, intrinsic contributions and extrinsic contributions to ϵ_r .

The differences in the intrinsic and extrinsic contributions to ϵ_r can often be quantified using Rayleigh analysis.[43][47][49][83][84] The Rayleigh law is described in Equation 1-7 of Chapter 1 in this thesis. In short, $\epsilon_{initial}$ is the reversible dielectric Rayleigh coefficient and represents the sum of reversible extrinsic and intrinsic contributions to the permittivity. α_ϵ is the irreversible dielectric Rayleigh coefficient associated with extrinsic contributions to the permittivity from irreversible movement of domain walls and phase boundaries through a random potential energy landscape.[21] Rayleigh analysis cannot

differentiate between motion of 90° and 180° domain walls. Therefore, it is advantageous to couple Rayleigh analysis with another characterization technique, such as *in situ* X-ray diffraction (XRD), that can directly probe ferroelastic extrinsic contributions to the permittivity.[51][77][85][86]

The extent of electric field-induced 90° domain reorientation in most clamped PZT films is relatively small compared to bulk ceramics,[87] and a majority of the reoriented domains relax back to a remanent state as the electric field decreases to zero.[85][88] Clamping effects can be alleviated in a variety of ways that are dictated by device design and etching techniques. For example, decreasing the width:thickness aspect ratio of the piezoelectric layer can partially declamp the film and enhance piezoelectric properties.[10][53][89] Alternatively, removing the substrate via an undercut release process can also relax substrate clamping effects.[51][54][84]

Griggio *et al.* proposed that removing the substrate from underneath the film can alleviate residual stress at the film-substrate interface and may relax thermal stresses by bending.[54] However, Wallace *et al.* observed no significant changes in the volume fraction of *c*-domains (v_{002}) normal to the film surface on release of elongated diaphragms with $2\ \mu\text{m}$ thick tetragonal PZT films. Therefore, simply releasing the film from the substrate may not change the average residual stress enough to induce a change in the overall domain distribution of the film for thick, taut membranes.[51] Notably, these studies were limited to comparatively thick PZT films ($>1\ \mu\text{m}$) in which the film-substrate interface makes up a small fraction of the overall film thickness. For thinner films, Berfield *et al.* [5] attributed a substantial reduction in polarizability of sol-gel PZT films $<200\ \text{nm}$ thick to higher residual stress than that observed in thicker films. Therefore, alleviating the

residual stress at the film-substrate interface may have a larger effect on the domain distribution in thinner films ($<1 \mu\text{m}$).

If stress were the dominant effect that degrades properties in thin ferroelectric films, then it would be expected that the properties of thin films would be most affected by removal of both substrate clamping and residual stresses. Alternatively, if the defect concentration in thinner films (e.g. due to lead loss to the bottom electrode or smaller grain size) were to dominate the property suppression, then reduction of substrate clamping would be expected to produce a less-pronounced improvement in properties. Further investigation is required to assess which effect is dominant.

In this work, *in-situ* high-resolution XRD was used to directly probe the structure of ferroelectric thin films and assess the effect of substrate clamping and residual stress on the thickness dependence of the domain state, strain, and domain reorientation of PZT films for thicknesses ranging from 0.27 to 1.11 μm . The results confirm that the properties of thin clamped films are influenced both by the stress and the defect chemistry. Additionally, this study combines XRD and Rayleigh analysis to deconvolute the intrinsic and the reversible, extrinsic contribution to the dielectric permittivity and to better understand the principles governing size effects in thin films.

3.2 Experimental Procedure

3.2.1 Film Synthesis and Nanofabrication

The samples used in this study are the same samples reported in Chapter 2 of this thesis. The average grain sizes of all film thicknesses, as measured by a line intercept

method [90], are largely independent of the film thickness, as shown in **Table 3-1**. Lotgering factors for {001} reflections ranged from 90% to 100% depending on film thickness.[91]

Table 3-1: Microstructure and Electrical Properties for Clamped PZT 30/70 Films						
Thickness (μm)	P_r ($\mu\text{C}/\text{cm}^2$)	P_{max} ($\mu\text{C}/\text{cm}^2$)	E_c (kV/cm)	ϵ_r	Loss %	Columnar Grain Size (nm)
	(P _r and P _{max} measured at 400 kV/cm)					
1.11	18.1 \pm 0.2	40.0 \pm 1.2	62.5 \pm 1.4	685 \pm 1.2	1.5 \pm 0.07	134 \pm 13.5
0.56	14.1 \pm 1.2	37.9 \pm 1.8	55.5 \pm 4.5	761 \pm 2.7	2.2 \pm 0.05	97 \pm 6.8
0.38	12.6 \pm 1.3	36.8 \pm 0.7	54.1 \pm 2.6	730 \pm 1.4	2.9 \pm 0.05	101 \pm 6.2
0.27	11.1 \pm 0.2	36.5 \pm 0.5	59.2 \pm 1.0	738 \pm 5.2	3.2 \pm 0.2	117 \pm 6.6

Photolithography was used to define top electrode areas and regions on the electrodes subject to a top-down etch and undercut release process. RF magnetron sputtered platinum top electrodes were defined in 3.5 mm x 0.7 mm areas. Large electrode areas were needed to ensure that an adequate volume of irradiated material was available for actuation during *in situ* XRD measurements. As described elsewhere, the electrodes were rotated 15° from the [001] of the silicon wafer to minimize diffraction from the substrate.[51] An Ulvac NE-550 inductively coupled high-density plasma etcher was used to dry etch 600 μm x 146 μm pits through the Pt/PZT/Pt/TiO₂/SiO₂ stack, exposing the Si substrate. Top-down etching was continued using an isotropic Xactic XeF₂ e1 vapor etch tool to etch 100 μm wide trenches into the Si substrate, as described elsewhere.[51][54][83] A ‘75% release’ corresponds to an electroded region in which 75% of the Pt/PZT/PT/TiO₂/SiO₂ stack is suspended above a void in the Si substrate. The term ‘clamped’ refers to an electroded region in which no etch trenches or etch pits are present, and the film is fully clamped to

the Si substrate. The electrical properties are summarized in **Table 3-1** for all film thicknesses in the clamped state.

3.2.2 X-ray Measurements and Analysis

To study the domain reorientation at high fields, *in situ* synchrotron XRD measurements were performed at the Advanced Photon Source beamline 11-ID-C with an energy of 105.091 keV (0.117418 Å). The samples were mounted on a custom stage, which allows for *in situ* use of electrical probes with voltage produced by a Keithley 2410C 1100V source meter. To increase the diffracting volume, the sample was tilted 1° to the incident beam with slit sizes of 0.5 mm in the horizontal direction and 0.1 mm in the vertical direction. Care was taken to align the electroded area of interest to ensure that only actuated film was captured in the diffracted pattern.

Diffraction patterns were measured while applying a direct current (dc) electric field. Each film was cycled twice, using the applied voltage sequence shown in **Figure 3-1** (a). During the first cycle, an initial pattern was taken at 0 V and subsequent patterns were taken after the field was increased by steps of $0.25 \cdot E_c$ (where E_c is the coercive field) until the maximum of $1.5 \cdot E_c$ was reached. At each step, the applied field was held for 210 s, followed by a 210 s acquisition of a diffraction pattern. Subsequently, patterns were also taken after the applied field was decreased by steps of $0.5 \cdot E_c$, with a final pattern taken at 0 V. This process was repeated for the second cycle, in which patterns were acquired at increasing field steps of $0.5 \cdot E_c$ until $3 \cdot E_c$ was reached. Subsequently, patterns were also taken in decreasing field steps of $1 \cdot E_c$ until 0 V was reached.

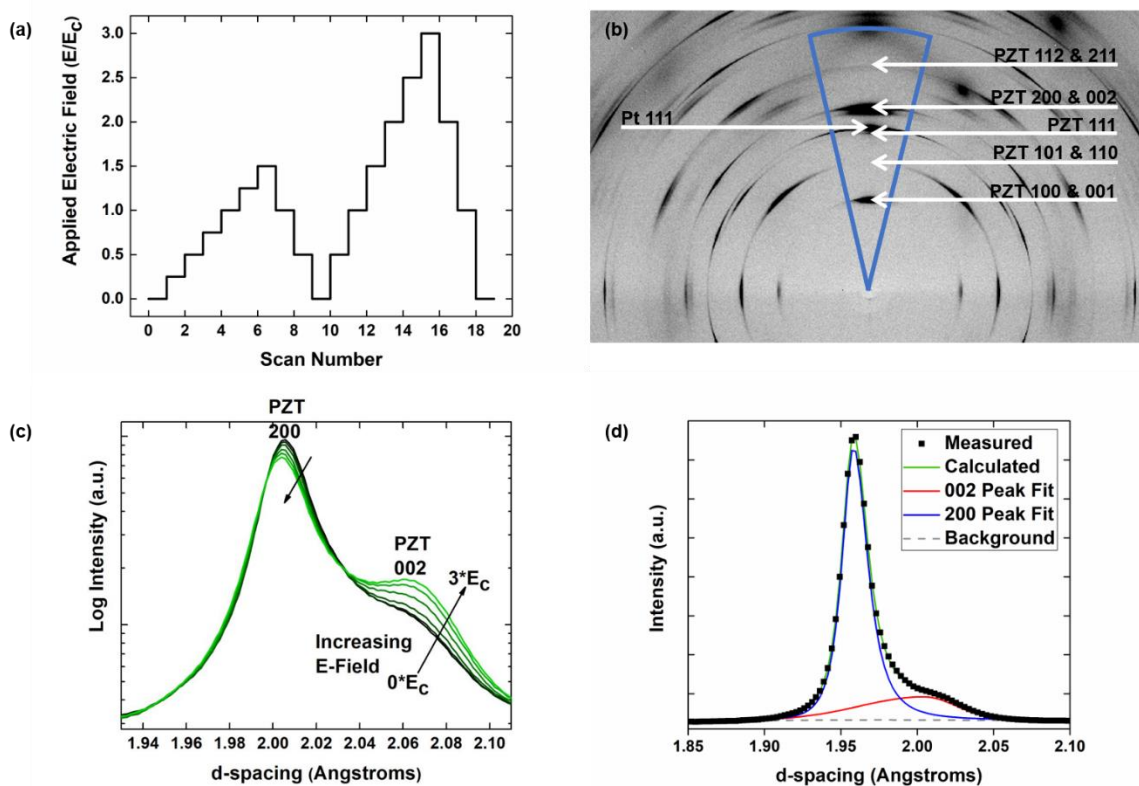


Figure 3-1: (a) A schematic of the applied electric field cycles during the in situ XRD study, (b) 2D diffraction image of the PZT 30/70 thin film with labeled reflections, (c) an example of the changes in peak intensity during application of electric field for the 1.11 μm PZT film, and (d) Asymmetric Pearson VII fits of the 002 and 200 reflections of the 1.11 μm PZT film at 0*E_c.

Line profiles were extracted from the measured 2D diffraction patterns using the *Fit2D* software (European Radiation Synchrotron Facility, Grenoble, France).[92] CeO₂ powder (NIST 674b), was used to calibrate the X-ray beam center and sample-to-detector distance, from which *d*-spacing values were calculated. The 20° sector of the 2D diffraction that represented scattering vectors parallel to the applied electric field direction (the vertical section shown in **Figure 3-1** (b)) was integrated using *Fit2D*. An example of the extracted line profiles is plotted in **Figure 3-1** (c), highlighting the changes in peak intensity of the 002 and 200 reflections as a function of applied electric field for the 1.11 μm thick film. The data were fit using LIPRAS (*Line-Profile Analysis Software*). [62] An asymmetric

Pearson VII function was applied to the 002 and 200 reflections since it accounts for peak asymmetry and approximates the diffuse scattering from ferroelectric/ferroelastic domain walls.[63] An example of the 002/200 peaks and fitting profiles is shown in **Figure 3-1** (d) for the 1.11 μm thick film at $0 \cdot E_c$.

From the peak fit, ν_{002} (the fraction of c -domains oriented in the direction normal to the film) was calculated from the integrated intensities using Equation 1-10, as described in Chapter 1 of this thesis.[22][23] The error for ν_{002} was calculated using an error propagation method that accounts for the integrated intensity error generated from peak fitting using LIPRAS. The fraction of ferroelastic domain reorientation (η_{002}), was assessed using Equation 1-9, as described in Chapter 1 of this thesis.

The d -spacings of the 002 and 200 reflections (d_{002} and d_{200} , respectively) were used to calculate the strain (ε) induced by the electric field. The calculated pattern, background and peak position generated from peak fitting using LIPRAS was used to determine the full width half maximum (FWHM) of each reflection. For example, the FWHM of the 002 is determined to be two times the 2θ distance between the central peak position and the left-hand side of the peak at the intensity value that is half the peak height. This calculation of the FWHM minimizes the error associated with the strong peak asymmetry.

To study the lattice strain at high temperatures, a PANalytical Empyrean X'Pert3 MRD laboratory diffractometer with $\text{CuK}\alpha$ radiation, 4-circle goniometer and PIXcel 3D detector was used to measure diffraction patterns at 500 $^\circ\text{C}$ for long 2θ ranges (10° - 100°). The XRD pattern was collected at a slow scan rate of $0.72^\circ/\text{min}$. Additionally, the XRD

data were utilized to evaluate the peak broadening Williamson-Hall analysis shown in Equation 3-1.[93] β_{total} is the FWHM for reflection hkl at position 2θ , λ is the X-ray wavelength of the $\text{CuK}\alpha$ radiation (1.5406 Å), K is the Scherrer constant or shape factor which was assumed to be 1, L is the effective crystallite size in the direction normal to the reflecting planes, and ε is the microstrain.[94]

$$\beta_{total} \cos \theta = 4\varepsilon \sin \theta + \frac{K\lambda}{L} \quad 3-1$$

Using this equation, a linear relationship can be made between $\sin \theta$ (plotted on the x-axis) and $\beta_{total} \cos \theta$ (plotted on the y-axis). The slope (4ε) and the y-intercept ($\frac{K\lambda}{L}$) of this linear relationship were used to determine the microstrain (ε) and crystallite size (L), respectively. The error for both ε and L is accounted for in the standard error of the linear fit.

Dielectric Rayleigh analysis was conducted on both clamped and released films at frequencies ranging from 50 Hz to 4 kHz with applied AC electric fields up to $0.5 \cdot E_c$. The samples were subjected to an anneal at 400°C for 30 min. and an aging time of 24 hours prior to the Rayleigh measurements. Subsequently, the samples were poled at $3 \cdot E_c$ for 15 min. prior to additional Rayleigh measurements. A correction was used to account for the presence of a low dielectric permittivity seed layer in series with the film.[83]

The combined electrical and structural datasets allow the possibility of separating the various contributions to the relative permittivity, assuming that each of the components is additive and that cross-coupling between the various terms can be neglected, as a first approximation. To do so, the intrinsic relative permittivity values were calculated using

Equation 1-11 described in Chapter 1 of this thesis. The dielectric susceptibility values used (χ_{11} and χ_{33}) are the free dielectric susceptibility (~ 230 and ~ 127 respectively), determined by Haun *et al.* for bulk PZT 30/70 at 25°C.[25] It is important to note that this calculation assumes a free system (fully released film) as opposed to the films in this study which are either in a clamped state or 75% released state. This approximation will overestimate the contributions from the intrinsic relative permittivity. The reversible, extrinsic contributions to the relative permittivity were calculated from Equation 1-12, as described in Chapter 1 of this thesis. Finally, the irreversible, extrinsic contributions to the relative permittivity were calculated from Equation 1-13, as described in Chapter 1 of this thesis.

3.3 Results and Discussion

3.3.1 Thickness Dependence of the Domain State

The electric field-induced change in the volume fraction of *c*-domains (v_{002}) is shown in **Figure 3-2** (a) for clamped, 2% Nb-doped PZT 30/70 thin films of thicknesses 0.27 μm , 0.56 μm , and 1.11 μm . Most of the clamped films underwent two electric field cycles.

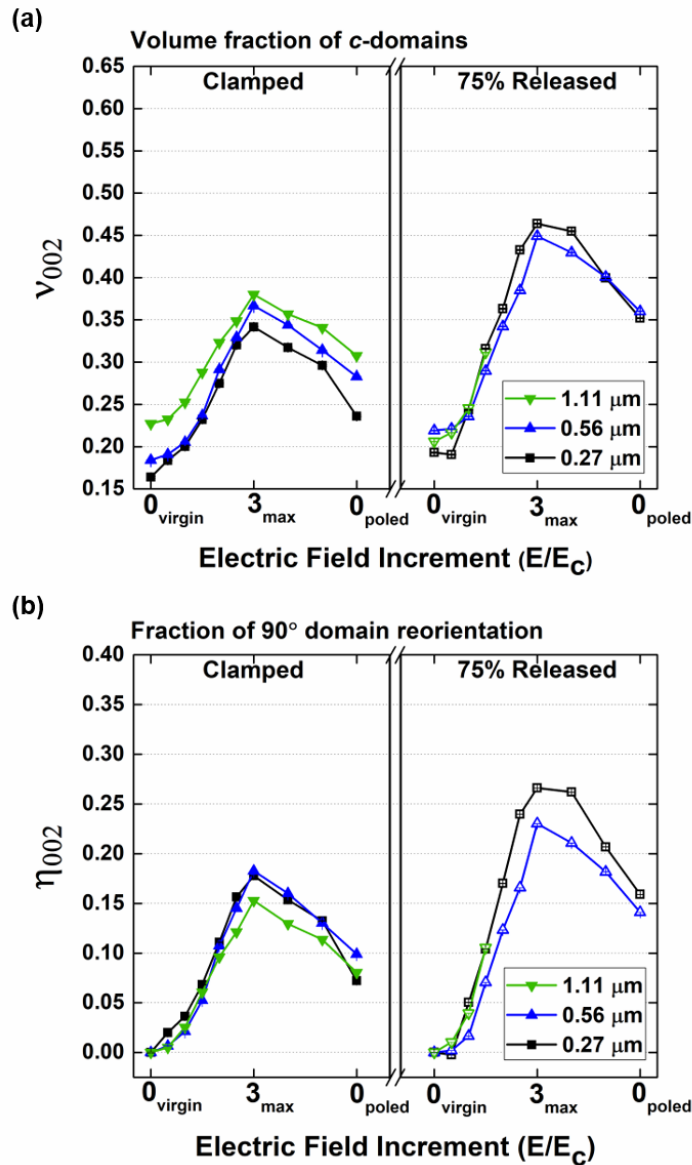


Figure 3-2: (a) The volume fraction of c -domains (v_{002}) as a function of applied electric field is shown for 2% Nb-doped PZT 30/70 thin films of thicknesses 0.27 μm , 0.56 μm , and 1.11 μm in the clamped state and in the released state. The 75% released 1.11 μm thick film exceeded a threshold current of 1×10^{-4} Amps/cm² at electric fields exceeding $2 \cdot E_c$. Therefore, the data for the released 1.11 μm film above $1.5 \cdot E_c$ were removed. (b) The fraction of 90° domain reorientation (η_{002}) as a function of applied electric field is also shown for the clamped state and the released state.

There are several important points to take from this figure. First, in the clamped virgin state, v_{002} is thickness-dependent and ranges between 0.23 (for the 1.11 μm film) and 0.16 (for the 0.27 μm film), which are comparable to those in the literature for similar

compositions, thicknesses and processing methods.[51][83] This thickness dependence of v_{002} is maintained after poling at $3*E_c$. That is, thicker clamped films have a higher volume fraction of c -domains than thinner clamped films in the initial state, during field application, and after release of field.

The thickness dependence of v_{002} develops during processing of the films.[81] For example, **Figure 3-3** shows the evolution of the normalized v_{001} during layer-by-layer processing of a $\sim 0.5 \mu\text{m}$ thick sample, in which v_{001} increases with each additional crystallized layer. Presumably, this evolution in the domain state is related to both the stress state of the film upon cooling below T_c and the defect chemistry of the interfaces.

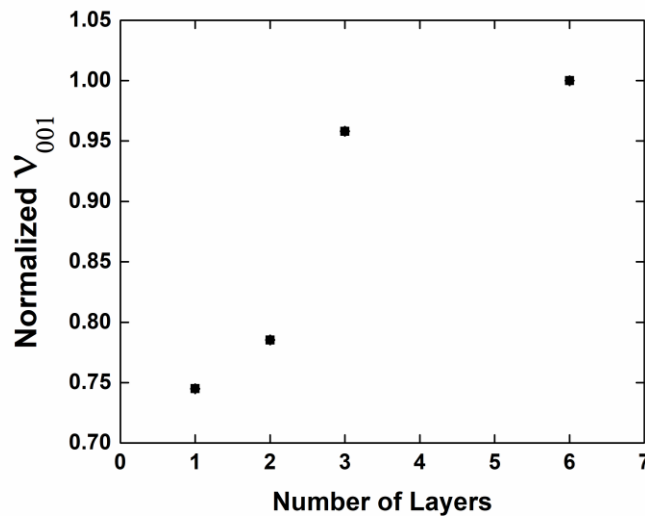


Figure 3-3: The evolution of the normalized volume fraction of c -domains (v_{001}) during layer-by-layer crystallization for 2% Nb-doped PZT 30/70 thin films processed via chemical solution deposition for thicknesses ranging from $\sim 80 \text{ nm}$ (1 layer) to $\sim 500 \text{ nm}$ (6 layers).

A second point of note from **Figure 3-2** (a) is that upon 75% release from the substrate (with an anneal above T_c), v_{002} values converge to $\sim 0.2 \pm 0.01$ for all films prior to application of an electric field. It is proposed that after a high temperature anneal, a

redistribution of the domain state occurred. The release relieves local stress at the film-substrate interface and reduces the bending rigidity of the structure. As a result, the released portions of the film experienced a different stress compared to its clamped counterpart upon cooling below T_c . Annealing above T_c allows redistribution of the domain state in the released films; whereas, when the annealing was not performed, no change in the volume fraction of c -domains was observed after films were released from the substrate.[28]

Thirdly, when an electric field is applied, a much larger volume fraction of c -domains is achieved for all film thickness in released films relative to clamped ones. This is particularly true at $3*E_c$. Above $1.5*E_c$, the diaphragms tear due to the high piezoelectric strains and release geometry.[51] After tearing, portions of the film are free to deflect vertically to relieve in-plane tensile stress, creating cantilever-like regions. This state is referred to as global release. After global release, the $0.27\ \mu\text{m}$ and $0.56\ \mu\text{m}$ thick films both show nearly 50% c -domain fractions at $3*E_c$. v_{002} are comparable for all thicknesses even after poling.

Figure 3-2 (b) shows electric field-induced changes in η_{002} for all film thickness in the clamped state and 75% released state. In the clamped state, each film experiences similar levels of ferroelastic domain reorientation during poling and similar back-switching regardless of film thickness (i.e. the relaxation of reoriented domains back to a remanent state as the electric field decreases to zero). These results suggest that substrate clamping acts as the dominant restoring force for back switching in clamped films. η_{002} is ~ 0.18 at $3*E_c$ which is almost four times larger than what has been previously reported for $\sim 1.9\ \mu\text{m}$ thick clamped 1% Mn-doped PZT 30/70 films.[51] The enhanced domain reorientation in the 2% Nb-doped PZT films of the present study is consistent with softening of the

electromechanical response. Additionally, after release, all film thicknesses have comparable electric field-induced changes in η_{002} , as shown in **Figure 3-2** (b). As expected, more domain reorientation is observed in released films than in clamped ones.[51]

3.3.2 *Thickness Dependence of Residual Stress*

In the clamped state, the thinnest 0.27 μm film has the smallest out-of-plane d-spacing for *a* and *c*-domains, d_{200} and d_{002} respectively, as shown in **Figure 3-4**. The domains present in an as-processed, clamped film are under in-plane tensile stress due to a variety of factors including strain related to defect concentrations and thermal strain formed due to the thermal expansion coefficient mismatch between the film and the substrate.

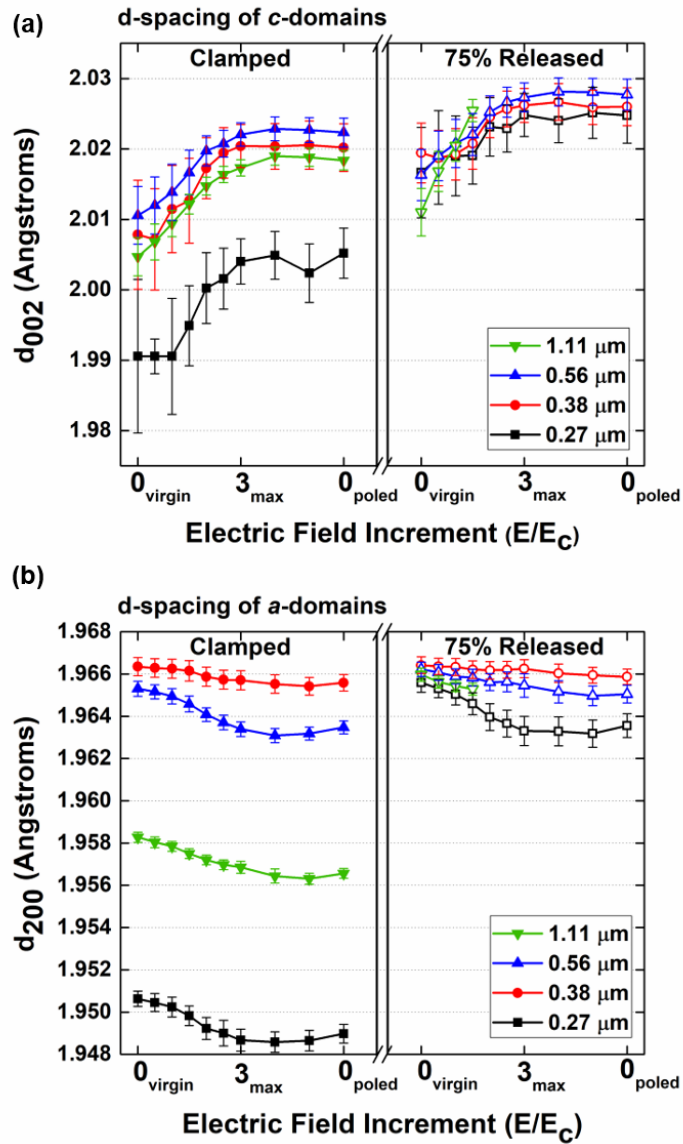


Figure 3-4: The d -spacing for the 002 (a) and 200 reflections (b) (d_{002} and d_{200} , respectively) as a function of applied electric field increment for 2% Nb-doped PZT 30/70 thin films of thicknesses 0.27 μm , 0.38 μm , 0.56 μm , and 1.11 μm in the clamped state and the 75% released state are shown.

Thinner films experience a greater in-plane tensile stress that develops upon cooling below T_c which contributes to smaller out-of-plane lattice (d) spacings for the 0.27 μm film.[30] Additionally, since a thickness dependence in the d spacings persist above T_c , as shown in **Figure 3-5**, a greater concentration of defects in thinner films also contributes to

smaller d spacings for the 0.27 μm film. The d spacings were determined from the peak fit of the 002 cubic reflection which was relatively symmetric at 500 $^{\circ}\text{C}$. Thus, the thickness dependence in the out-of-plane lattice spacings for clamped films is attributed to both a larger in-plane tensile stress and a higher concentration of defects in thinner films. This would be consistent with the data of Berfield *et al.* [5] suggesting that chemical solution derived PZT films ~ 200 nm thick have higher in-plane tensile stresses than thicker films when grown on Pt-coated Si substrates.

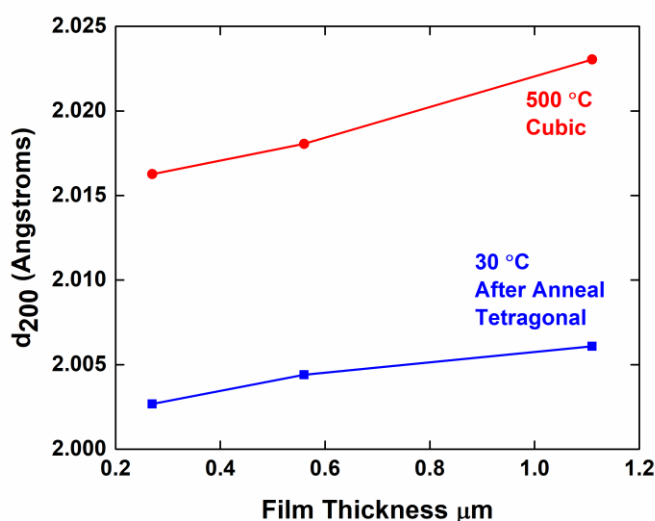


Figure 3-5: The thickness dependence of d -spacing for the 200 reflection (d_{200}) for 2% Nb-doped PZT 30/70 thin films of thicknesses 0.27 μm , 0.56 μm , and 1.11 μm at room temperature (30 $^{\circ}\text{C}$) and above the tetragonal to cubic phase transition temperature (500 $^{\circ}\text{C}$).

Interestingly, d_{200} does not monotonically increase with increasing thickness from 0.27 to 1.11 μm , shown in **Figure 3-4** (b). The films reported in this study have smaller out-of-plane lattice parameters compared to their bulk counterpart due to the in-plane tensile stress that PZT experiences when processed on a Si substrate. If the in-plane tensile stress decreases with increasing film thickness, as suggested elsewhere[81], it should be reflected

in a gradual increase in d_{200} . Additionally, at elevated temperatures above T_c , d -spacing is also observed to increase with increasing thickness for these films. However, at room temperature, **Figure 3-4** (b) shows that the d_{200} increases sharply as film thickness increases from 0.27 μm to 0.38 μm , then decreases as film thickness increases further from 0.38 μm to 1.11 μm . Reasons for this are unclear, but these changes are consistent with a reported decrease in the reversible Rayleigh coefficient with increasing thickness for films >0.38 μm .^[83] This suggests that competing factors may influence the thickness dependence of d_{200} .

For both clamped and released films, d_{002} increases with increasing applied electric field as shown in **Figure 3-4** (a). A complete data set of d_{002} and d_{200} as a function of applied field for all film thicknesses is shown in **Figure 3-6**, along with those of bulk ceramics of similar composition.^[95] The field-induced changes in d_{002} are substantially too large to be due only to the intrinsic piezoelectric response, as the required $d_{33,f}$ on increasing field would need to exceed ~ 250 pm/V in the clamped films. Moreover, the d_{002} values do not recover when the field is removed.

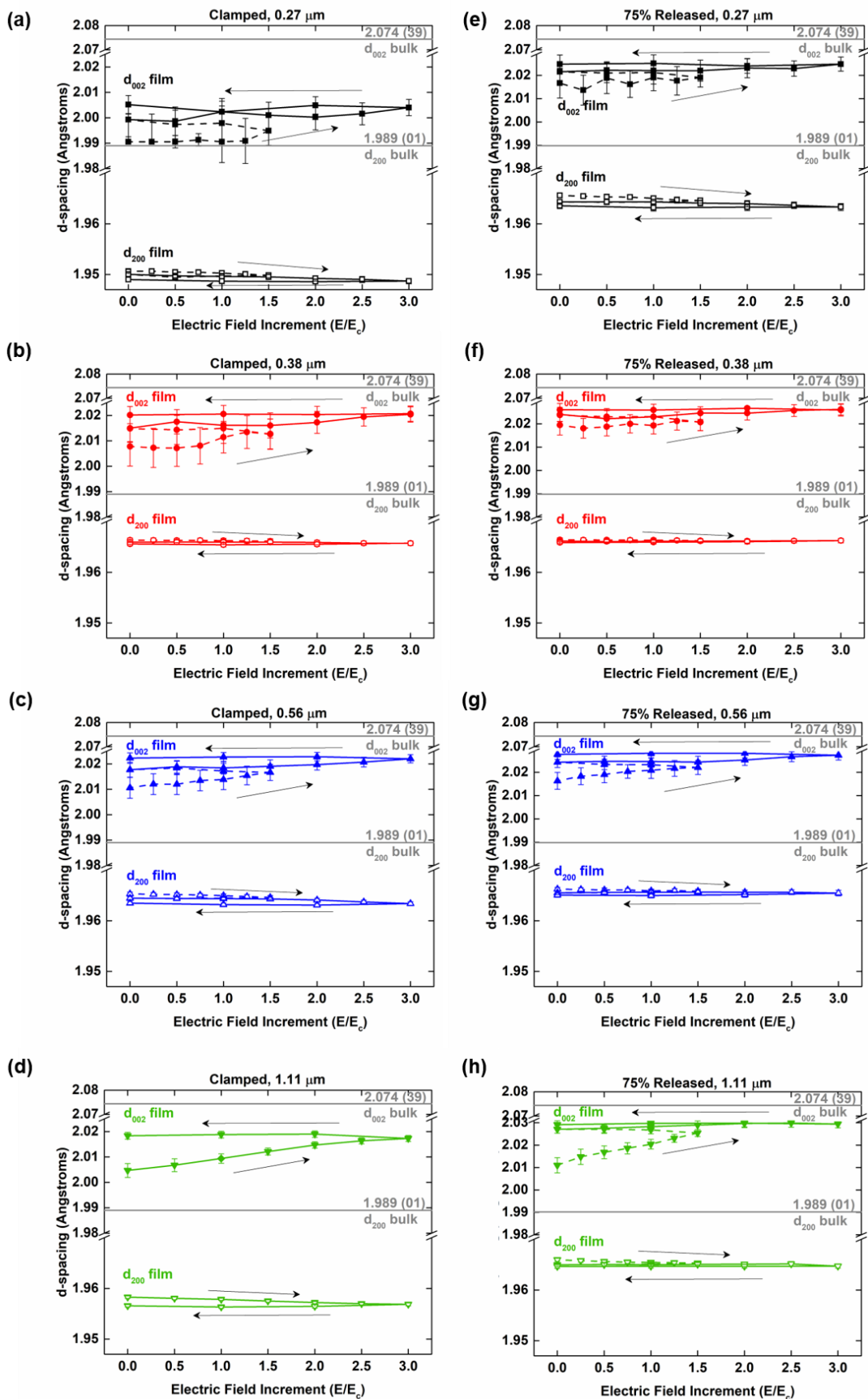


Figure 3-6: The d -spacing for the 002 and 200 reflections (d_{002} and d_{200} , respectively) as a function of applied electric field increment for 2% Nb-doped PZT 30/70 thin films of thicknesses (a,e) 0.27 μm , (b,f) 0.38 μm , (c,g) 0.56 μm , and (d,h) 1.11 μm in the clamped state and the 75% released state are shown and compared to d -spacing values for their bulk counterparts.

Under applied electric fields, re-writing the domain state will change both the residual stress state of the film and the domain size. For example, d_{002} increases with increasing applied electric fields whereas d_{200} decreases. It is notable that the increase in d_{002} is accompanied by a reduction in the full width half maximum (FWHM) of the 002 peak, while the FWHM of the 200 peak increases on poling, as shown in **Figure 3-7** (a) for a clamped 1.11 μm thick film. This suggests that the c -domains coarsen on poling, as shown schematically in **Figure 3-8**.

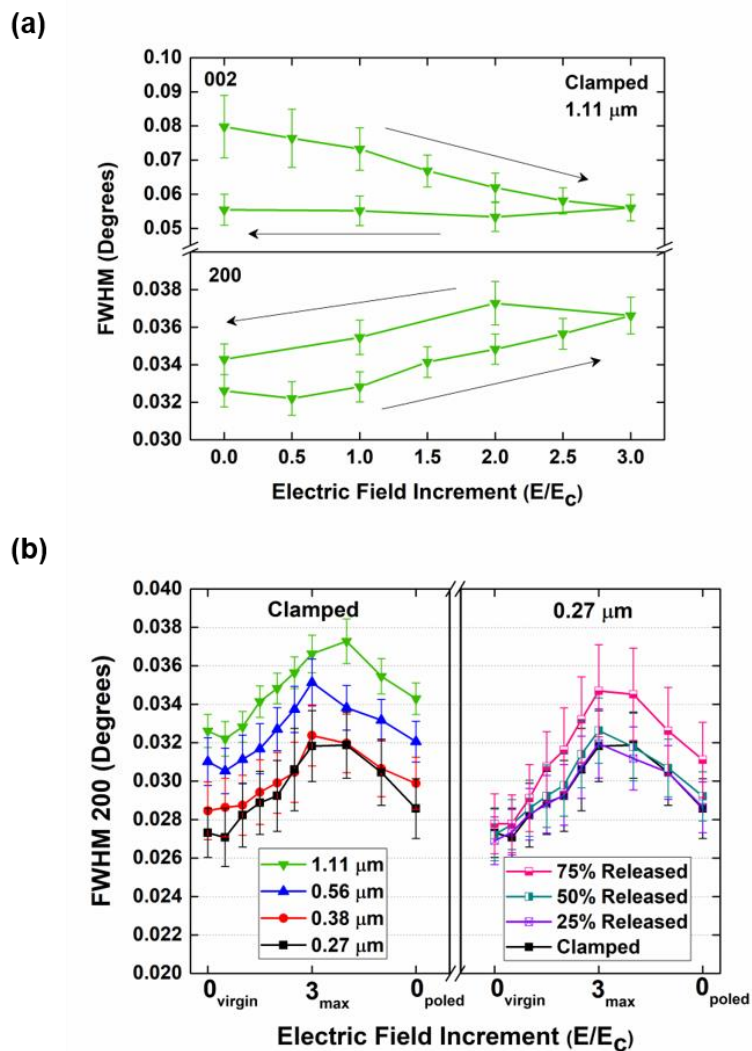


Figure 3-7: (a) The full width half maximum (FWHM) for the 002 and 200 reflections as a function of applied electric field is plotted for 2% Nb-doped PZT 30/70 thin films of thicknesses 1.11 μm . (b) FWHM for the 200 reflection as a function of applied electric field is plotted for clamped films of thicknesses ranging from 0.27 μm to 1.11 μm (left); and FWHM for the 200 reflection as a function of applied electric field is plotted for the 0.27 μm film for all release states (right).

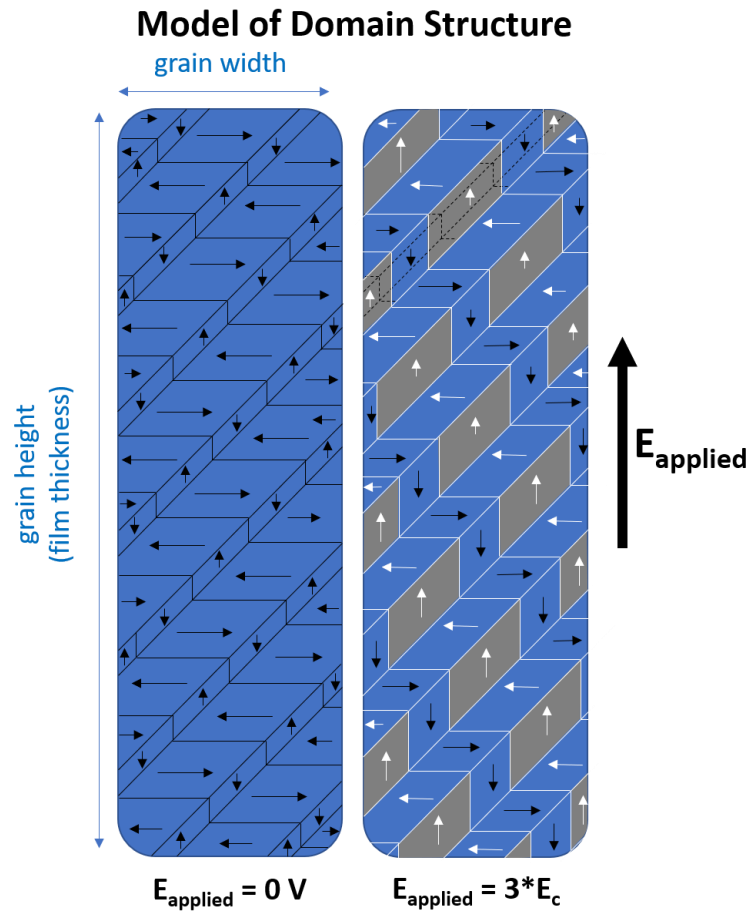


Figure 3-8: A model of the domain structure within one grain before (left) and after (right) poling to $3 * E_c$. In general, the volume fraction of c -domains increases, and the c -domains coarsen upon application of electric field.

As the c -domains coarsen, they begin to approach the d -spacing values for powders of the same composition. This is presumably the cause of the irreversible strains in d_{002} on poling. After ferroelastic switching occurs, unswitched a -domains are placed under further in-plane tension by neighboring c -domains reoriented by the applied electric field. As a result, d_{200} decreases. This is observed for tetragonal PZT thin films as an anisotropic electric field induced change in the out-of-plane d -spacings.[96] Additionally, the FWHM of the a -domains increases irreversibly upon application of electric field, presumably due to the microstrain that develops during irreversible 90° switching. Since some 90° domain

reorientation is not recoverable, the residual strain associated with ferroelastic switching results in an irreversible change in d_{002} , d_{200} , FWHM of 002 and FWHM of 200.

In general, the FWHM of the 200 is smaller than that of the 002, as shown in **Figure 3-7** (a) for the 1.11 μm thick film (and was true for all film thicknesses). Additionally, the FWHM of 200 increases as film thickness increases, as shown in Fig. **Figure 3-7** (b). Moreover, the thickness dependence in the FWHM of 200 is maintained even after poling.

Williamson-Hall analysis was used to determine the origin of the thickness dependence in the FWHM of 200.[93][94] **Figure 3-9** shows that both the microstrain and crystallite size of *a*-domains increases as thickness increases. These values are comparable to microstrain and crystallite sizes reported in other studies of PZT thin films grown on Si substrates using CSD, which also report an increase in crystallite size and microstrain as film thickness increases from 0.35 μm to 0.54 μm .[97]

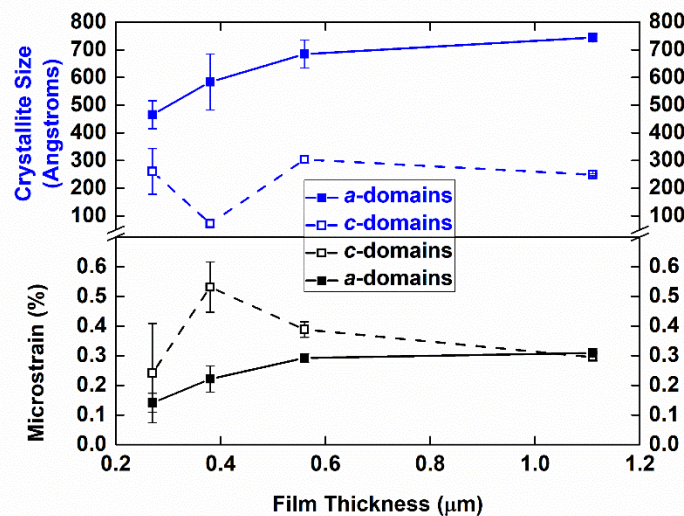


Figure 3-9: The crystallite size and microstrain as a function of film thickness for 2% Nb-doped PZT 30/70 thin films in the clamped, unpoled state.

The increase in microstrain of a -domains with film thickness may be correlated with the increase in ν_{002} . The local stress state of the film changes to accommodate an increase in ν_{002} . The dependence of microstrain on domain state has also been reported for PZT films grown in single-crystal MgO(100) substrates via pulsed laser deposition.[98]

In general, the crystallite size of a -domains are at least two times as large as c -domains. Therefore, tetragonal PZT films that are under in-plane tensile stress favor a greater volume fraction of a -domains as well as larger a -domain crystallites, as shown schematically in **Figure 3-8**. Similar to thickness-dependent trends in microstrain, the crystallite size of a -domains increases with increasing film thickness. Therefore, the thinnest 0.27 μm film presumably has the largest domain wall density, due to its small crystallite size. These results suggest that the reported Rayleigh coefficients (α_ε and $\varepsilon_{initial}$) for the clamped, unpoled 0.27 μm film are larger relative to thicker films due in part to the greater domain wall density present in the film.[83]

Releasing from the substrate followed by annealing above T_c ($\sim 450^\circ\text{C}$) relieves the in-plane tensile stress of the film, resulting in an increase in d -spacing, as shown in **Figure 3-4**. The largest increase in both d_{200} and d_{002} occurs for the 0.27 μm film (0.76% and 1.32% increase, respectively). Upon release, the d_{200} and d_{002} converge to $\sim 1.966 \pm 0.001$ Å and $\sim 2.015 \pm 0.01$ Å, respectively, for all film thicknesses in the virgin state. The annealing temperature is too low to expect significant changes in Pb stoichiometry, so the change in d spacing is attributed to strain relaxation associated with the different mechanical boundary conditions once the film is globally released. These results confirm

that 0.27 μm film experiences a greater strain relaxation upon release and is likely linked to a larger increase in the irreversible Rayleigh response upon release.[83]

At applied electric fields of $3*E_c$, the electric field induced increase in FWHM of 200 is enhanced post-release by $\sim 9\%$ for the 0.27 μm thick film, also shown in **Figure 3-7** (b). Differences in the FWHM as a function of release state develop after globally releasing the film from the substrate (applied electric fields $\geq 1.5*E_c$ for which tearing of the diaphragms occurs). Therefore, the increase in the FWHM upon release may be due to electric field induced non-uniformities in microstrain and/or crystallite size.

3.3.3 Rayleigh poling study

Previous studies have shown that Rayleigh parameters α_ε and $\varepsilon_{initial}$ have a complicated thickness dependence that is influenced by the domain state of the film and changes upon release.[83] Complementary Rayleigh analysis was conducted to investigate whether the thickness dependence of α_ε and $\varepsilon_{initial}$ changes upon poling. Dispersion curves of the Rayleigh parameter α_ε as a function of frequency are shown in **Figure 3-10** for unpoled (a) and poled (b) PZT films in the clamped state. In general, α_ε decreases upon poling, presumably due to the decrease in domain wall density associated with the coarsening of c -domains inferred from the smaller FWHM of the 002 reflection. Small ($< 9\%$) thickness independent changes in α_ε occur upon poling for clamped films.

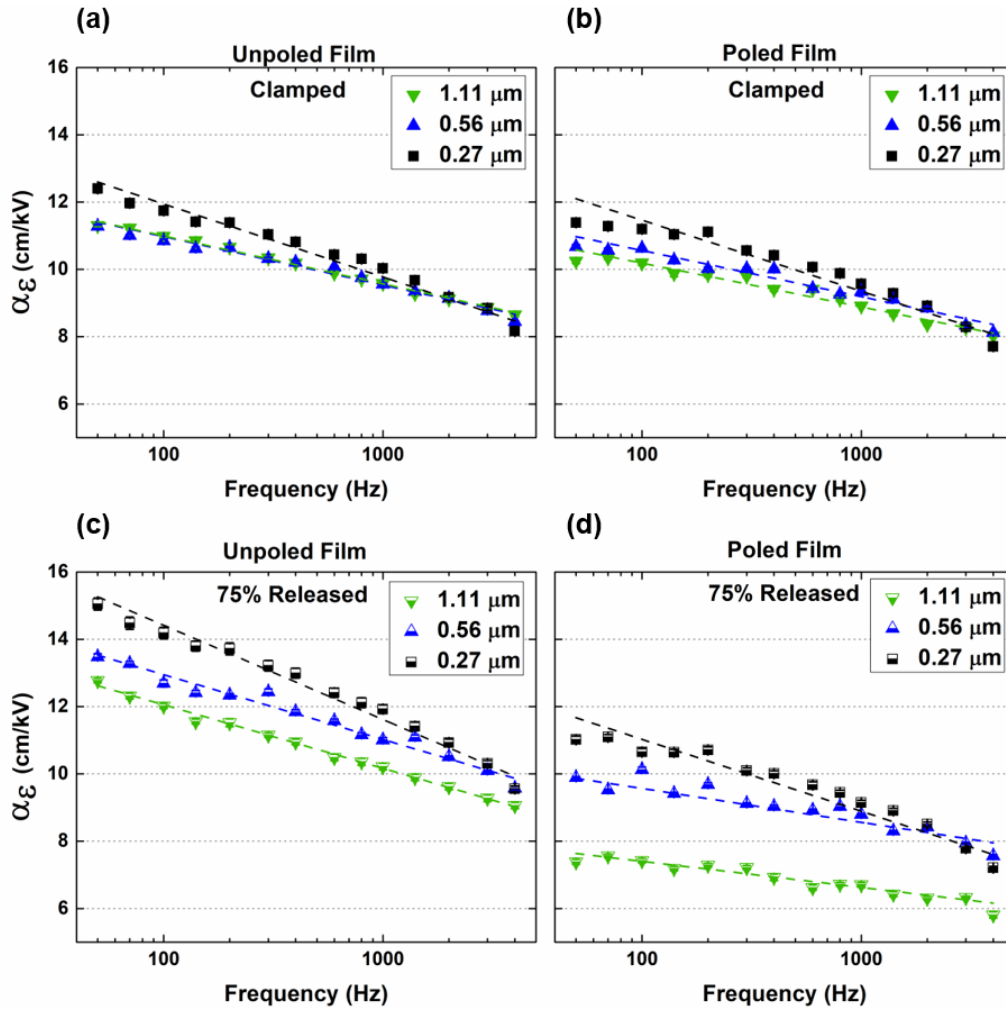


Figure 3-10: Frequency dispersion of the Rayleigh parameter α_ϵ as a function of film thickness ranging from 0.27 μm to 1.11 μm for 2% Nb-doped PZT 30/70 thin films in the clamped state for unpoled (a) and poled (b) films, as well as in the 75% released state for unpoled (c) and poled (d) films.

Upon 75% release from the substrate, α_ϵ increases for all film thickness, as shown in **Figure 3-10** (c). Moreover, after poling, the change in α_ϵ for the 75% released film is more than double that for the clamped film. The changes in α_ϵ are the largest at low frequencies, confirming observations reported elsewhere that substrate clamping has a greater influence on slower, irreversibly moving, domain walls.[83] Finally, since releasing the film from the substrate enhances ferroelastic domain reorientation, it can be assumed

that the greater change in α_ϵ for released films is due to a greater decrease in domain wall density resulting from c -domain coarsening upon poling.

Dispersion curves of $\epsilon_{initial}$ are shown in **Figure 3-11** for unpoled (a) and poled (b) clamped PZT films. $\epsilon_{initial}$ decreases upon poling due to the increases in volume fraction of c -domains coupled with a decrease in domain wall density due to coarsening of the c -domains. The thickness dependence of $\epsilon_{initial}$ is increases after poling, with a three times larger change in $\epsilon_{initial}$ for the 1.11 μm film ($\sim 16\%$) compared to the 0.27 μm film ($\sim 5\%$). This thickness-dependent change in $\epsilon_{initial}$ is not due to differences in the ferroelastic domain reorientation, since η_{002} is not thickness-dependent (see in **Figure 3-2**). Additionally, the thickness-dependent change in $\epsilon_{initial}$ is not intrinsically driven since there is no change in the thickness dependence of ν_{002} .

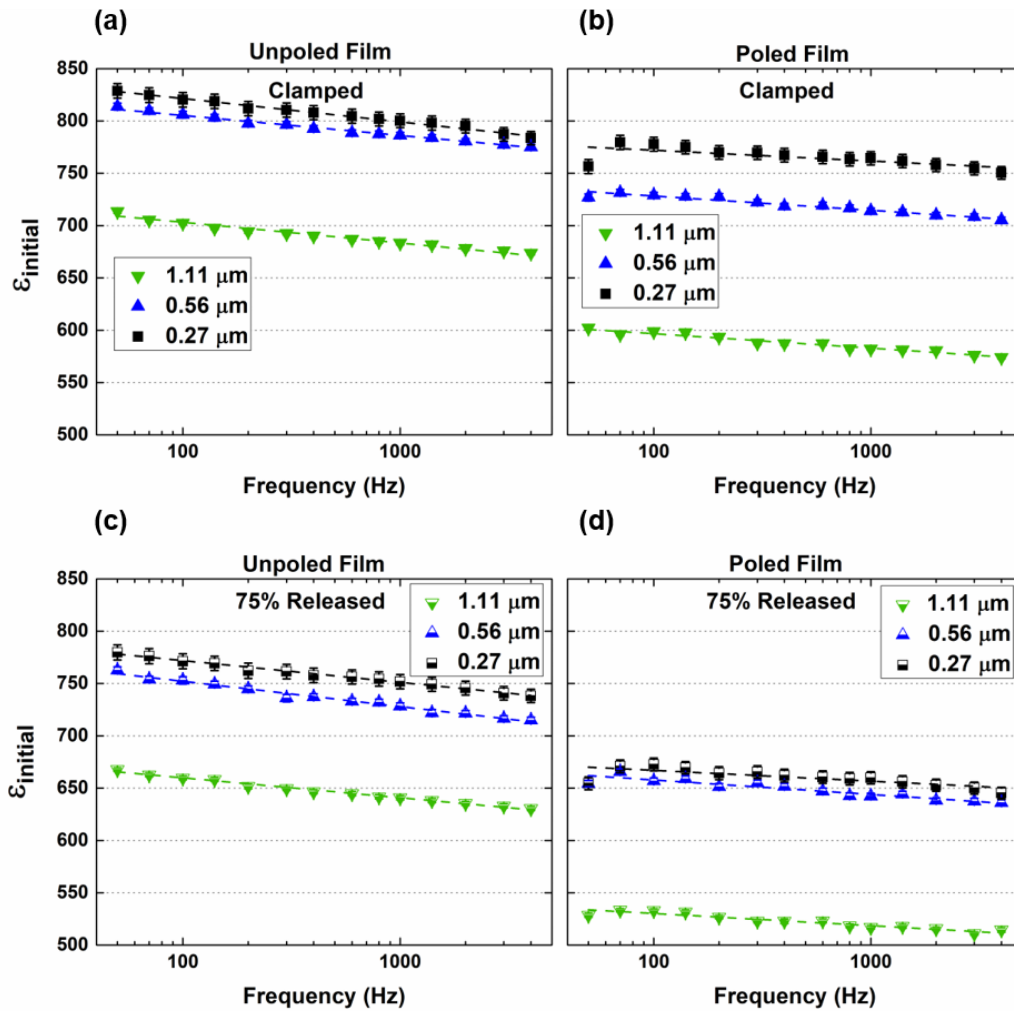


Figure 3-11: Frequency dispersion of the Rayleigh parameter $\epsilon_{\text{initial}}$ as a function of film thickness ranging from 0.27 μm to 1.11 μm for 2% Nb-doped PZT 30/70 thin films in the clamped state for unpoled (a) and poled (b) films, as well as in the 75% released state for unpoled (c) and poled (d) films.

Phenomenology can be used to determine whether thickness-dependent changes in $\epsilon_{\text{initial}}$ upon release and after poling is driven by intrinsic or reversible extrinsic contributions to the permittivity. Estimated values for $\epsilon_{r,\text{intrinsic}}$ are plotted as a function of film thickness for unpoled films in both the clamped and 75% released states, as shown in the lower portion of **Figure 3-12** (a). For a clamped unpoled film, $\epsilon_{r,\text{intrinsic}}$ decreases as thickness increases, as expected based on the thickness-dependence of ν_{002} . However,

upon 75% release from the substrate, the thickness dependence in $\epsilon_{r,intrinsic}$ is reduced. Therefore, the thickness dependence in $\epsilon_{initial}$ for the unpoled, 75% released state is due predominantly to a thickness dependence in the reversible extrinsic contribution to the relative permittivity ($\epsilon_{r,extrinsic}^{reversible}$). Upon release, $\epsilon_{initial}$ decreases by ~6% for all film thicknesses, as shown in **Figure 3-11** (c), which is mainly related to a shift from reversible to irreversible domain wall contributions to the relative permittivity.[83] Phenomenological calculations suggest that the $\epsilon_{r,extrinsic}^{reversible}$ decreases upon release for all film thicknesses, driving the overall decrease in $\epsilon_{initial}$.

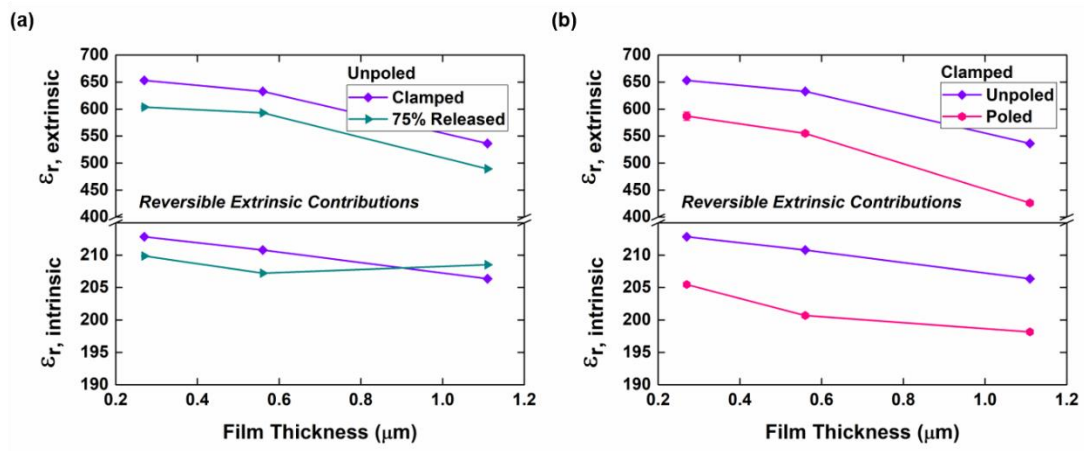


Figure 3-12: The intrinsic ($\epsilon_{r,intrinsic}$) and reversible, extrinsic ($\epsilon_{r,extrinsic}$) contributions to the permittivity as a function of film thickness ranging from 0.27 μm to 1.11 μm for 2% Nb-doped PZT 30/70 thin films in the clamped and 75% released state for unpoled (a), as well as in the clamped state for unpoled and poled films (b).

For clamped films, $\epsilon_{r,intrinsic}$ decreases upon poling, with a comparable decrease for all film thicknesses (3.4% decrease for 0.27 μm vs. 4.0% decrease for 1.11 μm), as shown in the lower portion of **Figure 3-12** (b). Therefore, it is confirmed that the thickness-dependent change in $\epsilon_{initial}$ upon poling for a clamped film is not due to intrinsic changes.

In general, $\epsilon_{r,extrinsic}^{reversible}$ decreases as thickness increases regardless of the release state for

both unpoled and poled samples, as shown in the upper portion of **Figure 3-12** (a) and (b). These results suggest that substrate clamping creates deep potential wells in the potential energy landscape in which reversible motion of domain walls is preferred, consistent with studies by Griggio *et al.*[54] Additionally, it is probable that domain wall motion in thinner films exhibit more reversible motion compared to thicker films, since a greater fraction of domain walls in thinner films are subject to clamping effects at the film-substrate interface. For clamped films, the decrease in $\epsilon_{r,extrinsic}^{reversible}$ upon poling in the thicker 1.11 μm film is double that for the thinner 0.27 μm film (20% decrease vs. 10% decrease, respectively). Therefore, the thickness-dependent change in $\epsilon_{initial}$ upon poling for a clamped film is primarily due to extrinsic contributions. It is proposed that thicker films, which have reduced in-plane tensile stress and defect concentrations, experience a greater coarsening of *c*-domains upon poling. As a result, thicker films have smaller domain wall densities in the poled state, resulting in a greater decrease in both $\epsilon_{r,extrinsic}^{reversible}$ and $\epsilon_{initial}$ upon poling.

The relative permittivity can be separated into three contributions: intrinsic, reversible extrinsic and irreversible extrinsic contributions, as shown in **Figure 3-13**. It was found that for these films, $\epsilon_{r,extrinsic}^{reversible}$ makes up a majority of the relative permittivity (at least 70%). Therefore, the thickness dependence in $\epsilon_{r,extrinsic}^{reversible}$ will dictate the thickness dependence of the overall relative permittivity. As noted above, the extraction of the three contributions to the relative permittivity assumes that the contributions can be stacked linearly. However, the intrinsic and extrinsic contributions may be inter-related. In this case, we assume that the cross terms are negligible at low applied electric fields (within the Rayleigh regime: $E_{applied} \leq E_c$). It is also possible that properly accounting for clamping

of the intrinsic relative permittivity would drop that contribution by roughly a factor of two, with the difference contributing to the reversible extrinsic permittivity.

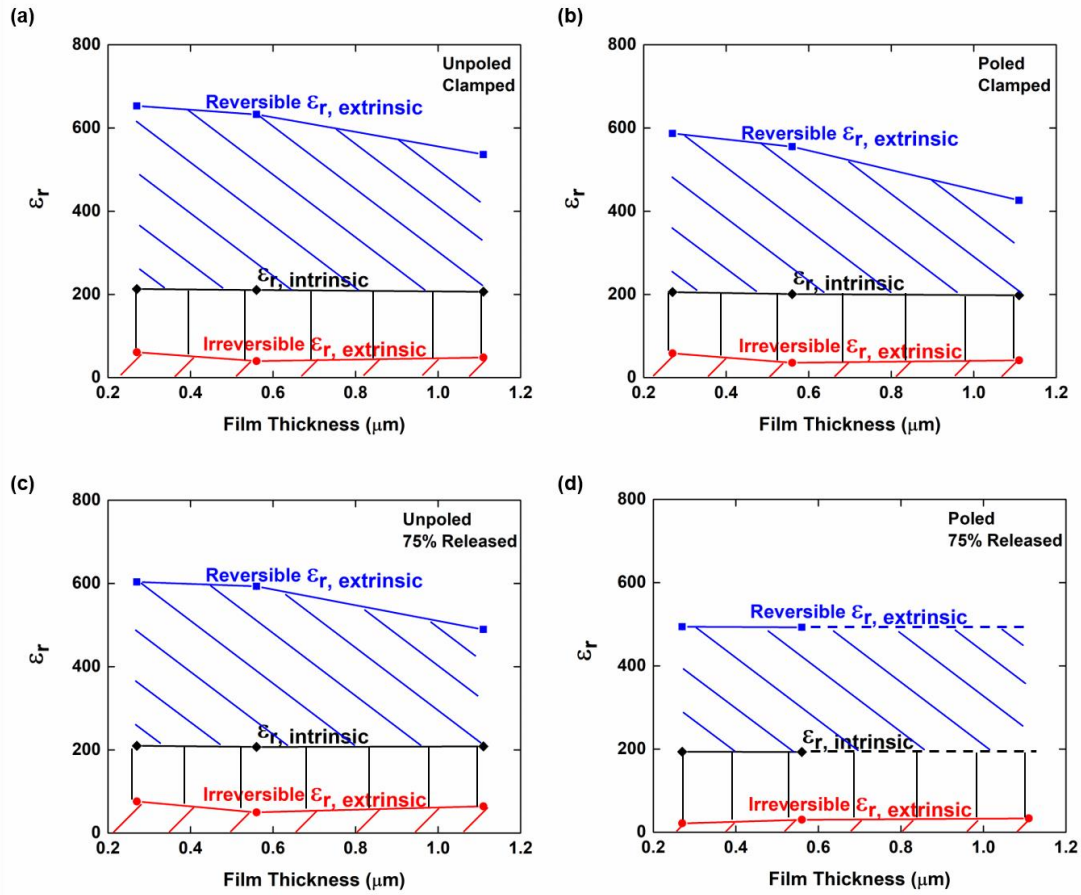


Figure 3-13: The intrinsic ($\epsilon_{r,\text{intrinsic}}$), reversible and irreversible extrinsic ($\epsilon_{r,\text{extrinsic}}$) contributions to the permittivity as a function of film thickness ranging from 0.27 μm to 1.11 μm for 2% Nb-doped PZT 30/70 thin films in the clamped state for unpoled (a) and poled films (b), as well as in the 75% released state for unpoled (c) and poled films (d).

3.4 Conclusions

In situ high resolution XRD was used to investigate the influence that substrate clamping and residual stress have on the thickness dependence of the volume fraction of *c*-domains and electric field induced strain upon release. Tetragonal {001} $\text{Pb}_{0.99}(\text{Zr}_{0.3}\text{Ti}_{0.7})_{0.98}\text{Nb}_{0.02}\text{O}_3$ films were deposited using CSD with thicknesses ranging from

0.27 μm to 1.11 μm . The thickness dependence of ν_{002} is influenced by the concentration of defects in the films and the degree of residual stress formed upon cooling below T_c . This thickness dependence persists after poling and is alleviated upon release. The thickness dependence of ν_{002} can result in differences in the intrinsic contributions to reversible Rayleigh parameter, $\varepsilon_{initial}$. The thinnest 0.27 μm film has the smallest d -spacings for both a and c -domains due to a greater in-plane tensile stress and a higher concentration of defects present in thinner films. In general, the electric field produced changes in d_{002} and d_{200} associated with irreversible coarsening of c -domains as well as irreversible 90° domain reorientation, both of which will change the local stress state of the film. The thickness dependence of the FWHM of 002 is due to increasing microstrain and crystallite size with film thickness. Releasing the film from the substrate relieves residual stress, increases the FWHM of the 200 reflection and enhances ferroelastic domain reorientation. Residual stress in a film indirectly affects the extent of reversible, extrinsic contributions to the relative permittivity. These results confirm that residual stress at the film-substrate interface creates a potential energy landscape with deep potential wells, such that reversible motion of domain walls is preferred.

Chapter: 4 Influence of Elastic Layer Thickness on Mechanical and Ferroelastic Behavior of PiezoMEMS Beams

4.1 Introduction

Pb(Zr_xTi_{1-x})O₃ (PZT) thin films serve as the active layer in piezoelectric microelectromechanical systems (piezoMEMS) for applications such as mass sensors, radio frequency (RF) switches, transformers, micromachined ultrasound transducers, and small-scale robotic actuators.[3][4][5][6][7][8][9][10][11][12] For these applications, released structures, such as a cantilever or fixed-fixed beam geometry, enhance the out-of-plane deflection for actuators and in-plane stresses for sensors. A typical piezoMEMS structure consists of a Pt/PZT/Pt/TiO₂/SiO₂ stack grown on a Si substrate, although many options for the electrodes (Pt, IrO₂, etc.) and the passive elastic layer (here SiO₂) are possible. The elastic layer thickness and its stress state can be tailored to control the static deformation of the piezoelectric layer, rigidity, resonant frequency and the drive voltage required to reach a particular deflection.[3][4][99][100][101]

The residual stress of each layer (σ_i) can be approximated as an uniaxial residual stress field using the polynomial in Equation 4-1 where h is the thickness of the individual layer and z is the z -position across the layer thickness from the film's midplane.[102]

$$\sigma_i = \sum_{k=0}^{\infty} \sigma_k * \left(\frac{2z}{h}\right)^k \text{ where } z \in \left(\frac{-h}{2}, \frac{+h}{2}\right) \quad 4-1$$

Therefore, for the first order approximation, the first term (σ_0) represents the mean stress of the layer, and the second term $\left(\sigma_1 * \left(\frac{2z}{h}\right)\right)$ represents the linear stress gradient in the film resulting from growth stresses. For a multilayered system, the mean residual stress

can be represented by the integrated stress, the residual stresses (σ_i) multiplied by the thickness (t_i) of each layer, as shown in Equation 4-2.[103]

$$\sigma_{1,2,\dots,n} = \frac{\sum_i^n \sigma_i t_i}{\sum_i^n t_i} \quad 4-2$$

The residual stress that develops during processing includes both thermal and growth stresses. Thermal stress develops due to the mismatch in the coefficient of thermal expansion (α_{CTE}) between the film and the substrate. Typically, on a blanket Si substrate, a crystallized PZT layer is under biaxial, in-plane tension since α_{CTE} of Si (2.6 ppm/°C) is less than that of PZT in the paraelectric phase (6.7-9.4 ppm/°C, depending on composition).[75] Additionally, the thermal SiO₂ layer is under compression, both due to intrinsic growth stresses and since α_{CTE} of Si is greater than that of SiO₂ (0.5 ppm/°C).[104]

Intrinsic stresses can vary during layer-by-layer processing involving repetitive high temperature annealing steps, such as during chemical solution deposition (CSD).[30][81][82] In particular, either line defects or non-stoichiometric defects vary in concentration across a film thickness, resulting in an out-of-plane stress gradient as a function of film depth. For example, during CSD of PZT thin films, Pb loss to the film-substrate interface and Zr/Ti segregation are common occurrences.[71][105][106] Therefore, intrinsic stress as well as thermal stress may be present in the PZT, contributing to the overall residual stress in the PiezoMEMS device stack (σ_{stack}).

In order to relieve σ_{stack} , a cantilever changes length in response to the mean stress and bends to relieve stress gradients.[102] The overall deflection can be modeled using Stoney's equation for cantilevers that have aspect ratios $\frac{L}{b} \geq 3$, where L is the length of the

cantilever and b is the width of the cantilever.[107] Additionally, finite element analysis (FEA), Bernoulli-Euler beam bending and other analytical methods have been proposed to describe the deflection of cantilevers and fixed-fixed beams. [99][107][108][109][110][111]

The passive layer (typically SiO_2) in PiezoMEMS is used to amplify deflection, while providing desired levels of stiffness to control resonance frequencies. The differences in the residual stress states between the tensile PZT layer and the compressive SiO_2 layer amplifies the static deflection of a cantilever tip since the layers are typically located on opposite sides of the neutral axis (\bar{y}).[99][110][112] The neutral axis can be calculated using Equation 4-3, in which t_i is the thickness, E_i is the Young's modulus of a given layer, E_{PZT} is the Young's modulus of PZT and y_i is the centroid of a given layer.

$$\bar{y} = \frac{\sum \left[t_i * \left(\frac{E_i}{E_{PZT}} \right) * y_i \right]}{\sum \left[t_i * \left(\frac{E_i}{E_{PZT}} \right) \right]} \quad 4-3$$

The added thickness of the SiO_2 layer increases the flexural rigidity (D) and bending stiffness (S) of the device, as shown in Equation 4-4, where E is the Young's modulus, t is the overall thickness and ν is the Poisson's ratio of the device.[113]

$$D = \frac{E * t^3}{12 * (1 - \nu^2)} = \frac{S}{(1 - \nu^2)} \quad 4-4$$

D and t are important design parameters for tuning the fundamental resonance frequency (f_0) for many PiezoMEMS devices, as shown in Equation 4-5, where ρ is the density. γ is a constant related to the length (L) of the structure and scaled frequency parameter or eigenvalue (k), as shown in Equation 4-6.[114]

$$f_0 = \gamma^2 \sqrt{\frac{D}{\rho * t}} \quad 4-5$$

$$\gamma = \frac{\sqrt{t * k}}{L} \quad 4-6$$

The normalized beam rigidity depends on the thickness of structures.[110][111][115][116] If $E_{SiO_2} > E_{PZT}$ then the average E_{stack} increases, which will increase D and S. However, it is difficult to determine whether SiO₂ or PZT has the larger Young's modulus since the reported values for E_{SiO_2} vary from 60 GPa to 80 GPa [117][118] and E_{PZT} varies from 40 GPa to 100 GPa with texture, composition, doping, etc.[119]

In the case of a fixed-fixed beam geometry, more complicated buckling patterns can occur in thinner devices. As the thickness of the SiO₂ layer decreases, f_0 is expected to decrease. However, f_0 will increase as the buckling complexity increases.[120] Therefore, for a fixed-fixed beam geometry, there may be competing mechanisms, flexural rigidity vs. buckling mode shape, that dictate the shift in resonance frequency as the thickness of the SiO₂ layer is varied.

As the rigidity of the device increases, at some point the ferroelastic response of the PZT layer will be suppressed, in the same way that substrate rigidity suppresses the ferroelastic response in blanket films.[51][86] The influence of substrate clamping on the dielectric properties of PZT can be investigated using Rayleigh analysis.[54][83] Therefore, this technique can be utilized to determine how the dielectric properties of the PZT layer change as the rigidity of the device increases, i.e. the thickness of the SiO₂ layer increases. The Rayleigh law is described using Equation 1-8 in Chapter 1 of this thesis. In

short, $\epsilon_{initial}$, is the reversible dielectric Rayleigh coefficient which contains both the reversible extrinsic and intrinsic contributions to the permittivity. α_ϵ , is the irreversible dielectric Rayleigh coefficient associated with extrinsic contributions to the permittivity from irreversible movement of domain walls and phase boundaries through a random potential energy landscape.[21]

Griggio *et al.* has shown that polycrystalline $\text{Pb}(\text{Zr}_{0.52}\text{Ti}_{0.48})\text{O}_3$ (PZT 52/48) films that are released from the substrate have enhanced α_ϵ and $\epsilon_{initial}$. [54] Conversely, Denis *et al.* reported that α_ϵ increases, while $\epsilon_{initial}$ decreases, with increasing release state for {001} textured PZT 30/70 films of thickness ranging from 0.27 μm to 1.11 μm . It is suggested that there is a shift of at least some domain walls from reversible to irreversible motion upon release.[83] Therefore, it is important to understand how the elastic layer thickness (i.e. device rigidity) influences the irreversible or reversible contributions to the relative permittivity of the PZT layer. This will ultimately govern device performance.

4.2 Fabrication

Tetragonal, {001} textured $\text{Pb}(\text{Zr}_{0.3}\text{Ti}_{0.70})\text{O}_3$ (PZT 30/70) based PiezoMEMS actuators were fabricated on a (001) silicon wafer in a cantilever and fixed-fixed beam geometry. The free-standing composite stack is comprised of either a 0.76 μm or 2.035 μm thick SiO_2 elastic layer, followed by a TiO_2 adhesion layer, a Pt bottom electrode, a PbTiO_3 seed layer, a PZT 30/70 active layer, and an IrO_2 top electrode layer. A schematic of the device stack, including the thicknesses of each layer and lateral dimensions, is shown in **Figure 4-1** for the fixed-fixed beam geometry (a, b) and the cantilever geometry (c, d). SEM images of the side view of both devices are also included.

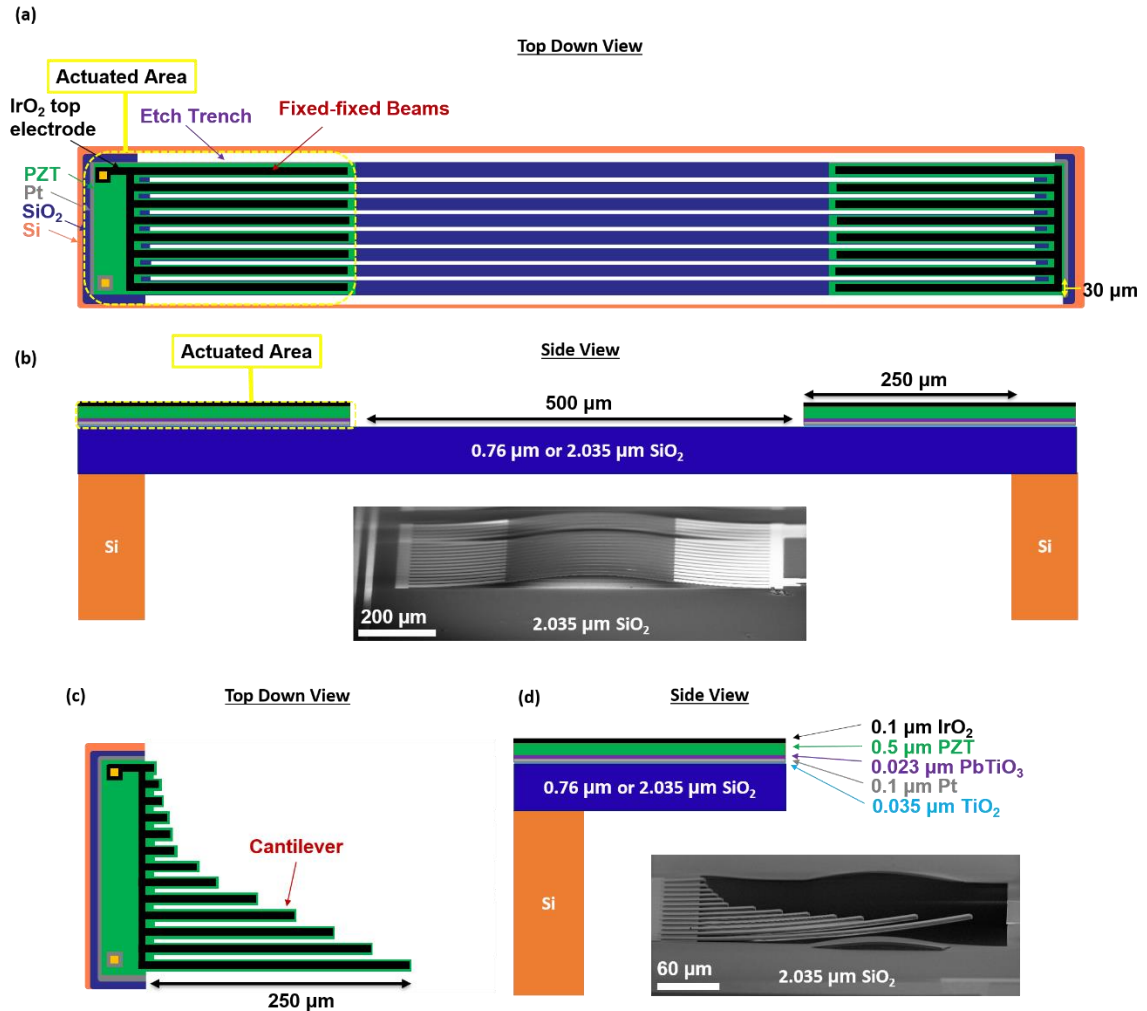


Figure 4-1: A schematic illustrating the dimensions and film stack of the fixed-fixed beams, including a top down view of the patterned features (a) and side view of the device stack (b) with a SEM image of the device with a 2.035 μm SiO₂ elastic layer. Also shown is a schematic listing of the dimensions and film stack for cantilevers of lengths ranging from 250 μm to 50 μm, including a top down view of the patterned features (c) and side view of the device stack (d) with a SEM image of cantilevers with a 2.035 μm SiO₂ elastic layer.

The devices were fabricated at the US Army Research Laboratory (ARL). Full details of the processing are described elsewhere.[99][121] In summary, thermal SiO₂ was grown by annealing a Si wafer at 700 °C. The thickness of the SiO₂ layer was chosen such that either a positive or negative tip displacement of the cantilever was achieved based on a linear residual stress deformation model (2.035 μm or 0.76 μm thick SiO₂, respectively).[99] Next, a layer of Ti was sputtered and oxidized at 750 °C in flowing

oxygen to form the adhesion/diffusion barrier layer. The Pt bottom electrode was deposited onto the adhesion layer at 500 °C using magnetron sputtering. A PbTiO₃ seed layer was deposited via a 2-Methoxyethanol (2-MOE) based CSD process described elsewhere.[58][122] The seed layer promoted the growth of the {001} textured PZT film; the PZT films were also grown via 2-MOE based CSD with 12% excess lead. The PZT films were spun, pyrolyzed and crystallized at 700 °C repeatedly until a ~0.5 μm thick film was achieved. Details of the CSD process used for the PZT film is described elsewhere.[121] Finally, IrO₂ was sputtered onto the PZT layer to act as the top electrode, instead of Pt, to improve capacitor reliability.[123]

The cantilever and fixed-fixed beam geometries were achieved via a four-mask photopatterning and release process described elsewhere.[99][121] Argon ion milling was used to remove regions of the IrO₂/PZT/PbTiO₃/Pt/TiO₂/SiO₂ stack to expose the underlying silicon substrate and create the release trench. An isotropic XeF₂ etch was then used to remove parts of the Si substrate underneath the device stack, creating the free-standing structures. For the cantilever actuator, the IrO₂/PZT/PbTiO₃/Pt/TiO₂/SiO₂ stack extends the full length of the cantilever beam. However, for the fixed-fixed beam structure, the IrO₂/PZT/PbTiO₃/Pt/TiO₂/SiO₂ stack is only present 250 μm along the length of the beam from the clamped edges on either side of the bridge structure, as shown in the cross-sectional schematic of **Figure 4-1** (a). Only SiO₂ is present at the center of the bridge structure; this is shown in navy blue in **Figure 4-1** (a) (500 μm in length).

4.3 Modeling

FEA (via COMSOL Multiphysics® software[124]) was used to model the vertical deflection of a 2-dimensional (2-D) cantilever 250 μm in length, 30 μm in width using the material properties listed in **Table 4-1**. All layers were assumed to behave as linear elastic materials with isotropic properties. Since PbTiO_3 shares similar material properties to PZT and the thickness of the PbTiO_3 is an order of magnitude less than that of PZT, the PbTiO_3 layer was included as part of the PZT layer in the modeling for simplicity. Since E_{PZT} can vary with composition, dopant type and texture, E_{PZT} values ranging from 40 GPa to 100 GPa were tested in the simulation, which is representative of the range of E_{PZT} found in the literature.[119]

Material	Thickness (μm)	Young's Modulus (GPa)	Poisson's Ratio	Initial Stress (MPa)
IrO_2	0.1	262 [123]	0.3 [123]	-900 [125]
PZT	0.5	40 to 100 [119][126]	0.3 [81]	0 to 300
Pt	0.1	182 [127]	0.41 [127]	700 [99]
TiO_2	0.035	250 [128]	0.27 [128]	500 [129]
SiO_2	2.035 or 0.76	60 to 100 [117][126]	0.17 [117]	0 to -125

The residual stress of the PZT and SiO_2 layers were based on thermal stress calculations for a film grown on a 0.5 mm thick Si substrate ($E_{\text{Si}} = 160$ GPa [130], $\nu_{\text{Si}} = 0.17$ [130] and $\alpha_{CTE,\text{Si}} = 2.6$ ppm/ $^\circ\text{C}$ [131][132]) using classical laminate theory.[133] A range of values for σ_{PZT} and σ_{SiO_2} were chosen to account for the variations in α_{CTE} of PZT [134] and SiO_2 [135] reported in the literature. σ_{PZT} was varied between 0 MPa and 300 MPa, corresponding to a $\alpha_{CTE,PZT}$ range of 2 ppm/ $^\circ\text{C}$ to 6 ppm/ $^\circ\text{C}$, respectively, for $E_{PZT} =$

80 GPa. σ_{SiO_2} was varied between 0 GPa and -125 GPa, corresponding to a α_{CTE, SiO_2} range of 2.5 ppm/°C to 0.25 ppm/°C, respectively, for $E_{SiO_2} = 70$ GPa.

4.4 Characterization

The cantilever tip displacements were measured using optical profilometry (Zygo Nexview™ NX2, 3D Optical Surface Profiler), typically in a CSI measurement mode, high Z resolution, high dynamic range, 10x magnification, 1x or 0.5x zoom depending on feature size, and 100 μ m z-scan length to view both the device features and etch pit underneath. The measured tip displacements were used as a reference point for the COMSOL simulations. Based on this reference, the residual stress combinations for PZT and SiO₂ that give the desired tip displacement were identified. The vertical deflections and buckling nature of the fixed-fixed beams were also measured using optical profilometry.

Polarization vs. electric field (P-E) hysteresis loops were measured at a frequency of 10 Hz using a *Radiant Precision Ferroelectric Tester* for cantilever and fixed-fixed beams with SiO₂ layers of thickness 2.035 μ m and 0.76 μ m. Rayleigh analysis was also conducted. The dielectric properties were measured at frequencies ranging from 100 Hz to 4 kHz with applied AC electric fields up to 0.5*E_c (E_c = 55 \pm 5 kV/cm) after the samples were annealed (open circuit) at ~450°C for 30 min. and aged for 24 hours.

4.5 Results and Discussion

4.5.1 Influence of Stress and Thickness on Cantilever Tip Deflection

Optical profilometry measurements for cantilevers of varying lengths are shown in the inset of **Figure 4-2**. For the longest cantilever (i.e. $L=250\ \mu\text{m}$), the tip deflection is positive for cantilevers with a $2.035\ \mu\text{m}$ thick SiO_2 layer and negative for cantilevers with a $0.76\ \mu\text{m}$ thick SiO_2 layer. Sample tilting was accounted for by subtracting the tilt measured from clamped regions of the sample from the overall tip deflection within the area of interest. The magnitude of tip deflection is greater for the $0.76\ \mu\text{m}$ thick SiO_2 device compared to the $2.035\ \mu\text{m}$ thick SiO_2 device ($-26.0\ \mu\text{m}$ and $+18.3\ \mu\text{m}$, respectively, when $L=250\ \mu\text{m}$), as expected based on the lower rigidity. Additionally, as L decreases, the magnitude of the tip deflection also decreases regardless of SiO_2 thickness, as shown in the SEM image of **Figure 4-1** (d).

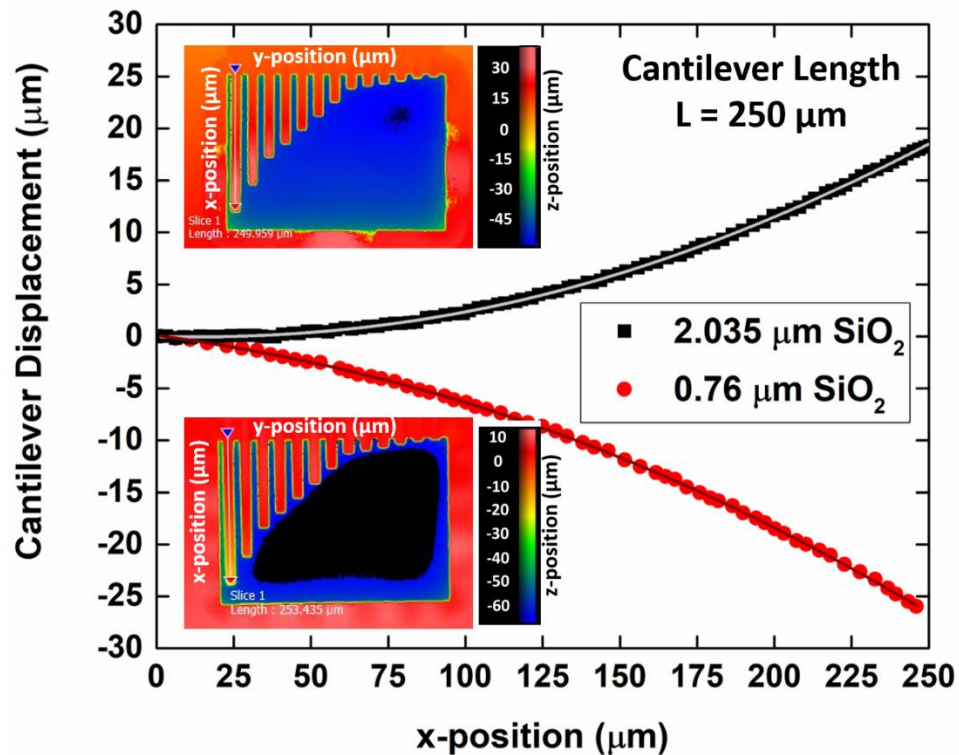


Figure 4-2: Vertical displacement of a cantilever across the length (x-position) of a 250 μm long beam for a device with a 2.035 μm thick SiO_2 elastic layer and a 0.76 μm thick SiO_2 elastic layer. The cantilever displacements were determined using the optical profilometry images inset in the graph for each device.

For a given cantilever length, the differences in the magnitude and sign (\pm) of tip deflection depends on the thickness and residual stress of each layer. The presence of a residual stress gradient in the device stack would result in the bending of the cantilever observed in **Figure 4-2**. [136] In the clamped state, the films were grown on a blanket substrate with a thickness approximately 3 orders of magnitude larger than the film thickness. Therefore, a uniform thermal stress developed within the layers post-processing. However, a stress gradient through the depth of the *released device* exists due to bending since the thermal stress of each layer in the device stack differ, as shown schematically in **Figure 4-3** for a device with a 0.76 μm thick SiO_2 layer and a 2.035 μm thick SiO_2 layer.

Residual Stress Post-processing

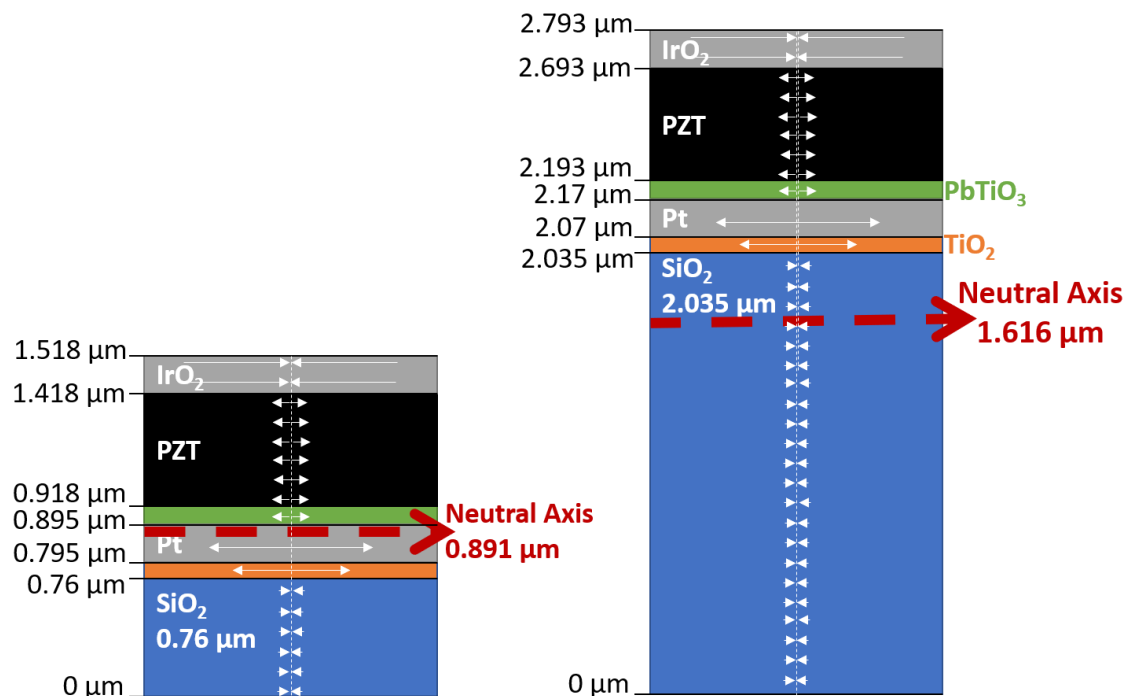


Figure 4-3: A cross-sectional schematic of the thermal residual stress that develops post-processing for a multilayered device, with a 0.76 μm thick SiO_2 layer and a 2.035 μm thick SiO_2 layer, processed on a Si substrate. The z-position of the neutral axis is shown for each device.

Cantilever bending alleviates the residual stresses in the device, more so in layers located farther from the neutral axis. The position of the neutral axis changes as the thickness of the SiO_2 changes, as shown in **Figure 4-3**. Cantilevers with a 0.76 μm thick SiO_2 layer exhibits a negative vertical deflection, suggesting that the region above the neutral axis was under compression and/or the region below the neutral axis was under tension post-processing. For a device with a 0.76 μm thick SiO_2 layer, the neutral axis (Equation 4-3) lies within the Pt bottom electrode. The layers located above the neutral axis in this device include the PbTiO_3 seed layer, the PZT active layer and the IrO_2 top electrode. Since PbTiO_3 and PZT develop in-plane tensile stress when processed on a Si substrate, it is unlikely that the alleviation of the residual thermal stress of these layers will result in the downward cantilever tip bending in this device. The IrO_2 top electrode is under compression post-processing, with a large σ_{IrO_2} of -913 MPa [125], which contributes strongly to the overall deflection of this device. The influence of the residual stress of the IrO_2 top electrode may be greater for the thinner device since the top electrode (0.1 μm) makes up a greater volume of the device stack. If we assume $\sigma_{\text{SiO}_2} = -75$ MPa and $\sigma_{\text{PZT}} = 100$ MPa, the average residual stress above the neutral axis is compressive and $\sim 2\times$ larger in magnitude than that below the neutral axis, (-69 MPa vs. 34 MPa for above and below the neutral axis, respectively, calculated using Equation 4-2). Therefore, upon release, the cantilever deflected in the negative vertical direction, presumably, to alleviate the in-plane stress in the top electrode.

Cantilevers with a 2.035 μm thick SiO_2 layer exhibit a positive vertical deflection, suggesting that the influence of σ_{IrO_2} on the tip deflection decreases as the thickness of the SiO_2 layer increases. For a device with a 2.035 μm thick SiO_2 layer, the neutral axis lies in the SiO_2 layer. As a result, the variation in residual stresses above the neutral axis is greater for this device, since this region includes layers in compression (IrO_2 top electrode and $\sim 0.4 \mu\text{m}$ of SiO_2) and layers in tension (PZT, PbTiO_3 , Pt and TiO_2). If we assume $\sigma_{\text{SiO}_2} = -75 \text{ MPa}$ and $\sigma_{\text{PZT}} = 100 \text{ MPa}$, the average residual stress below the neutral axis is compressive and more than 6x larger in magnitude than that above the neutral axis, (-75 MPa vs. 12 MPa for below and above the neutral axis, respectively, calculated using Equation 2).

4.5.2 FEA Modeling of Cantilever Tip Deflection

Using COMSOL Multiphysics® software, FEA models of the device stack after release were created to determine the residual stress in each layer in order to match the observed tip displacement. **Figure 4-4** shows the mesh used for these simulations. **Figure 4-5** shows a 2-D model of the cantilever tip displacement and a cross-section illustrating the in-plane residual stresses for each layer for cantilevers with either a 2.035 μm thick or 0.76 μm thick SiO_2 layer. Post-deflection, stress gradients form in regions of the device that are far from the neutral axis, as seen in the 2.035 μm thick SiO_2 layer and 0.5 μm PZT layer in the 2.035 μm SiO_2 device. COMSOL was also used to determine which combinations of σ_{PZT} and σ_{SiO_2} produced the experimental tip deflection for both the 2.035 μm and 0.76 μm thick SiO_2 cantilevers. The absolute value of the residual stress ratio of PZT to SiO_2 $\left(\frac{\sigma_{\text{PZT}}}{\sigma_{\text{SiO}_2}}\right)$ decreases as E_{PZT} decreases, regardless of SiO_2 thickness or E_{SiO_2} , as

shown in **Figure 4-6** (a). For a given E_{PZT} , there is a $\sim 4\%$ difference in $\frac{\sigma_{PZT}}{\sigma_{SiO_2}}$ between the 2.035 μm and 0.76 μm thick SiO_2 device if $E_{SiO_2} = 60$ GPa. As E_{SiO_2} increases, the linear relationship (E_{PZT} vs. $\frac{\sigma_{PZT}}{\sigma_{SiO_2}}$) for the 2.035 μm thick SiO_2 device converges with that for the 0.76 μm thick SiO_2 device. As SiO_2 becomes less compliant (greater E_{SiO_2}), a greater residual stress may form in the SiO_2 layer and dictate $\frac{\sigma_{PZT}}{\sigma_{SiO_2}}$ regardless of SiO_2 thickness. However, it is unlikely that $E_{SiO_2} > 70$ GPa.[117][118] Therefore, this suggests that σ_{SiO_2} may be thickness dependent, resulting in differences in $\frac{\sigma_{PZT}}{\sigma_{SiO_2}}$ with SiO_2 thickness. A thickness dependence in σ_{SiO_2} is not uncommon and may be related to variations in processing.[99]

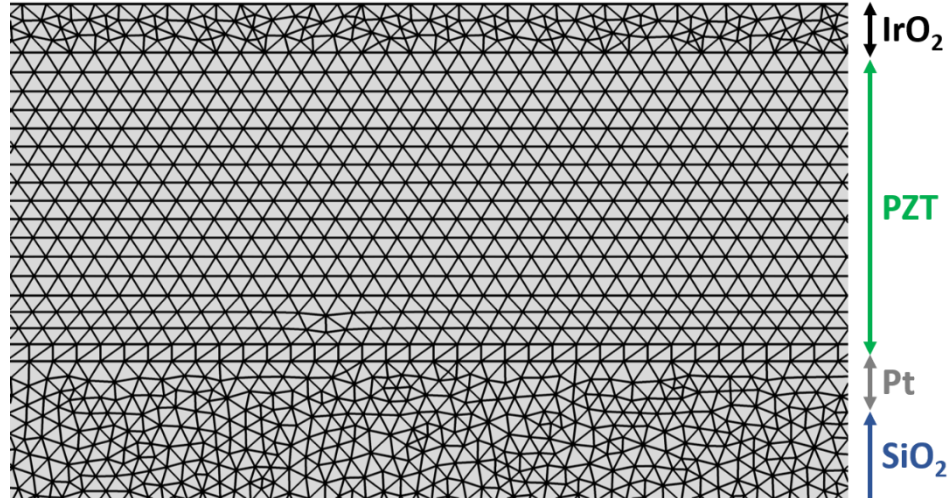


Figure 4-4: The mesh used for FEA simulations of the multilayered PiezoMEMS device.

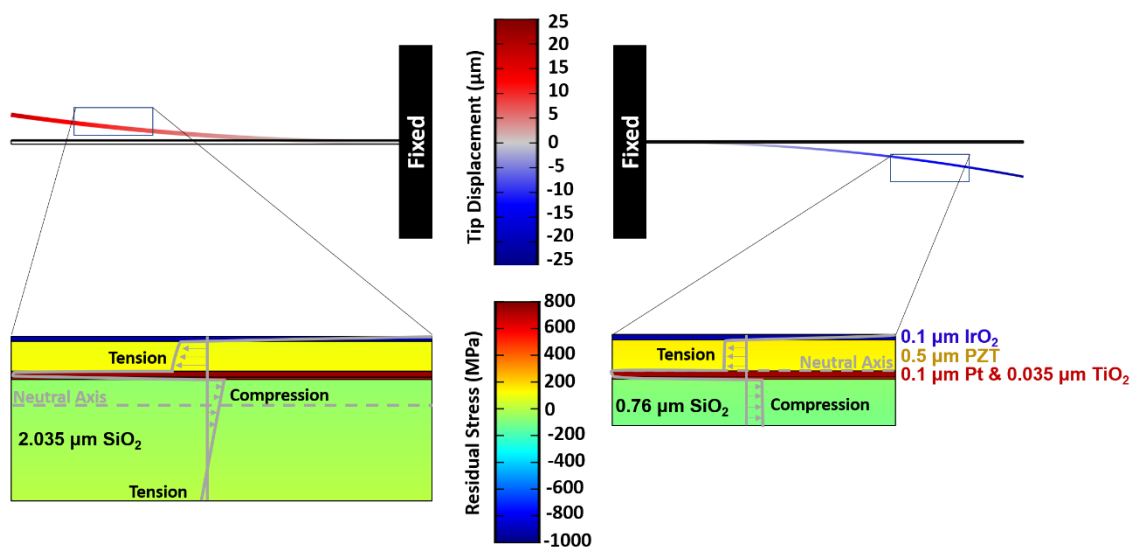


Figure 4-5: A 2-D COMSOL model of the tip deflection of a 250 μm long cantilever, and a schematic cross-section showing the residual stress in each layer after deflection for a device with a 2.035 μm thick SiO₂ elastic layer and a 0.76 μm thick SiO₂ elastic layer.

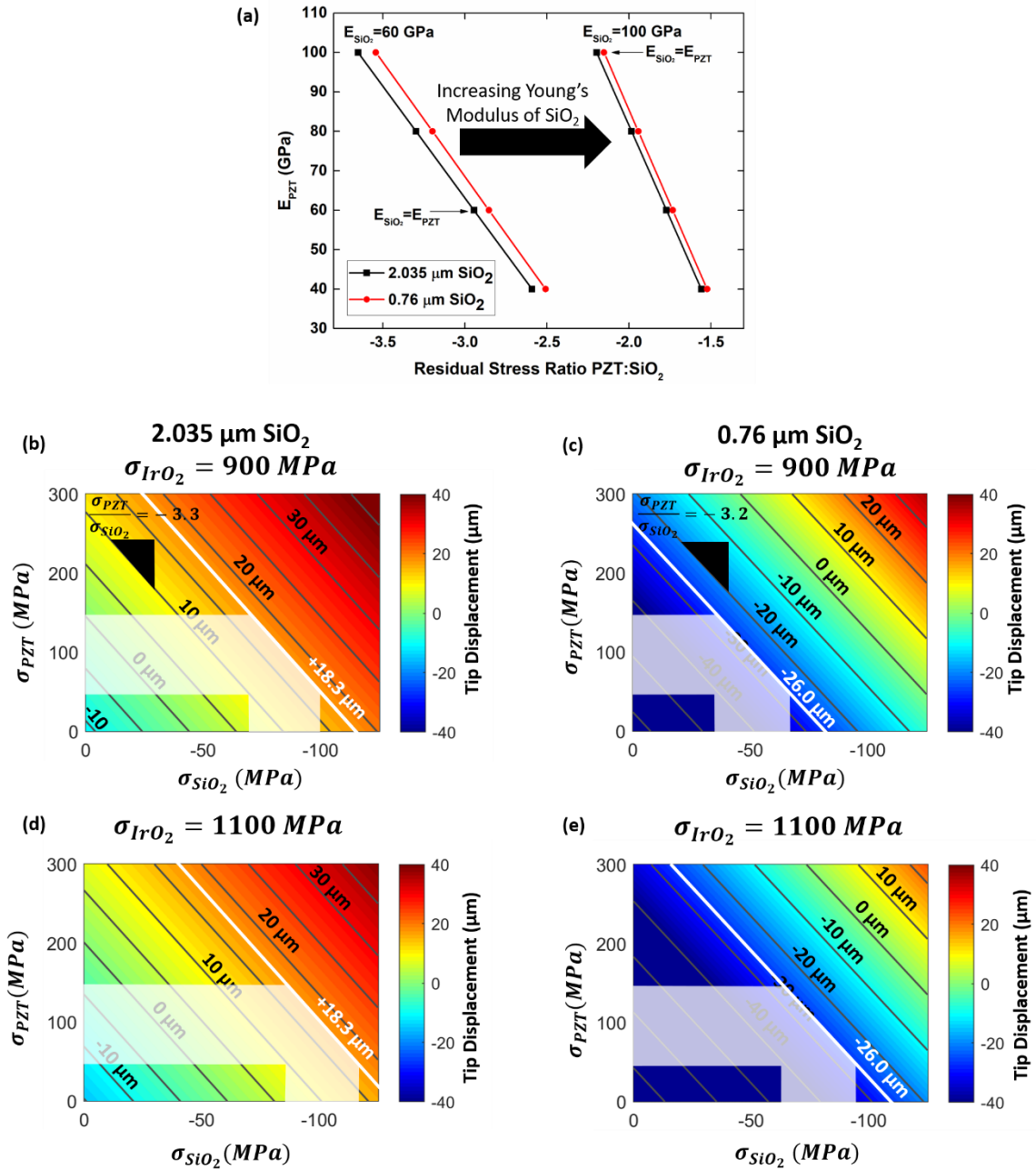


Figure 4-6: (a) The linear relationship between the residual stress ratio ($\sigma_{\text{PZT}}/\sigma_{\text{SiO}_2}$) and the PZT Young's Modulus (E_{PZT}) plotted for a device with a 2.035 μm thick SiO_2 elastic layer and a 0.76 μm thick SiO_2 elastic layer. The comparison is shown for two different SiO_2 Young's Modulus (E_{SiO_2}): 60 GPa and 100 GPa. Contour plots of σ_{PZT} vs. σ_{SiO_2} for a variety of cantilever tip displacements for a device with a 2.035 μm thick SiO_2 elastic layer (b, d) and a 0.76 μm thick SiO_2 elastic layer (c, e) for σ_{IrO_2} for 900 MPa and 1100 MPa.

Contour plots of σ_{PZT} vs. σ_{SiO_2} for a variety of tip displacements is also shown in **Figure 4-6** for the 2.035 μm (b, d) and 0.76 μm (c, e) thick SiO_2 devices with $E_{PZT} = 80$ GPa and $E_{SiO_2} = 60$ GPa. The values of σ_{PZT} and σ_{SiO_2} are not the values of residual stress measured in the PZT and SiO_2 layers of the devices in this study. Rather, the FEA model represents a general (but complex) relationship between the layer thickness, residual stress, elastic modulus and tip displacement of a cantilever device. The grey diagonal lines on the contour plots represent a possible tip displacement (μm) and combinations of σ_{PZT} and σ_{SiO_2} to achieve that displacement. The slope of the line is $\frac{\sigma_{PZT}}{\sigma_{SiO_2}}$. The contour plots can be used to determine the range of σ_{SiO_2} that will produce the appropriate tip displacement if σ_{PZT} ranges from 50 to 150 MPa, as shown in the white shaded regions. The offset of the line (Z_{offset}) corresponds to the tip displacement at zero residual stress of PZT and SiO_2 ($\sigma_{PZT} = \sigma_{SiO_2} = 0$ GPa) and depends on the residual stress of the IrO_2 top electrode (σ_{IrO_2}).

For a given film thickness (2.035 μm SiO_2), the range of σ_{SiO_2} that will produce the appropriate tip displacement varies significantly with σ_{IrO_2} , as shown in **Figure 4-6** for $\sigma_{IrO_2} = -900$ MPa (b) and $\sigma_{IrO_2} = -1100$ MPa (d). Changing the σ_{IrO_2} will shift the origin of the contour plot, thereby shifting the linear relationship between σ_{SiO_2} and σ_{PZT} for the desired tip displacement (white line). To obtain a self-consistent combination of σ_{PZT} and σ_{SiO_2} that will yield the desired tip displacement in each device, the σ_{IrO_2} will be different for the two devices. The σ_{IrO_2} of the 0.67 μm thick SiO_2 device would need to be ~ 200 MPa greater than that for the 2.035 μm thick SiO_2 , as shown in the comparison of the white shaded region in **Figure 4-6** (b) and (e). The relationship between tip displacement

($Z_{tip\ displ.}$), σ_{PZT} and σ_{SiO_2} is shown in Equation 4-7, where m and n are defined by the residual stress ratio: $\frac{\sigma_{PZT}}{\sigma_{SiO_2}} = \frac{m}{n}$. m and n depend on SiO₂ thickness, E_{PZT} and E_{SiO_2} .

$$Z_{tip\ displ.} = m * \sigma_{SiO_2} + n * \sigma_{PZT} + Z_{offset} \quad 4-7$$

4.5.3 Influence of Etch Process on Fixed-Fixed Beam Buckling

Optical profilometry measurements for fixed-fixed beams are shown in the inset of **Figure 4-7** for the device with SiO₂ thickness of 2.035 μm and 0.76 μm . The thicker 2.035 μm SiO₂ device exhibits a first buckling mode shape (n=1) whereas the thinner 0.76 μm SiO₂ device has an asymmetric third buckling mode shape (n=3). A maximum deflection of 34.8 μm occurs at the center of the fixed-fixed beam for the 2.035 μm SiO₂ device. However, the 0.76 μm SiO₂ device has a global maximum deflection of -21.6 μm and local maximum deflection of -16.9 μm , both of which occur ~220 μm from the center of the fixed-fixed beam, which is the region in which the device stack transitions from SiO₂ (present at the center of the fixed-fixed beam) to a stack of IrO₂/PZT/PbTiO₃/Pt/TiO₂/SiO₂ (present at the left and right extremities of the fixed-fixed beams). This region will be referred to as the stack-SiO₂ interface.

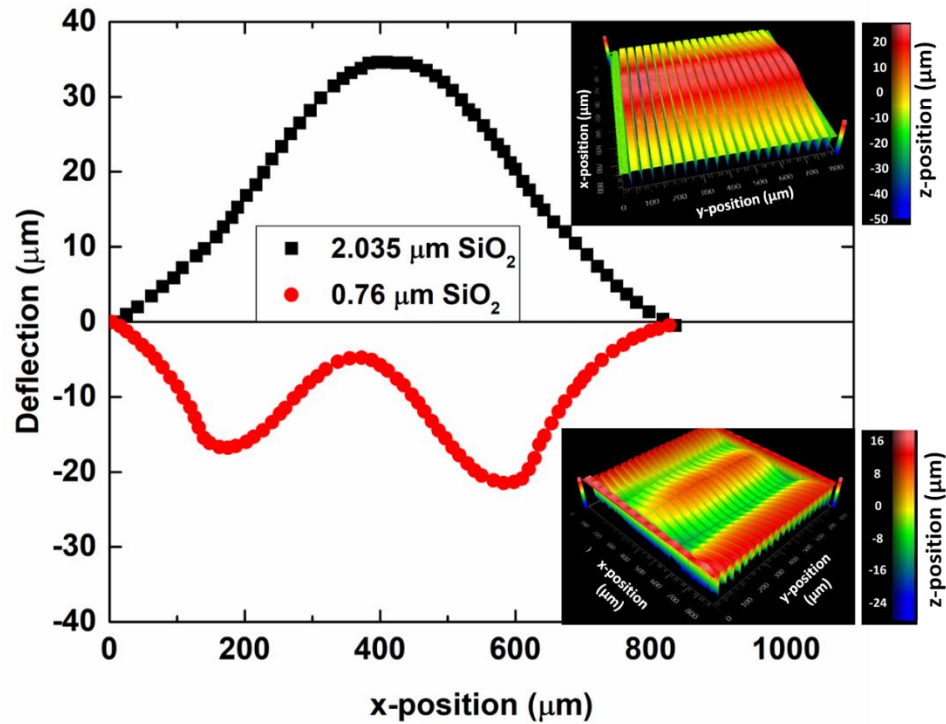


Figure 4-7: The vertical deflection of fixed-fixed beams across the length (x-position) of a ~1,000 μm long beam for a device with a 2.035 μm thick SiO_2 elastic layer and a 0.76 μm thick SiO_2 elastic layer. The buckling and vertical deflection of the fixed-fixed beams were determined using the optical profilometry images inset in the graph for each device.

The driving force to create the complex buckling observed in the fixed-fixed beam with a 0.76 μm thick SiO_2 layer is unclear, but may be an artifact of uneven XeF_2 etching during the release process. The sign of the bending moment (M) around the center of mass at the stack- SiO_2 interface changes for the device with a 0.76 μm thick SiO_2 layer; whereas the sign of M stays the same for the device with a 2.035 μm thick SiO_2 layer, as shown schematically in **Figure 4-8**. For the device with a thicker 2.035 μm SiO_2 layer, the compressive SiO_2 layer dictates the bending across the device. However, for the device with a thinner 0.76 μm SiO_2 layer, the compressive IrO_2 top electrode is proposed to dictate the downward bending in the stack, similar to the bending of the cantilever version of the device. Since the center of the fixed-fixed beam consists only of a compressive SiO_2 layer,

the center of the beam will lengthen to alleviate the residual compressive stress upon release. This can be accomplished by buckling either upward or downward. Therefore, an additional driving force is needed to shift the bending moment at the stack-SiO₂ interface in the device with a thinner 0.76 μm SiO₂ layer. It is proposed that a non-uniform XeF₂ etch may have occurred across the length of the fixed-fixed beam such that undercutting started at the center of the beams, where only SiO₂ was present. Therefore, the central portion of the beam released prematurely and deflected upward to alleviate the compressive stress in the SiO₂. **Figure 4-9** shows an optical profilometry image of an interrupted XeF₂ etch in which regions of SiO₂ (center of the fixed-fixed beams) are released and bend upward although the electroded region of the beam remains unetched and clamped. The device with a thinner 0.76 μm SiO₂ layer achieved a local minimum stress state due to the uneven XeF₂ etch.

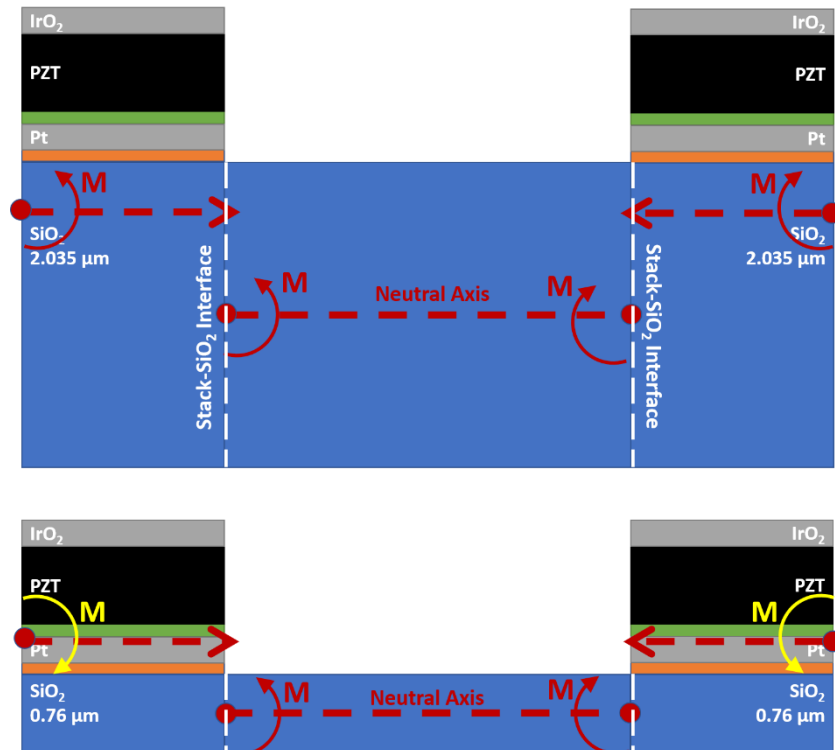


Figure 4-8: A cross-sectional schematic of the neutral axis and bending moment (M) is shown across the length of a fixed-fixed beam with a $0.76 \mu\text{m}$ thick SiO_2 layer and a $2.035 \mu\text{m}$ thick SiO_2 layer.

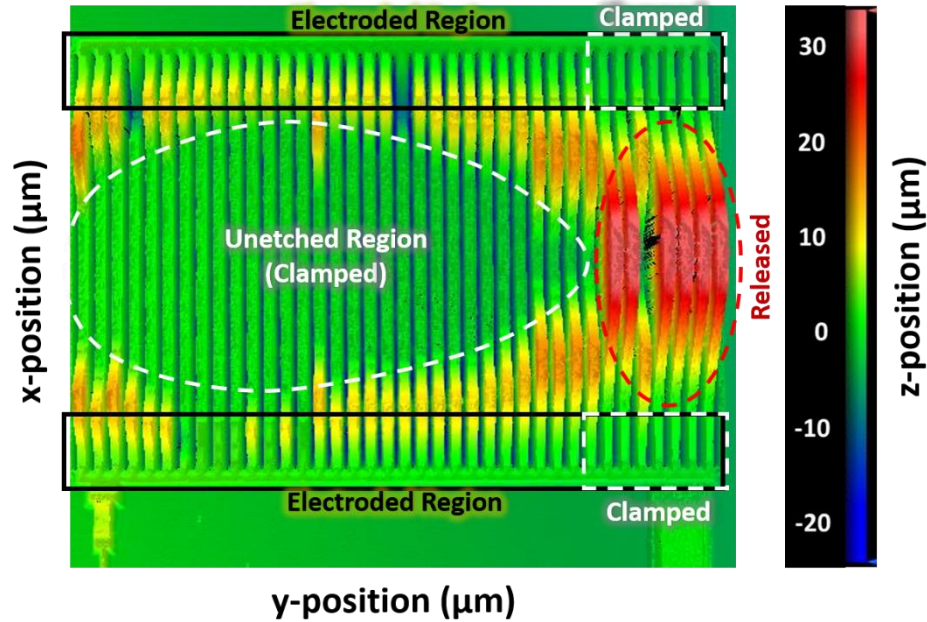


Figure 4-9: Optical profilometry image of a fixed-fixed beam device with a $2.035 \mu\text{m}$ SiO_2 layer that is partially and non-uniformly released after an interrupted XeF_2 etch.

4.5.4 Impact of Nanofabrication and Tip Deflection on Electrical Properties

To understand the impact of device fabrication on the electrical properties of the film, P-E loops were compared for clamped films (a), cantilevers (b), unpoled fixed-fixed beams (c) and poled fixed-fixed beams (d), as shown in **Figure 4-10**. For clamped films, the P-E loop exhibits a square shape, characteristic of a non-linear ferroelectric response. The P-E loops for the $2.035 \mu\text{m}$ and $0.76 \mu\text{m}$ thick SiO_2 devices are almost identical, with imprint towards the positive electric field direction. Therefore, for a clamped film, the remanent polarization ($P_r = 13.5 \pm 0.1 \mu\text{C}/\text{cm}^2$), maximum polarization ($P_{\text{max}} = 36.5 \pm 0.1 \mu\text{C}/\text{cm}^2$) and coercive fields ($+E_c = 68.8 \pm 1.7 \text{ kV}/\text{cm}$ and $-E_c = 53.0 \pm 0.2 \text{ kV}/\text{cm}$) do not depend on the thickness of the SiO_2 layer.

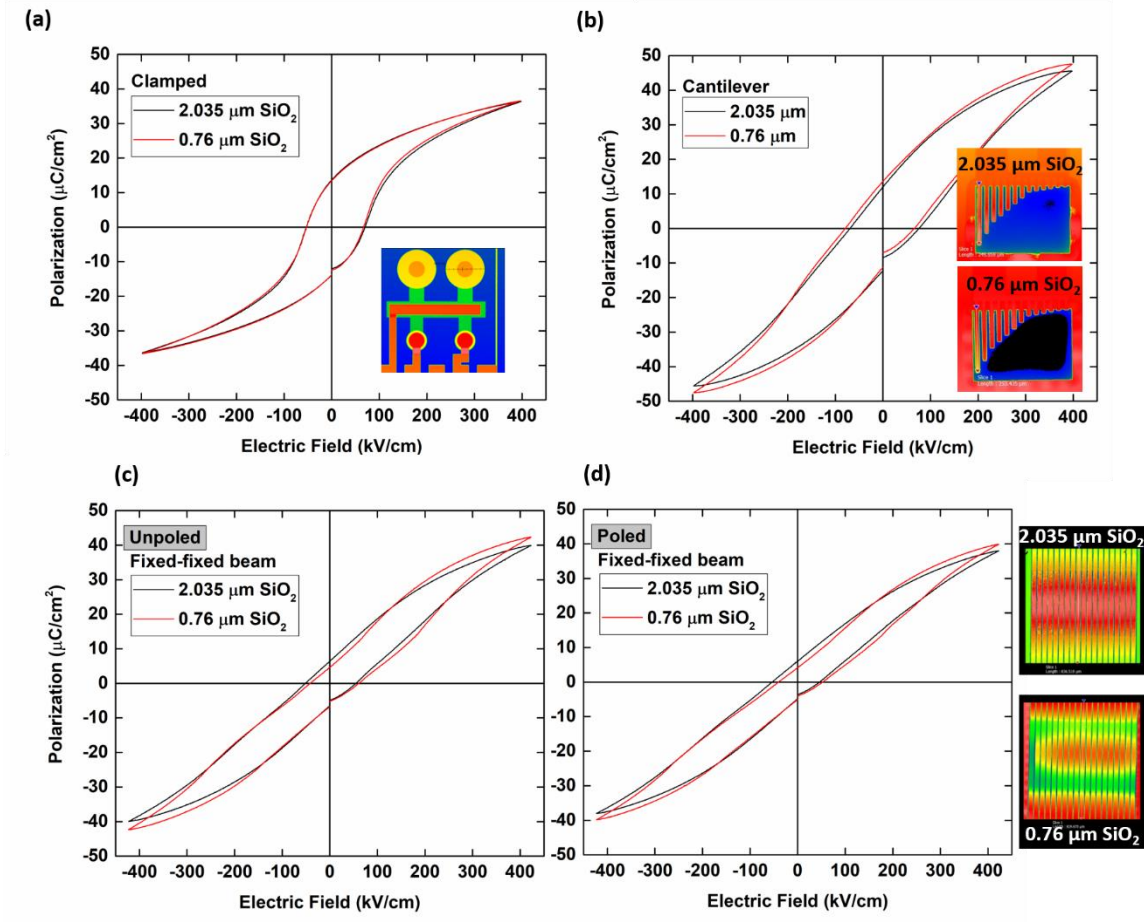


Figure 4-10: Polarization vs. electric field (P-E) hysteresis loops of an unpoled (a) clamped PZT 30/70 thin film, (b) cantilever and (c) fixed-fixed beam for a device with a 2.035 μm thick SiO₂ elastic layer and a 0.76 μm thick SiO₂ elastic layer. P-E loops of a poled fixed-fixed beam for devices with the different SiO₂ elastic layer thicknesses are also shown (d). Complementary optical profilometry images are shown for each device.

Upon release, P_r , P_{max} and E_c increase, as shown in **Figure 4-10** (a) for cantilevers.

In each case, the loops are heavily pinched. Pinching of the P-E loops may be a result of domain wall pinning from structural inhomogeneity and/or defects that develop during additional nanofabrication (such as Ar ion milling, reactive ion etching and XeF₂ etching) needed to create the cantilevers and fixed-fixed beams. In particular, the charged ions in reactive ion etching can produce local imprint of the P-E loops. The cantilever with SiO₂ thickness of 0.76 μm has a higher P_{max} and P_r than that for the thicker elastic layer. It is not

clear if this is due to a lowered rigidity for the thinner elastic layer device and hence a greater degree of ferroelastic switching, or whether it is simply a change in the process-induced damage. In general, the area of the P-E loop increases upon release, regardless of SiO₂ thickness, due to degraded saturation. Internal electric fields may have developed in the PZT film as a result of process-induced defect formation, resulting in an increase in E_c upon release (by ~6 kV/cm and ~27 kV/cm for +E_c and -E_c, respectively). It is probable that P_{max} increases by ~10 μC/cm² upon release due to the declamping effect.[83][137]

The P-E loops for the fixed-fixed beams are similar to that of the cantilevers, as shown in **Figure 4-10** (c). The fixed-fixed beam with SiO₂ thickness of 0.76 μm also has a higher P_{max}. However, the P-E loop of the fixed-fixed beams have greater amounts of pinching, which may be related to microfabrication induced damage. Therefore, no conclusions can be made about the thickness dependence of E_c or P_r for the fixed-fixed beams. Upon poling, P_r, P_{max} and the amount of imprint in the P-E loops does not change, as shown in **Figure 4-10** (d). This further confirms that the damage accrued during additional microfabrication induces large internal fields which overrides the materials' ability to be influenced by an external applied electric field and suppresses the nonlinear ferroelectric response at high applied electric fields.

Differences in the dielectric response of 2.035 μm vs. 0.76 μm thick SiO₂ devices can be detected at low applied AC electric fields (below 0.5*E_c). The irreversible domain wall motion contributions to the dielectric permittivity, α_ε, were measured for (a) clamped, (b) cantilever and (c) fixed-fixed beam devices of varied SiO₂ thicknesses, as shown in **Figure 4-11**. For clamped films, α_ε is independent of SiO₂ thickness, regardless of frequency. However, upon release (and the associated process damage), α_ε decreases by

~70% for both the cantilever and fixed-fixed beams. This decrease is consistent with the imprint and pinching observed in the hysteresis loops. Damage induced during fabrication suppresses the irreversible domain wall motion contributions in the cantilever and fixed-fixed beams. Additionally, for a cantilever and fixed-fixed beam, α_ε depends on SiO₂ thickness. The thicker device with a 2.035 μm SiO₂ layer has a greater irreversible domain wall motion contribution, regardless of frequency. It is not clear if this is a consequence of the difference in elastic layer thickness, or whether it arises in response to run-to-run process variability in the degree of internal fields developed in the PZT films. In principle, the bending or buckling of the devices may lead to mechanical clamping of irreversible domain wall contributions, lowering α_ε . For example, the downward bending of the cantilever with a 0.76 μm SiO₂ layer would place the PZT layer under further tension, reducing the irreversible domain wall contribution to the dielectric response. Likewise, the PZT (which is within the electroded region) of the fixed-fixed beams with a 0.76 μm SiO₂ layer also deflects downward and is put under further tension, reducing irreversible domain wall contributions resulting in a lower α_ε . However, in the cantilever and fixed-fixed beams with a 2.035 μm SiO₂ layer, the device deflects upward. Therefore, the residual in-plane tensile stress in the PZT is partially alleviated, since it is located above the neutral axis, which should result in a higher α_ε .

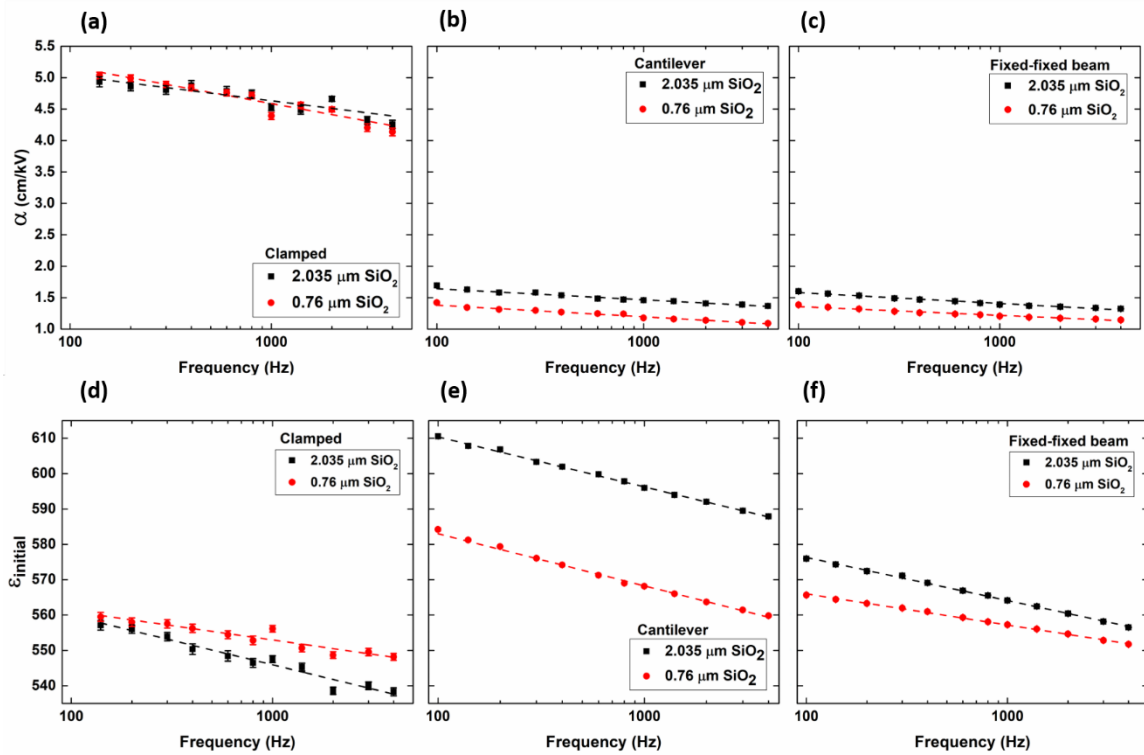


Figure 4-11: Frequency dispersion of the Rayleigh parameter α_ϵ of a (a) clamped PZT 30/70 thin film, (b) cantilever and (c) fixed-fixed beam for a device with a 2.035 μm thick SiO₂ elastic layer and a 0.76 μm thick SiO₂ elastic layer. Also included is the frequency dispersion of the Rayleigh parameter $\epsilon_{initial}$ of a (d) clamped PZT 30/70 thin film, (e) cantilever and (f) fixed-fixed beam for a device with a 2.035 μm thick SiO₂ elastic layer and a 0.76 μm thick SiO₂ elastic layer.

The intrinsic and reversible domain wall motion contributions to the dielectric permittivity, $\epsilon_{initial}$, were measured for (d) clamped, (e) cantilever and (f) fixed-fixed beam devices of varied SiO₂ thicknesses, as shown in **Figure 4-11**. In the clamped state, the PZT films have comparable $\epsilon_{initial}$ at low frequencies (100 Hz) with increasing deviation at higher frequencies (4 kHz). Upon release, $\epsilon_{initial}$ increases for both the cantilever and fixed-fixed beam device, regardless of SiO₂ thickness. The increase in $\epsilon_{initial}$ coupled with the decrease in α_ϵ may suggest that there is a shift of some of the domain walls from irreversible to reversible domain wall motion upon release.[83] The cantilevers and fixed-fixed beams with a 2.035 μm thick SiO₂ elastic layer has a greater $\epsilon_{initial}$, regardless of

frequency. The lower $\varepsilon_{initial}$ seen for PZT on 0.76 μm thick SiO_2 may be related to the downward bending of the cantilever and electroded region of the fixed-fixed beam, which places the PZT layer further in tension and could reduce reversible domain wall motion contributions. The $\varepsilon_{initial}$ for a cantilever is larger than that of a fixed-fixed beam for a fixed SiO_2 thickness. Suppressed $\varepsilon_{initial}$ for the fixed-fixed beam compared to a cantilever is presumably related to the in-plane stresses associated with the buckling.

If a greater volume fraction of *c*-domains existed in the PZT film on a 0.76 μm SiO_2 layer, the $\varepsilon_{initial}$ would be lower, as seen in **Figure 4-11** (e) and (f). However, the motivation for such a domain state is unclear. Since the cantilever with a 0.67 μm SiO_2 layer deflects in the negative *z*-direction, an *a*-domain state would be favorable in the PZT layer which is under further in-plane tension due to the deflection. Therefore, an intrinsically driven dependence of $\varepsilon_{initial}$ on SiO_2 thickness is unlikely.

4.6 Conclusions

Cantilever tip deflections were modeled using Finite Element Analysis (via COMSOL Multiphysics® software) in order to determine the overall residual stresses of the device stack ($\text{IrO}_2/\text{PZT}/\text{PbTiO}_3/\text{Pt}/\text{TiO}_2/\text{SiO}_2$). These models were compared with optical profilometry measurements of the tip displacement. Thicker cantilevers with a 2.035 μm SiO_2 layer exhibited a positive tip displacement of +18.3 μm , whereas thinner cantilevers with a 0.76 μm SiO_2 layer exhibited a negative tip displacement of -26.0 μm . A linear relationship between the cantilever tip displacement and residual stress ratio of PZT to SiO_2 was derived. The differences in magnitude of the tip displacement were attributed to the differences in rigidity of the device stack with SiO_2 thickness. The

differences in the bending of the cantilevers were attributed to competing influences of the integrated stress of the IrO₂ top electrode located above the neutral axis, and the SiO₂ elastic layer located below the neutral axis. To model a self-consistent combination of residual stress of PZT and SiO₂ for each device, the IrO₂ residual stress will need to vary by $\pm 10\%$, based on the COMSOL simulations.

The vertical deflection of fixed-fixed beams was also measured using optical profilometry for bridges with an IrO₂/PZT/PbTiO₃/Pt/TiO₂/SiO₂ device stack near the anchor points and SiO₂ in the center. A third buckling mode shape was observed for the 0.76 μm SiO₂ device compared to the 2.035 μm SiO₂ device which exhibited a first buckling mode shape. The complex, third order buckling is believed to be induced during processing by prematurely releasing the SiO₂ layer near the center of the fixed-fixed beams.

During the release process, microfabrication-induced defects created internal electric fields that suppressed the nonlinear ferroelectric response at high applied electric fields and resulted in pinching of the P-E hysteresis loops. The devices with a thinner SiO₂ layer exhibited downward bending of the electroded regions of the device, placing the PZT layer under further in-plane tension and suppressing the irreversible and reversible domain wall motion contributions to the relative permittivity. Released films, in the form of cantilevers and fixed-fixed beams, showed increased reversible Rayleigh coefficients but decreased irreversible Rayleigh coefficients, relative to the clamped films, suggesting that there was a transition of at least some of the domain walls from irreversible to reversible motion upon release.

Chapter: 5 Conclusions

The primary objective of this work was to investigate the underlying mechanisms that contribute to thickness scaling of ferroelectric thin films. Rayleigh analysis in combination with in situ XRD was used to identify substrate clamping and residual stress as two main factors that contribute to the thickness-dependent extrinsic contributions to the relative permittivity. Additionally, a low dielectric permittivity seed layer, acting as a capacitor in series with the film, contributed to the property degradation and thickness-dependence of the irreversible and reversible contributions to the relative permittivity.

XRD confirmed that the PZT films were under in-plane tensile stress which varied with film thickness and developed during processing. The thinnest 0.27 μm PZT film was under the greatest in-plane tension resulting in the smallest out-of-plane d -spacings (d_{002} and d_{200}). Variations in residual stresses with film thickness also promoted thickness-dependent variations in the domain state. ν_{002} increased with increasing film thickness due to a reduction of the in-plane tensile stresses. This induced a thickness dependence in the intrinsic contributions to the relative permittivity. The reversible Rayleigh coefficient ($\epsilon_{initial}$) decreased as film thickness increased for films $>0.38 \mu\text{m}$ thick.

The full width half maximum of the a -domains also increased with thickness. Based on Williamson Hall analysis, the thickness dependence in the FWHM of the 200 reflections is a result of the thickness dependence in both the crystallite size and the microstrain. The thinnest 0.27 μm thick PZT film had the smallest crystallite size while maintaining grain sizes comparable to films of greater thicknesses. Therefore, the thinner films had the greatest domain wall density which enhanced the irreversible (α_ϵ) and reversible ($\epsilon_{initial}$)

domain wall motion contributions to the relative permittivity. The thickness-dependence in microstrain may be correlated with the thickness dependence in the domain distributions, with a more varied domain distribution (greater ν_{002}) resulting in greater microstrain at the 90° domain wall boundaries. A thickness dependence in point defect concentration can also influence microstrain.

The in-plane residual stress was reduced by bending of released structures. After releasing the films from the substrate and annealing at high temperatures, the d -spacings increased for all film thicknesses, with a greater increase observed for the thinnest 0.27 μm thick PZT film that was under the largest in-plane tensile stress. Additionally, a redistribution of the domain state occurred such that ν_{002} converged for all film thicknesses. Therefore, the thickness dependence that exists for the reversible Rayleigh coefficient ($\varepsilon_{initial}$) is not intrinsically driven. Rather, $\varepsilon_{initial}$ decreases as film thicknesses increases presumably due to a decrease in the domain wall density associated with larger crystallite sizes.

In general, substrate clamping affects both the irreversible and reversible domain wall motion contributions to the relative permittivity. The irreversible Rayleigh coefficient (α_ε) increases when the films are released from the substrate, whereas the reversible Rayleigh coefficient ($\varepsilon_{initial}$) decreases. The observed decrease in $\varepsilon_{initial}$ upon release may suggest that there is a shift of at least some of the domain walls from reversible motion in a clamped film to irreversible motion in a released film. Therefore, the potential energy landscape of a clamped film may have deeper potential energy wells, favoring reversible motion of domain walls; and a released state may favor more shallow potential energy

wells in which irreversible domain wall motion has a higher contribution to the extrinsic response. Additionally, upon release, there is either an increase in the mobility of the existing domain walls active at lower frequencies or an increase in the density of the slower moving domain walls. The increase in irreversible domain wall motion contributions result in enhanced nonlinearity of the P-E loops, with increased P_r and P_{max} upon release.

Upon application of electric field, irreversible changes to ν_{002} , d -spacings and FWHM occur. Therefore, an electric field induced irreversible change in the overall domain state of the film, in which a -domains reorient parallel to the electric field direction and the c -domains coarsen. Ferroelastic, 90° domain reorientation is enhanced in films that are globally released due to the tearing of the diaphragms at applied fields $>1.5 \cdot E_c$. The ν_{002} determined from XRD was used to calculate the intrinsic contributions to the reversible Rayleigh coefficient ($\epsilon_{initial}$) in order to distinguish the reversible extrinsic contributions to the relative permittivity. The thickness-dependence in the reversible, extrinsic contributions persists even after poling and upon release, presumably due to variations in the domain wall density or mobility with film thickness. The thickness dependence in the intrinsic contributions also persists after poling but is alleviated upon release, consistent with the convergence of ν_{002} upon release for all films. The overall response to the relative permittivity is dominated by the reversible, extrinsic contributions which is indirectly affected by residual stress. By combining XRD and Rayleigh analysis, the linear deconstruction of the relative permittivity into its intrinsic, reversible extrinsic contributions and irreversible extrinsic contributions was achieved.

The influence of residual stress on the deflection of PiezoMEMS devices such as cantilevers and fixed-fixed beams were also investigated. For a cantilever with a device stack of IrO₂/PZT/PbTiO₃/Pt/TiO₂/SiO₂, a positive vertical tip displacement of +18.3 μm was achieved for a device with a 2.035 μm SiO₂ layer; whereas, a negative tip displacement of -26.0 μm was achieved for a device with a thinner 0.76 μm SiO₂ layer. The device with a thinner SiO₂ layer achieved a greater overall tip displacement in the negative vertical direction due to its reduced device rigidity. However, the thickness of the SiO₂ layer and its position with respect to the neutral axis dictated whether the device deflected up or down. The stress times thickness ($\sigma_i * t_i$) of the IrO₂ top electrode, located above the neutral axis, competed with that of the SiO₂ elastic layer, located below the neutral axis. The downward bending of the device with a thinner SiO₂ layer places the PZT layer under further in-plane tension. As a result, the irreversible (α_ϵ) and reversible ($\epsilon_{initial}$) Rayleigh coefficients are suppressed for the thinner SiO₂ device.

COMSOL FEA modeling was used to determine the overall residual stresses of the device stack. The models were compared with optical profilometry measurements of the cantilever tip displacement. To appropriately model the tip displacements of each device, the IrO₂ residual stress was varied by ±10% while maintaining a self-consistent combination of residual stress of PZT and SiO₂ for each device. Additionally, a linear relationship between the cantilever tip displacement and residual stress ratio of PZT to SiO₂ was derived.

Buckling was observed for fixed-fixed beams with a device stack of IrO₂/PZT/PbTiO₃/Pt/TiO₂/SiO₂ present near the beam anchor points and SiO₂ only in the center. The device with a thinner SiO₂ layer exhibited a third buckling mode shape which

is believed to be a consequence of inhomogeneous release of the central SiO₂ regions during the XeF₂ etch. As a result, the central SiO₂ regions deflected upward, whereas the electroded regions deflected downward, resulting in the complex third order buckling. In general, the release process and extensive microfabrication induced defects in the PZT film that suppressed the nonlinear-ferroelectric response. This resulted in both pinching of the P-E loops at high AC electric fields and reduced reversible ($\epsilon_{initial}$) and irreversible (α_ϵ) Rayleigh coefficients at low AC electric fields. Therefore, although releasing the film from the substrate can improve the dielectric and piezoelectric properties, the release process may induce defects in the piezoelectric layer that may compromise device performance.

Chapter: 6 Future Work

6.1 Depth Profiling using X-ray Diffraction

Many factors have been identified in this work as thickness-dependent, including in-plane tensile stress, d -spacings, volume fraction of c -domains, full width at half maximum of the 200 reflection, crystallite size, microstrain, domain wall density, etc. The observed thickness dependence develops during CSD processing and contributes to the overall scaling effects in clamped PZT thin films fabricated on Si substrates. However, the variation of these factors as a function of film depth should be better quantified.

It is difficult to depth profile the structure of multilayered films using a nondestructive characterization technique that maintains a constant penetration volume.[138] Cross-sectional techniques such as transmission electron microscopy (TEM) can maintain a constant penetration volume during depth profile analysis. However, the fabrication of film cross-sections is a destructive process that often involves ion milling which can induce residual strains and alter the structure at the milled surface.[139]. Additionally, removing portions of the film from the substrate to create a cross-section can alleviate residual in-plane stresses (or stress gradients) that may have existed in the clamped state. Therefore, it is preferable to investigate non-destructive methods for depth profiling.

6.1.1 *Glancing-incidence X-ray Diffraction*

XRD techniques such as grazing-incidence diffraction (GID) [140][141], also known as glancing-angle XRD or glancing-incidence XRD [142]) allow for non-destructive depth profiling of the film structure (thickness, phase, etc.) and microstructure

(strain field, defects, preferred orientation, d -spacing, crystallite size, etc.) by varying the incidence angle of the X-ray beam. However, with these techniques, it is not possible to maintain a constant penetration volume during depth profiling.

As the incidence angle increases, the penetration depth of the X-rays increases such that the measured d -spacing is the average response of a greater irradiated volume. Equation 6-1 relates the incidence angle (θ) to the X-ray penetration depth (z) and the distance (t) that the transmitted beam passes through the medium for a given beam intensity ($\frac{I}{I_0} * 100\%$).

$$\sin \theta = \frac{z}{t} \quad 6-1$$

The beam intensity can be calculated using Equation 6-2, where $\frac{\mu}{\rho}$ is the mass absorption coefficient, ρ is the density, I_0 is the incident intensity of the X-ray beam, and I is the transmitted intensity of the X-ray beam.

$$\frac{I}{I_0} = e^{-\left(\frac{\mu}{\rho}\right)\rho t} \quad 6-2$$

Using Equations 6-1 and 6-2, the intensity of X-rays that penetrate the film-substrate interface for a given film thickness and incidence angle can be calculated. For GID of a 0.5 μm thick PZT 30/70 film in which the incidence angle varies between 0.1° (near the critical angle) and $\sim 1.3^\circ$, depth profiling can be conducted since the X-rays penetrate the entire sample thickness (with a 5% intensity at the film-substrate interface).[143]

GID with an incidence angle corresponding to a penetration depth that exceeds the film thickness are qualitative depth profiling techniques that compare average parameters at the film surface vs. the bulk of the film.[140] For example, Araujo *et al.* attempted to

measure depth-dependent changes in microstrain and crystallite size of a 0.71 μm thick PZT 50/50 film using GID.[31][97] However, large error bars are reported for incidence angles between 3° and 6° , suggesting that statistically insignificant changes in microstrain, crystallite size and tetragonality factor c/a . The large error may be related to a convoluted response when using large incidence angles. The X-ray penetration depth was equivalent to or greater than the film thickness even at the smallest incidence angle used in the study (2°).[31] Therefore, the data collected at the smallest incidence angle (2°) is an average response of the entire film that is weighted with a greater X-ray intensity at the film surface compared to the film-substrate interface ($\sim 5\%$ intensity at interface) of the 0.71 μm thick PZT 50/50 film used in the study. In contrast, Pietsch *et al.* limited the incidence angle to $\leq 0.8^\circ$ while investigating the progressive state of relaxation of strained superlattice layers of $\text{Ga}_{1-x}\text{In}_x\text{As}/\text{GaAs}$ and showed statistically significant changes in in-plane lattice mismatch with incident angle.[140] Kelman *et al.* reported a coexistence of tetragonal and rhombohedral phases in polycrystalline PZT 35/65 thin films.[143] The variation in the volume fraction of the rhombohedral phase was successfully quantified using GID when varying the incidence angle between 1° and 0.2° , as shown in **Figure 6-1**.

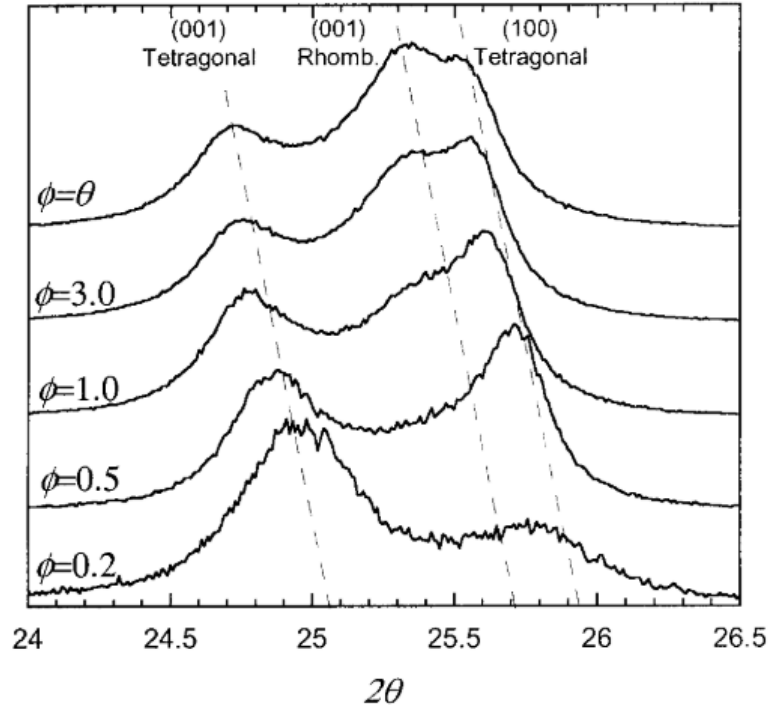


Figure 6-1: Grazing incidence XRD patterns of polycrystalline PZT 35/65 thin films. The evolution of the phase coexistence of tetragonal and rhombohedral phases as a function of incidence angle (i.e. film depth) is shown. This figure was taken from M. B. Kelman *et al.*[143]

The $\sin^2\psi$ method can be used to deconvolute in-plane (ε_{\parallel}) and out-of-plane strain (ε_{\perp}) response measured during GID, using Equation 6-3, in which ψ is the angle between the surface normal and diffraction vector at a given angle of incidence.[144]

$$\varepsilon_{\psi} = \varepsilon_{\parallel}\sin^2\psi + \varepsilon_{\perp}\cos^2\psi \quad 6-3$$

This equation is derived from the measured strained lattice reflections using X-ray diffraction and the elastic response of material (generalized Hooke's Law).[145] Based on the diffraction geometry, a set of lattice spacings (d_{ψ}^{hkl}) are identified for measured angles (θ_{ψ}^{hkl}) at various tilt angles (ψ) using Bragg's law. It is assumed that the films are sufficiently textured such that strain can be measured by varying the tilt angles (ψ) exclusively.[138] This equation is simplified, based on the assumption that the in-plane

strain is a result of equal biaxial stress (i.e. $\sigma_{11} = \sigma_{22} = \sigma_{\parallel}$). A linear relationship can be made between the measured strain (ε_{ψ}) and $\sin^2\psi$, in which the slope is the in-plane strain (ε_{\parallel}).

6.1.2 X-ray Nanodiffraction

By reducing the waist of the X-ray beam down to 50 nm or less, the spatial resolution for XRD depth profiling of microstructure (including texture and crystallite size) and residual stress gradients can be improved.[138] Synchrotron radiation facilities such as The Advanced Photon Source (APS) beamline 2-ID-D[89], the sector 26 Hard X-ray Nanoprobe (HXN)[146], the European Synchrotron Radiation Facility (ESRF) beamlines ID01[147], ID11[148] and ID13[149][150][151][152], or the Petra III beamline P03[153] and P07[154] uses Fresnel zone plates, parabolic refractive X-ray lenses, and multilayer Laue lenses to focus an X-ray beam to a spot size ranging from 25 nm to 250 nm. With a monochromatic, high energy (>40 keV) X-ray beam, penetration through the entire sample width (in the direction of X-ray beam propagation) is possible in transmission mode for samples of width < 400 μm (in the direction of the y-axis as indicated in **Figure 6-2** (a)).[148] In transmission mode, residual stress depth profiling can be accomplished by fixing the incident beam perpendicular to the normal vector of the film surface while vertically scanning the cross-section of the film with a step size that is greater than the X-ray nanobeam height, as shown in **Figure 6-2** (a). A charge coupled device (CCD) area detector is positioned at a distance from the sample such that a Debye-Scherrer diffraction frame of {002} PZT reflections are acquired.

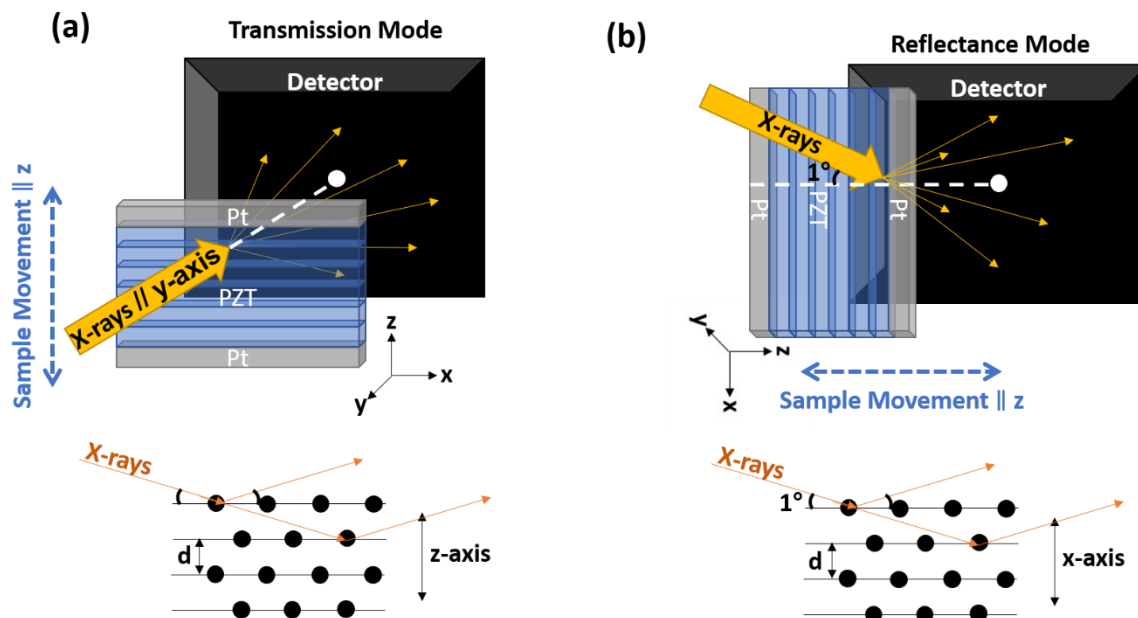


Figure 6-2: Schematics comparing techniques for using nanoprobe X-ray diffraction in (a) transmission mode and (b) grazing incidence angle reflectance mode in order to achieve depth profiling of strain and domain distributions in a multilayered ferroelectric thin film.

In reflectance mode, however, the high energy synchrotron radiation will result in X-ray penetration occurs at an angle (dictated by the incident angle). Therefore, the X-rays will penetrate through the depth (along the z-axis) of the sample, even at small incident angles ($< 1^\circ$). To prevent X-ray penetration through multiple crystallization layers in a film, an alternative sample set up is proposed for depth profiling in reflection mode using high energy, synchrotron X-rays, as shown in **Figure 6-2** (b). If the sample is rotated 90° about the X-ray propagation axis, then the X-ray penetration would be within the plane of the film, i.e. within a crystallized layer. With this sample orientation and diffraction set up, residual stress depth profiling can be accomplished in reflectance mode with a 1° incident angle while laterally scanning the cross section of the film.

The sample dimensions needed for X-ray nanodiffraction can be fabricated using focused ion beam or reactive ion etched pillars. Using nanodiffraction, Keech *et al.* was

able to investigate clamping effects by scanning laterally across pillars while applying electric fields *in situ*. This study confirmed that patterning relieves local stresses imposed by the substrate in regions $\sim 1 \mu\text{m}$ from the edges of the pillars, resulting in increased out-of-plane lattice parameters near the free sidewalls and an enhanced intrinsic piezoelectric coefficient.[89] Therefore, it is necessary to probe stress gradients as a function of film depth in central, clamped regions of pillars $>2.05 \mu\text{m}$ in width to avoid the influence of edge effects (assuming an X-ray width of 50 nm).

6.1.3 *In Situ X-ray Microscopy*

If a residual stress gradient exists along the film thickness, then high stressed regions will have suppressed ferroelastic properties which could limit thin film device performance. It is critical to understand and model the impact of stress gradients, grain boundaries and other interfaces on the dynamics of domain wall motion. X-ray nanodiffraction, mentioned in the previous section, can be used *in situ* while applying electric fields to measure 90° domain wall reorientation at different depths in the film.[148] However, this technique is limited in terms of the structural length scales investigated and is unable to probe real-time domain wall motion. In contrast, Dark-field X-ray Diffraction Microscopy (DF-XRM) is a full-field imaging technique that shows promise for nondestructive, three-dimensional (3D) multi-scale mapping of structure, orientation and strain of crystallites and grains within millimeter-sized samples.[155][156][157]

DF-XRM uses an X-ray objective lens to magnify diffracted X-rays from the sample onto a 2D area detector by up to 50x magnification, as shown in **Figure 6-3**. [157] Additionally, the objective acts as a collimator and filters diffraction signals from other grains/domains, deconvoluting the response. DF-XRM is available at the ESRF beamline

ID06 with X-ray energies ranging from 15-35 keV, spatial resolution of $\sim 100\text{nm}$, field of view of $100\ \mu\text{m}$, strain resolution $>10^{-4}$, angular resolution of 0.001° and exposure times on the order of 1 sec. With this accuracy, DF-XRM can perform spatial mapping of lattice symmetry and strain across individual domain walls or features $>0.2\ \mu\text{m}$ within a bulk or thin film ferroelectric.

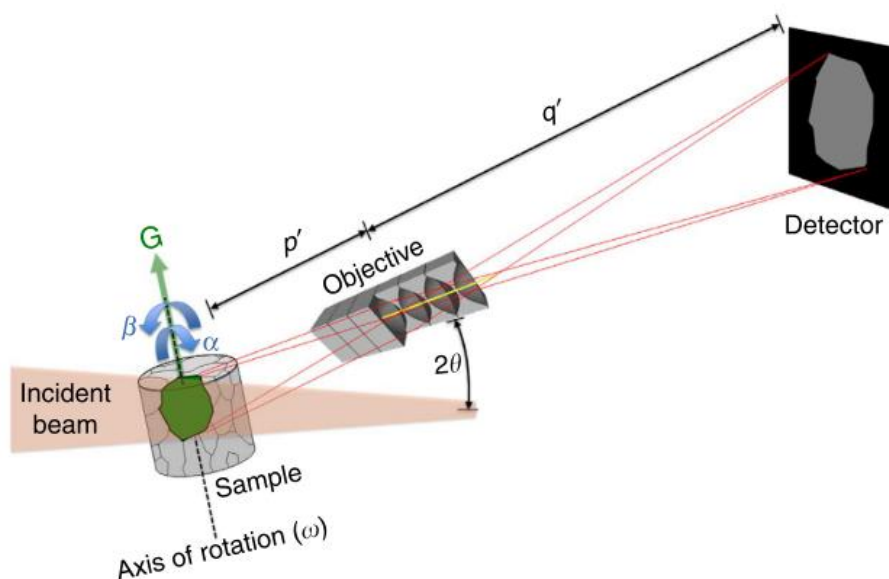


Figure 6-3: A diagram of the experimental set up for multi-scale 3D imaging of strain and structure using dark-field X-ray microscopy. Figure taken from H. Simons *et al.*[157]

Although DF-XRM is a promising technique for spatially investigating residual stress gradients and variable domain distributions, the speed and the spatial resolution need to be improved to characterize domain wall dynamics in a ferroelectric thin film. The use of the multilayer Laue lens as the magnification objective will improve the spatial resolution down to 25 nm and magnification by four-fold.[158] Additionally, it is proposed that diffraction-limited synchrotron storage rings will boost imaging rate by a factor of 100x-1000x. By improving imaging rate and spatial resolution, real-time DF-XRM of the

electric-field induced movement of a single domain wall and the correlated motion of domain walls within a crystallite is obtainable.

6.2 Application of Relative Permittivity Deconstruction

6.2.1 Assessing the Possibility of a Critical Film Thickness

In Chapter 3 of this thesis, the intermediate film thickness of 0.38 μm often exhibited superior values for Rayleigh coefficients α_ϵ and $\epsilon_{initial}$, presumably due to its relatively high domain wall density compared to thicker films and lower defect density compared to thinner films in the study. It is of interest to determine whether a critical thickness exists between 0.27 μm and 0.56 μm in which superior dielectric and piezoelectric properties are achievable, or whether this observation was simply a consequence of reduced defect concentrations induced during processing of this particular film. X-ray diffraction and Rayleigh analysis can be used to deconstruct the contributions to the relative permittivity as a function of film thickness. The film thicknesses can be controlled by varying the number of crystallized layers during CSD. Assuming each layer is ~ 60 nm thick if spun at 3000 rpm, the number of crystallized layers can be varied from 3 to 7 layers (not including the seed layer) to achieve film thicknesses ranging from 0.27 μm to 0.5 μm . Within this thickness range, 5 samples of varying thicknesses can be produced by incrementally increasing the number of crystallized layers by one for each subsequent film.

As film thickness decreases, the defect density will increase since the interfacial regions with high concentrations of lead vacancies will make up a greater overall volume fraction of the film. High defect densities will suppress the extrinsic response to the relative permittivity in thinner films. However, as film thickness decreases, domain wall density is

observed to increase which will enhance the extrinsic response to the relative permittivity. Therefore, within the suggested film thickness range, a compromise will be made between the domain wall density and the defect density to achieve enhanced extrinsic contributions to the relative permittivity. It would also be interesting to anneal the resulting films in a PbO-rich atmosphere in order to alter the concentration of Pb-based defects through the film thickness. This could be done using a furnace described by Marincel *et al.*[159]

6.2.2 Permittivity Deconstruction for Various Compositions

The deconstruction of the relative permittivity into its constituent components is a powerful technique that can be used to quantify changes in the intrinsic and extrinsic contributions as a function of Zr/Ti ratio in the PZT system. This would allow the relative roles of phase, tilt structure, and phase coexistence to be investigated. For example, it has been reported in ceramics that both the intrinsic and extrinsic contributions to the properties peak at the morphotropic phase boundary (MPB). At the MPB, the intrinsic polarizabilities rise, as described by Haun *et al.*[25] The phase coexistence at the MPB also influences the extrinsic contributions by creating a flattened potential energy landscape that lowers the energy penalty associated with making domain walls (so that domain wall densities rise).[160] However, due to the multiphase coexistence in films at the MPB, the reflections in XRD patterns are often broad and convoluted, making peak fitting difficult. Therefore, it is suggested that the composition be limited to the tetragonal region of the phase diagram that approach the MPB while still have distinct splitting of the 002/200 peaks.

6.3 TEM Analysis of Domain Structure

In order to confirm the model of the domain structure developed in Chapter 3 of this thesis, transmission electron microscopy (TEM) measurements are proposed. TEM images of the domain structure can be compared as a function of film thickness. It is expected that the domain wall density increases (i.e. crystallite size decreases) as film thickness decreases; whereas the volume fraction of *c*-domains decreases as film thickness decreases. Additionally, Rayleigh analysis in combination with XRD was used to determine the mechanism that caused the thickness dependent change in $\epsilon_{initial}$ upon poling. It is proposed that the greater change in $\epsilon_{initial}$ upon poling for thicker films is due to a greater coarsening of *c*-domains and enhanced reversible 180° domain reorientation. This hypothesis can be confirmed using TEM by comparing the observed domain state before and after poling for each film thickness in this study. Since the domain structure on the surface of PZT samples can be altered by mechanical grinding, TEM samples should be prepared via dual beam FIB/SEM to avoid domain reorientation during TEM sample preparation.

6.4 Detecting Dead-layers using Curie-Weiss Behavior

This work identified the presence of a low-dielectric seed layer that acted in series with the film to lower the overall measured capacitance and dielectric properties. However, it is important to investigate whether the low dielectric response of the seed layer was in actuality due to the presence of interfacial regions with high defect concentrations. The relative permittivity reported for the films in this study is significantly lower than that reported for bulk PZT ceramics of comparable composition. This is, in part, due to the

presence of low dielectric interfacial layers or “dead-layers”. These dead-layers are believed to form at the film-electrode interfaces and have a high concentration of point defects (i.e. lead vacancies) due to lead volatility during crystallization or lead loss to the underlying electrode. As the concentration of defects increases (i.e. as film thickness decreases), the maximum in the relative permittivity at T_c drops and the distribution broadens. By measuring the Curie Weiss behavior above T_c , it should be possible to eliminate convolution of the domain state from the defect concentrations. The Curie-Weiss relationship describes the change in the relative permittivity at temperatures when the films is in the paraelectric phase, shown in Equation 6-4.

$$\epsilon_{eff} \sim \frac{C}{T-\theta} \quad 6-4$$

In this equation, C is the Curie constant, and θ is the Curie-Weiss temperature. It has been shown that C and θ decrease as the concentration of low-dielectric grain boundaries increases (i.e. as grain size decreases).[161] Therefore, it is expected that these parameters will also vary with film thickness, since it is expected that defect concentration increases as film thickness decreases. This has been observed by Park *et al.* who investigated the film thickness dependent Curie-Weiss behavior of (Ba,Sr)TiO₃ thin films.[162] Based on the relationship between C vs. film thickness and θ vs. film thickness, the effective relative permittivity of a dead-layer can be extrapolated.

References

- [1] R.E. Newnham, *Properties of Materials: Anisotropy, Symmetry, Structure*, 2005.
- [2] J. Nye, *Physical Properties of Crystals: Their Representation by Tensors and Matrices*, 1985.
- [3] P. Muralt, Ferroelectric thin films for micro-sensors and actuators: a review, *J. Micromechanics Microengineering*. 10 (2000) 136–146. doi:10.1088/0960-1317/10/2/307.
- [4] G.L. Smith, J.S. Pulskamp, L.M. Sanchez, D.M. Potrepka, R.M. Proie, T.G. Ivanov, R.Q. Rudy, W.D. Nothwang, S.S. Bedair, C.D. Meyer, R.G. Polcawich, PZT-based piezoelectric MEMS technology, *J. Am. Ceram. Soc.* 95 (2012) 1777–1792. doi:10.1111/j.1551-2916.2012.05155.x.
- [5] J.S. Pulskamp, R.G. Polcawich, R.Q. Rudy, S.S. Bedair, R.M. Proie, T. Ivanov, G.L. Smith, Piezoelectric PZT MEMS technologies for small-scale robotics and RF applications, *MRS Bull.* 37 (2012) 1062–1070. doi:10.1557/mrs.2012.269.
- [6] P. Muralt, Recent progress in materials issues for piezoelectric MEMS, *J. Am. Ceram. Soc.* 91 (2008) 1385–1396. doi:10.1111/j.1551-2916.2008.02421.x.
- [7] J.S. Pulskamp, R.G. Polcawich, K. Oldham, Highly integrated PiezoMEMS enabled millimeter-scale robotics, in: Vol. 6 ASME Power Transm. Gearing Conf. 3rd Int. Conf. Micro- Nanosyst. 11th Int. Conf. Adv. Veh. Tire Technol., ASME,

- 2009: pp. 797–805. doi:10.1115/DETC2009-87231.
- [8] P. Muralt, R.G. Polcawich, S. Trolier-McKinstry, Piezoelectric thin films for sensors, actuators, and energy harvesting, *MRS Bull.* 34 (2009) 658–664. doi:10.1557/mrs2009.177.
- [9] P. Muralt, N. Ledermann, J. Paborowski, A. Barzegar, S. Gentil, B. Belgacem, S. Petitgrand, A. Bosseboeuf, N. Setter, Piezoelectric micromachined ultrasonic transducers based on PZT thin films, *IEEE Trans. Ultrason. Ferroelectr. Freq. Control.* 52 (2005) 2276–2288. doi:10.1109/TUFFC.2005.1563270.
- [10] S.S.N. Bharadwaja, M. Olszta, S. Trolier-McKinstry, X. Li, T.S. Mayer, F. Roozeboom, Fabrication of high aspect ratio ferroelectric microtubes by vacuum infiltration using macroporous silicon templates, *J. Am. Ceram. Soc.* 89 (2006) 2695–2701. doi:10.1111/j.1551-2916.2006.01123.x.
- [11] I. Kanno, Piezoelectric MEMS: Ferroelectric thin films for MEMS applications, *Jpn. J. Appl. Phys.* 57 (2018) 040101. doi:10.7567/JJAP.57.040101.
- [12] K. Wasa, T. Matsushima, H. Adachi, I. Kanno, H. Kotera, Thin-film piezoelectric materials for a better energy harvesting MEMS, *J. Microelectromechanical Syst.* 21 (2012) 451–457. doi:10.1109/JMEMS.2011.2181156.
- [13] A.W. Glass, M.E. Lines, *Principles and Applications of Ferroelectrics and Related Materials*, 2001.
- [14] Bernard Jaffe, *Piezoelectric Ceramics*, 2012.

- [15] B. Jaffe, W. R. Cook Jr., H. Jaffe, *Piezoelectric Ceramics*, 1971. doi:77-153538.
- [16] V.M. Goldschmidt, Crystal structure and chemical constitution, *Trans. Faraday Soc.* 25 (1929) 253. doi:10.1039/tf9292500253.
- [17] A.K. Tagantsev, E.L. Cross, J. Fousek, *Domains in Ferroic Crystals and Thin Films*, 2010.
- [18] D. Damjanovic, Ferroelectric, dielectric and piezoelectric properties of ferroelectric thin films and ceramics, *Reports Prog. Phys.* 61 (1999) 1267.
- [19] G. Bertotti, I. Mayergoyz, *The Science of Hysteresis*, 2006.
- [20] D. Damjanovic, M. Demartin, The Rayleigh law in piezoelectric ceramics, *J. Phys. D. Appl. Phys.* 29 (1999) 2057–2060. doi:10.1088/0022-3727/29/7/046.
- [21] S. Trolier-McKinstry, N. Bassiri Gharb, D. Damjanovic, Piezoelectric nonlinearity due to motion of 180° domain walls in ferroelectric materials at subcoercive fields: A dynamic poling model, *Appl. Phys. Lett.* 88 (2006) 202901. doi:10.1063/1.2203750.
- [22] J.L. Jones, E.B. Slamovich, K.J. Bowman, Domain texture distributions in tetragonal lead zirconate titanate by x-ray and neutron diffraction, *J. Appl. Phys.* 97 (2005) 034113. doi:10.1063/1.1849821.
- [23] T. Key, J.L. Jones, W.F. Shelley, K.J. Bowman, Quantifying domain textures in lead zirconate titanate using 022:202 and 220 diffraction peaks, *Solid State*

- Phenom. 105 (2005) 379–384. doi:10.4028/www.scientific.net/SSP.105.379.
- [24] International Centre for Diffraction Data, in Card 01-070-4261, (n.d.).
- [25] M.J. Haun, E. Furman, S.J. Jang, L.E. Cross, Thermodynamic theory of the lead zirconate-titanate solid solution system, part V: theoretical calculations, *Ferroelectrics*. 99 (1989) 63–86. doi:10.1080/00150198908221440.
- [26] S.P. Murarka, *Metallization Theory And Practice For VLSI And ULSI*, 1993.
- [27] F. Xu, S. Trolier-McKinstry, W. Ren, B. Xu, Z.-L. Xie, K.J. Hemker, Domain wall motion and its contribution to the dielectric and piezoelectric properties of lead zirconate titanate films, *J. Appl. Phys.* 89 (2001) 1336–1348. doi:10.1063/1.1325005.
- [28] L. Pintilie, I. Vrejoiu, D. Hesse, G. LeRhun, M. Alexe, Extrinsic contributions to the apparent thickness dependence of the dielectric constant in epitaxial $\text{Pb}(\text{Zr},\text{Ti})\text{O}_3$ thin films, *Phys. Rev. B*. 75 (2007) 224113. doi:10.1103/PhysRevB.75.224113.
- [29] Y. Bastani, T. Schmitz-Kempen, A. Roelofs, N. Bassiri-Gharb, Critical thickness for extrinsic contributions to the dielectric and piezoelectric response in lead zirconate titanate ultrathin films, *J. Appl. Phys.* 109 (2011) 014115. doi:10.1063/1.3527970.
- [30] R.J. Ong, D.A. Payne, N.R. Sottos, Processing effects for integrated PZT: residual stress, thickness, and dielectric properties, *J. Am. Ceram. Soc.* 88 (2005) 2839–

2847. doi:10.1111/j.1551-2916.2005.00641.x.

- [31] E.B. Araújo, E.C. Lima, I.K. Bdikin, A.L. Kholkin, Thickness dependence of structure and piezoelectric properties at nanoscale of polycrystalline lead zirconate titanate thin films, *J. Appl. Phys.* 113 (2013) 187206. doi:10.1063/1.4801961.
- [32] V. Nagarajan, J. Junquera, J.Q. He, C.L. Jia, R. Waser, K. Lee, Y.K. Kim, S. Baik, T. Zhao, R. Ramesh, P. Ghosez, K.M. Rabe, Scaling of structure and electrical properties in ultrathin epitaxial ferroelectric heterostructures, *J. Appl. Phys.* 100 (2006) 051609. doi:10.1063/1.2337363.
- [33] T.A. Berfield, R.J. Ong, D.A. Payne, N.R. Sottos, Residual stress effects on piezoelectric response of sol-gel derived lead zirconate titanate thin films, *J. Appl. Phys.* 101 (2007) 024102. doi:10.1063/1.2422778.
- [34] J.F. Ihlefeld, D.T. Harris, R. Keech, J.L. Jones, J.-P. Maria, S. Trolier-McKinstry, Scaling effects in perovskite ferroelectrics: fundamental limits and process-structure-property relations, *J. Am. Ceram. Soc.* 99 (2016) 2537–2557. doi:10.1111/jace.14387.
- [35] M. Randall, D. Skamser, T. Kinard, J. Qazi, A. Tajuddin, S. Trolier-Mckinstry, C. Randall, W. Ko, T. Dechakupt, Thin film MLCC, *Cart. 2007 Electron. Components, Assem. Mater. Assoc.* (2007) 1–12.
- [36] H. Kishi, Y. Mizuno, H. Chazono, Base-metal electrode-multilayer ceramic capacitors: past, present and future perspectives, *Jpn. J. Appl. Phys.* 42 (2003) 1–

15. doi:10.1143/JJAP.42.1.
- [37] D. Newns, B. Elmegreen, X. Hu Liu, G. Martyna, A low-voltage high-speed electronic switch based on piezoelectric transduction, *J. Appl. Phys.* 111 (2012) 084509. doi:10.1063/1.4704391.
- [38] T.M. Shaw, S. Trolier-McKinstry, P.C. McIntyre, The properties of ferroelectric films at small dimensions, *Annu. Rev. Mater. Sci.* 30 (2000) 263–298. doi:10.1146/annurev.matsci.30.1.263.
- [39] D.D. Fong, Ferroelectricity in ultrathin perovskite films, *Science* (80-.). 304 (2004) 1650–1653. doi:10.1126/science.1098252.
- [40] F. Chu, F. Xu, J. Shepard, S. Trolier-McKinstry, Thickness dependence of the electrical properties of sol-gel derived lead zirconate titanate thin films with (111) and (100) texture, *MRS Proc.* 493 (1997) 409. doi:10.1557/PROC-493-409.
- [41] D.-J. Kim, J.-P. Maria, A.I. Kingon, S.K. Streiffer, Evaluation of intrinsic and extrinsic contributions to the piezoelectric properties of $\text{Pb}(\text{Zr}_{1-x}\text{Ti}_x)\text{O}_3$ thin films as a function of composition, *J. Appl. Phys.* 93 (2003) 5568–5575. doi:10.1063/1.1566478.
- [42] J. Pérez de la Cruz, E. Joanni, P.M. Vilarinho, A.L. Kholkin, Thickness effect on the dielectric, ferroelectric, and piezoelectric properties of ferroelectric lead zirconate titanate thin films, *J. Appl. Phys.* 108 (2010) 114106. doi:10.1063/1.3514170.

- [43] N. Bassiri-Gharb, I. Fujii, E. Hong, S. Trolier-McKinstry, D. V. Taylor, D. Damjanovic, Domain wall contributions to the properties of piezoelectric thin films, *J. Electroceramics*. 19 (2007) 49–67. doi:10.1007/s10832-007-9001-1.
- [44] I.F. Fujii, E.H. Hong, S. Trolier-McKinstry, Thickness dependence of dielectric nonlinearity of lead zirconate titanate films, *IEEE Trans. Ultrason. Ferroelectr. Freq. Control*. 57 (2010) 1717–1723. doi:10.1109/TUFFC.2010.1610.
- [45] P. Bintachitt, S. Jesse, D. Damjanovic, Y. Han, I.M. Reaney, S. Trolier-McKinstry, S. V Kalinin, T. Nattermann, Collective dynamics underpins Rayleigh behavior in disordered polycrystalline ferroelectrics, *Proc. Natl. Acad. Sci.* 107 (2010) 7219–7224. doi:10.1073/pnas.0913172107.
- [46] W. Zhu, I. Fujii, W. Ren, S. Trolier-McKinstry, Influence of Mn doping on domain wall motion in $\text{Pb}(\text{Zr}_{0.52}\text{Ti}_{0.48})\text{O}_3$ films, *J. Appl. Phys.* 109 (2011) 064105. doi:10.1063/1.3552298.
- [47] C.-R. Cho, W.-J. Lee, B.-G. Yu, B.-W. Kim, Dielectric and ferroelectric response as a function of annealing temperature and film thickness of sol-gel deposited $\text{Pb}(\text{Zr}_{0.52}\text{Ti}_{0.48})\text{O}_3$ thin film, *J. Appl. Phys.* 86 (1999) 2700–2711. doi:10.1063/1.371114.
- [48] A.J. Welsh, R.H.T. Wilke, M.A. Hickner, S. Trolier-McKinstry, Low-cost, damage-free patterning of lead zirconate titanate films, *J. Am. Ceram. Soc.* 96 (2013) 2799–2805. doi:10.1111/jace.12505.

- [49] D.-J. Kim, J.-H. Park, D. Shen, J.W. Lee, A.I. Kingon, Y.S. Yoon, S.-H. Kim, Thickness dependence of submicron thick $\text{Pb}(\text{Zr}_{0.3}\text{Ti}_{0.7})\text{O}_3$ films on piezoelectric properties, *Ceram. Int.* 34 (2008) 1909–1915. doi:10.1016/j.ceramint.2007.07.016.
- [50] V. Nagarajan, A. Roytburd, A. Stanishevsky, S. Prasertchoung, T. Zhao, L. Chen, J. Melngailis, O. Auciello, R. Ramesh, Dynamics of ferroelastic domains in ferroelectric thin films, *Nat. Mater.* 2 (2003) 43–47. doi:10.1038/nmat800.
- [51] M. Wallace, R.L. Johnson-Wilke, G. Esteves, C.M. Fancher, R.H.T. Wilke, J.L. Jones, S. Trolier-McKinstry, In situ measurement of increased ferroelectric/ferroelastic domain wall motion in declamped tetragonal lead zirconate titanate thin films, *J. Appl. Phys.* 117 (2015) 054103. doi:10.1063/1.4907394.
- [52] S. Bühlmann, B. Dwir, J. Baborowski, P. Muralt, Size effect in mesoscopic epitaxial ferroelectric structures: Increase of piezoelectric response with decreasing feature size, *Appl. Phys. Lett.* 80 (2002) 3195–3197. doi:10.1063/1.1475369.
- [53] A. Bernal, A. Tselev, S. Kalinin, N. Bassiri-Gharb, Free-standing ferroelectric nanotubes processed via soft-template infiltration, *Adv. Mater.* 24 (2012) 1160–1165. doi:10.1002/adma.201103993.
- [54] F. Griggio, S. Jesse, A. Kumar, O. Ovchinnikov, H. Kim, T.N. Jackson, D. Damjanovic, S. V. Kalinin, S. Trolier-McKinstry, Substrate clamping effects on irreversible domain wall dynamics in lead zirconate titanate thin films, *Phys. Rev.*

- Lett. 108 (2012) 157604. doi:10.1103/PhysRevLett.108.157604.
- [55] C. Yeager, PZT thin films for piezoelectric MEMS mechanical energy harvesting, Ph.D. Thesis Mater. Sci. Eng. Pennsylvania State Univ. (2015).
- [56] M.D. Nguyen, M. Dekkers, H.N. Vu, G. Rijnders, Film-thickness and composition dependence of epitaxial thin-film PZT-based mass-sensors, *Sensors Actuators A Phys.* 199 (2013) 98–105. doi:10.1016/j.sna.2013.05.004.
- [57] N. Ledermann, P. Mural, J. Baborowski, S. Gentil, K. Mukati, M. Cantoni, A. Seifert, N. Setter, {100}-Textured, piezoelectric $\text{Pb}(\text{Zr}_x\text{Ti}_{1-x})\text{O}_3$ thin films for MEMS: integration, deposition and properties, *Sensors Actuators A Phys.* 105 (2003) 162–170. doi:10.1016/S0924-4247(03)00090-6.
- [58] S.K. Dey, K.D. Budd, D.A. Payne, Thin-film ferroelectrics of PZT of sol-gel processing, *IEEE Trans. Ultrason. Ferroelectr. Freq. Control.* 35 (1988) 80–81. doi:10.1109/58.4153.
- [59] T.M. Borman, S.W. Ko, P. Mardilovich, S.E. Trolier-McKinstry, Development of crystallographic texture in chemical solution deposited lead zirconate titanate seed layers, *J. Am. Ceram. Soc.* 100 (2017) 4476–4482. doi:10.1111/jace.15019.
- [60] T. Doi, H. Sakurai, N. Soyama, Method of forming PNBZT ferroelectric thin film, Pat. Appl. EP2784802 A1. (2014).
- [61] G.L. Brennecke, C.M. Parish, B.A. Tuttle, L.N. Brewer, M.A. Rodriguez, Reversibility of the perovskite-to-fluorite phase transformation in lead-based thin

and ultrathin films, *Adv. Mater.* 20 (2008) 1407–1411.

doi:10.1002/adma.200702442.

- [62] G. Esteves, K. Ramos, C.M. Fancher, J.L. Jones, LIPRAS : Line-Profile Analysis Software, DOI 10.13140/RG.2.2.29970.25282/3. (2017) 1–4.
doi:10.13140/RG.2.2.29970.25282/3.
- [63] J.E. Daniels, J.L. Jones, T.R. Finlayson, Characterization of domain structures from diffraction profiles in tetragonal ferroelastic ceramics, *J. Phys. D. Appl. Phys.* 39 (2006) 5294–5299. doi:10.1088/0022-3727/39/24/029.
- [64] A.K. Tagantsev, M. Landivar, E. Colla, N. Setter, Identification of passive layer in ferroelectric thin films from their switching parameters, *J. Appl. Phys.* 78 (1995) 2623–2630. doi:10.1063/1.360122.
- [65] A.K. Tagantsev, G. Gerra, Interface-induced phenomena in polarization response of ferroelectric thin films, *J. Appl. Phys.* 100 (2006) 051607.
doi:10.1063/1.2337009.
- [66] C. Basceri, S.K. Streiffer, A.I. Kingon, R. Waser, The dielectric response as a function of temperature and film thickness of fiber-textured (Ba,Sr)TiO₃ thin films grown by chemical vapor deposition, *J. Appl. Phys.* 82 (1997) 2497–2504.
doi:10.1063/1.366062.
- [67] Y. Xia, J. Wang, Switching behavior of ferroelectric thin films with deadlayers, *Smart Mater. Struct.* 21 (2012) 094019. doi:10.1088/0964-1726/21/9/094019.

- [68] B.A. Tuttle, R.W. Schwartz, Solution deposition of ferroelectric thin films, *MRS Bull.* 21 (1996) 49–54. doi:10.1557/S088376940004608X.
- [69] Z. Wu, J. Zhou, W. Chen, J. Shen, C. Lv, Effects of residual stress on the electrical properties in $\text{PbZr}_{0.52}\text{Ti}_{0.48}\text{O}_3$ thin films, *J. Sol-Gel Sci. Technol.* 75 (2015) 551–556. doi:10.1007/s10971-015-3725-1.
- [70] M.J. Haun, E. Furman, S.J. Jang, L.E. Cross, Thermodynamic theory of the lead zirconate-titanate solid solution system, part I: Phenomenology, *Ferroelectrics*. 99 (1989) 13–25. doi:10.1080/00150198908221436.
- [71] S.S. Sengupta, S.M. Park, D.A. Payne, L.H. Allen, Origins and evolution of stress development in sol-gel derived thin layers and multideposited coatings of lead titanate, *J. Appl. Phys.* 83 (1998) 2291–2296. doi:10.1063/1.366971.
- [72] N. Setter, D. Damjanovic, L. Eng, G. Fox, S. Gevorgian, S. Hong, A. Kingon, H. Kohlstedt, N.Y. Park, G.B. Stephenson, I. Stolitchnov, A.K. TagansteV, D. V. Taylor, T. Yamada, S. Streiffer, *Ferroelectric thin films: Review of materials, properties, and applications*, *J. Appl. Phys.* 100 (2006) 051606. doi:10.1063/1.2336999.
- [73] G.A.C.M. Spierings, G.J.M. Dormans, W.G.J. Moors, M.J.E. Ulenaers, P.K. Larsen, Stresses in $\text{Pt/Pb}(\text{Zr,Ti})\text{O}_3/\text{Pt}$ thin-film stacks for integrated ferroelectric capacitors, *J. Appl. Phys.* 78 (1995) 1926–1933. doi:10.1063/1.360230.
- [74] D.G. Schlom, L. Chen, C. Eom, K.M. Rabe, S.K. Streiffer, J. Triscone, Strain

tuning of ferroelectric thin films, *Annu. Rev. Mater. Res.* 37 (2007) 589–626.
doi:10.1146/annurev.matsci.37.061206.113016.

- [75] B.A. Tuttle, J.A. Voigt, T.J. Garino, D.C. Doodnow, R.W. Schwartz, D.L. Lamppa, T.J. Headley, M.O. Eatough, Chemically prepared Pb(Zr, Ti)O₃ thin films: the effects of orientation and stress, *ISAF '92. Proc. 8th IEEE Int. Symp. Appl. Ferroelectr.* (1992) 344–48. doi:10.1109/ISAF.1992.300703.
- [76] J.S. Speck, A.C. Daykin, A. Seifert, A.E. Romanov, W. Pompe, Domain configurations due to multiple misfit relaxation mechanisms in epitaxial ferroelectric thin films. III. Interfacial defects and domain misorientations, *J. Appl. Phys.* 78 (1995) 1696–1706. doi:10.1063/1.360267.
- [77] K. Lee, S. Baik, Ferroelastic domain structure and switching in epitaxial ferroelectric thin films, *Annu. Rev. Mater. Res.* 36 (2006) 81–116.
doi:10.1146/annurev.matsci.36.090804.094613.
- [78] Fujitsu, *FRAM Guide Book*, 2010.
- [79] A. Pramanick, A.D. Prewitt, J.S. Forrester, J.L. Jones, Domains, Domain Walls and Defects in Perovskite Ferroelectric Oxides: A Review of Present Understanding and Recent Contributions, *Crit. Rev. Solid State Mater. Sci.* 37 (2012) 243–275. doi:10.1080/10408436.2012.686891.
- [80] W. Pompe, X. Gong, Z. Suo, J.S. Speck, Elastic energy release due to domain formation in the strained epitaxy of ferroelectric and ferroelastic films, *J. Appl.*

- Phys. 74 (1993) 6012–6019. doi:10.1063/1.355215.
- [81] E. Hong, R. Smith, S.V. Krishnaswamy, C.B. Freidhoff, S. Trolier-McKinstry, Residual stress development in $\text{Pb}(\text{Zr},\text{Ti})\text{O}_3/\text{ZrO}_2/\text{SiO}_2$ stacks for piezoelectric microactuators, *Thin Solid Films*. 510 (2006) 213–221. doi:10.1016/j.tsf.2005.12.300.
- [82] B. Ma, S. Liu, S. Tong, M. Narayanan, R.E. Koritala, Z. Hu, U. Balachandran, Residual stress of $(\text{Pb}_{0.92}\text{La}_{0.08})(\text{Zr}_{0.52}\text{Ti}_{0.48})\text{O}_3$ films grown by a sol–gel process, *Smart Mater. Struct.* 22 (2013) 055019. doi:10.1088/0964-1726/22/5/055019.
- [83] L.M. Denis, G. Esteves, J. Walker, J.L. Jones, S. Trolier-McKinstry, Thickness dependent response of domain wall motion in declamped $\{001\}$ $\text{Pb}(\text{Zr}_{0.3}\text{Ti}_{0.7})\text{O}_3$ thin films, *Acta Mater.* 151 (2018) 243–252. doi:10.1016/j.actamat.2018.03.046.
- [84] J.I. Yang, R.G. Polcawich, L.M. Sanchez, S. Trolier-Mckinstry, Effect of feature size on dielectric nonlinearity of patterned $\text{PbZr}_{0.52}\text{Ti}_{0.48}\text{O}_3$ films, *J. Appl. Phys.* 117 (2015) 0–7. doi:10.1063/1.4905300.
- [85] K.S. Lee, Y.K. Kim, S. Baik, J. Kim, I.S. Jung, In situ observation of ferroelectric 90° -domain switching in epitaxial $\text{Pb}(\text{Zr}, \text{Ti})\text{O}_3$ thin films by synchrotron x-ray diffraction, *Appl. Phys. Lett.* 79 (2001) 2444–2446. doi:10.1063/1.1406981.
- [86] R.L. Johnson-Wilke, R.H.T. Wilke, M. Wallace, A. Rajashekhar, G. Esteves, Z. Merritt, J.L. Jones, S. Trolier-McKinstry, Ferroelectric/Ferroelastic domain wall motion in dense and porous tetragonal lead zirconate titanate films, *IEEE Trans.*

Ultrason. Ferroelectr. Freq. Control. 62 (2015) 46–55.

doi:10.1109/TUFFC.2014.006562.

- [87] S. Li, A.S. Bhalla, R.E. Newnham, L.E. Cross, C.-Y. Huang, 90 domain reversal in $\text{Pb}(\text{Zr}_x\text{Ti}_{1-x})\text{O}_3$ ceramics, *J. Mater. Sci.* 29 (1994) 1290–1294.

doi:10.1007/BF00975077.

- [88] G. Esteves, M. Wallace, R. Johnson-Wilke, C.M. Fancher, R.H.T. Wilke, S. Trolier-McKinstry, J.L. Jones, Effect of mechanical constraint on domain reorientation in predominantly {111}-textured lead zirconate titanate films, *J. Am. Ceram. Soc.* 99 (2016) 1802–1807. doi:10.1111/jace.14159.

- [89] R. Keech, L. Ye, J.L. Bosse, G. Esteves, J. Guerrier, J.L. Jones, M.A. Kuroda, B.D. Huey, S. Trolier-McKinstry, Declamped Piezoelectric Coefficients in Patterned 70/30 Lead Magnesium Niobate-Lead Titanate Thin Films, *Adv. Funct. Mater.* 27 (2017) 1605014. doi:10.1002/adfm.201605014.

- [90] A. Berger, M. Herwegh, J. Schwarz, B. Putlitz, Quantitative analysis of crystal / grain sizes and their distributions in 2D and 3D, *J. Struct. Geol.* 33 (2011) 1751–1763. doi:10.1016/j.jsg.2011.07.002.

- [91] F.K. Lotgering, Topotactical reactions with ferrimagnetic oxides having hexagonal crystal structures—I, *J. Inorg. Nucl. Chem.* 9 (1959) 113–123. doi:10.1016/0022-1902(59)80070-1.

- [92] A.P. Hammersley, S.O. Svensson, M. Hanfland, A.N. Fitch, D. Hausermann, Two-

- dimensional detector software: From real detector to idealised image or two-theta scan, *High Press. Res.* 14 (1996) 235–248. doi:10.1080/08957959608201408.
- [93] G.. Williamson, W.. Hall, X-ray line broadening from filed aluminium and wolfram, *Acta Metall.* 1 (1953) 22–31. doi:10.1016/0001-6160(53)90006-6.
- [94] J.I. Langford, A.J.C. Wilson, Scherrer after sixty years: a survey and some new results in the determination of crystallite size, *J. Appl. Crystallogr.* 11 (1978) 102–113.
- [95] V. Lantto, J. Lappalainen, M. Kakihana, Phase transitions of $\text{Pb}(\text{Zr}_x\text{Ti}_{1-x})\text{O}_3$ ceramics, *Phys. Rev. B.* 66 (2002) 1–15. doi:10.1103/PhysRevB.66.064108.
- [96] Y. Ehara, S. Yasui, T. Oikawa, T. Shiraishi, T. Shimizu, H. Tanaka, N. Kanenko, R. Maran, T. Yamada, Y. Imai, O. Sakata, N. Valanoor, H. Funakubo, In-situ observation of ultrafast 90° domain switching under application of an electric field in (100)/(001)-oriented tetragonal epitaxial $\text{Pb}(\text{Zr}_{0.4}\text{Ti}_{0.6})\text{O}_3$ thin films, *Sci. Rep.* 7 (2017) 1–7. doi:10.1038/s41598-017-09389-6.
- [97] E.B. Araújo, B.O. Nahime, M. Melo, F. Dinelli, F. Tantussi, P. Baschieri, F. Fuso, M. Allegrini, Processing and structural properties of random oriented lead lanthanum zirconate titanate thin films, *Mater. Res. Bull.* 61 (2015) 26–31. doi:10.1016/j.materresbull.2014.09.055.
- [98] J. Lappalainen, V. Lantto, J. Frantti, J. Hiltunen, X-ray diffraction and Raman investigations of thickness dependent stress effects on $\text{Pb}(\text{Zr}_x\text{Ti}_{1-x})\text{O}_3$ thin films,

- Appl. Phys. Lett. 88 (2006) 252901. doi:10.1063/1.2216895.
- [99] J.S. Pulskamp, A. Wickenden, R. Polcawich, B. Piekarski, M. Dubey, G. Smith, Mitigation of residual film stress deformation in multilayer microelectromechanical systems cantilever devices, *J. Vac. Sci. Technol. B Microelectron. Nanom. Struct.* 21 (2003) 2482. doi:10.1116/1.1615982.
- [100] M. Olfatnia, T. Xu, L.S. Ong, J.M. Miao, Z.H. Wang, Investigation of residual stress and its effects on the vibrational characteristics of piezoelectric-based multilayered microdiaphragms, *J. Micromechanics Microengineering.* 20 (2010) 015007. doi:10.1088/0960-1317/20/1/015007.
- [101] M.F. Doerner, W.D. Nix, Stresses and deformation processes in thin films on substrates, *CRC Crit. Rev. Solid State Mater. Sci.* 14 (1988) 225–268.
- [102] W. Fang, J.A. Wickert, Determining mean and gradient residual stresses in thin films using micromachined cantilevers, *J. Micromechanics Microengineering.* 6 (1996) 301–309. doi:10.1088/0960-1317/6/3/002.
- [103] C.Q. Guo, Z.L. Pei, D. Fan, R.D. Liu, J. Gong, C. Sun, Predicting multilayer film's residual stress from its monolayers, *Mater. Des.* 110 (2016) 858–864. doi:10.1016/j.matdes.2016.08.053.
- [104] E. Zakar, R. Polcawich, M. Dubey, J. Pulskamp, B. Piekarski, J. Conrad, R. Piekarz, Stress analysis of SiO₂/Ta/Pt/PZT/Pt stack for MEMS application, in: ISAF 2000. Proc. 2000 12th IEEE Int. Symp. Appl. Ferroelectr. (IEEE Cat.

No.00CH37076), IEEE, n.d.: pp. 757–759. doi:10.1109/ISAF.2000.942430.

- [105] J.L. Jones, J.M. LeBeau, J. Nikkel, A.A. Oni, J.H. Dycus, C. Cozzan, F. Lin, A. Chernatynskiy, J.C. Nino, S.B. Sinnott, S. Mhin, G.L. Brennecka, J. Ihlefeld, Combined experimental and computational methods reveal the evolution of buried interfaces during synthesis of ferroelectric thin films, *Adv. Mater. Interfaces*. 2 (2015) 1500181. doi:10.1002/admi.201500181.
- [106] Y. Bastani, N. Bassiri-Gharb, Enhanced dielectric and piezoelectric response in PZT superlattice-like films by leveraging spontaneous Zr/Ti gradient formation, *Acta Mater.* 60 (2012) 1346–1352. doi:10.1016/j.actamat.2011.11.030.
- [107] J.E. Sader, Surface stress induced deflections of cantilever plates with applications to the atomic force microscope: V-shaped plates, *J. Appl. Phys.* 91 (2002) 9354–9361. doi:10.1063/1.1470240.
- [108] F. Fachin, S.A. Nikles, J. Dugundji, B.L. Wardle, Analytical extraction of residual stresses and gradients in MEMS structures with application to CMOS-layered materials, *J. Micromechanics Microengineering*. 21 (2011) 095017. doi:10.1088/0960-1317/21/9/095017.
- [109] V. Ziebart, O. Paul, H. Baltes, Strongly buckled square micromachined membranes, *J. Microelectromechanical Syst.* 8 (1999) 423–432. doi:10.1109/84.809057.
- [110] D.C.C. Lam, F. Yang, A.C.M. Chong, J. Wang, P. Tong, Experiments and theory

in strain gradient elasticity, *J. Mech. Phys. Solids*. 51 (2003) 1477–1508.
doi:10.1016/S0022-5096(03)00053-X.

[111] N.H. Zhang, W.L. Meng, E.C. Aifantis, Elastic bending analysis of bilayered beams containing a gradient layer by an alternative two-variable method, *Compos. Struct.* 93 (2011) 3130–3139. doi:10.1016/j.compstruct.2011.06.019.

[112] M.J. Lachut, J.E. Sader, Buckling of a cantilever plate uniformly loaded in its plane with applications to surface stress and thermal loads, *J. Appl. Phys.* 113 (2013) 024501. doi:10.1063/1.4772745.

[113] Y. Wyser, C. Pelletier, J. Lange, Predicting and determining the bending stiffness of thin films and laminates, *Packag. Technol. Sci.* 14 (2001) 97–108.
doi:10.1002/pts.540.

[114] J.R. Looker, J.E. Sader, Flexural Resonant Frequencies of Thin Rectangular Cantilever Plates, *J. Appl. Mech.* 75 (2008) 011007. doi:10.1115/1.2745377.

[115] F. Yang, A.C.M. Chong, D.C.C. Lam, P. Tong, Couple stress based strain gradient theory for elasticity, *Int. J. Solids Struct.* 39 (2002) 2731–2743.
doi:10.1016/S0020-7683(02)00152-X.

[116] N.A. Fleck, G.M. Muller, M.F. Ashby, J.W. Hutchinson, Strain gradient plasticity: Theory and experiment, *Acta Metall. Mater.* 42 (1994) 475–487.
doi:10.1016/0956-7151(94)90502-9.

[117] M.T. Kim, Influence of substrates on the elastic reaction of films for the

microindentation tests, 283 (1996) 12–16.

- [118] T.P. Weihs, S. Hong, J.C. Bravman, W.D. Nix, Mechanical deflection of cantilever microbeams: A new technique for testing the mechanical properties of thin films, *J. Mater. Res.* 3 (1988) 931–942. doi:10.1557/JMR.1988.0931.
- [119] D. Das, L. Sanchez, J. Martin, B. Power, S. Isaacson, R.G. Polcawich, I. Chasiotis, Control of mechanical response of freestanding $\text{PbZr}_{0.52}\text{Ti}_{0.48}\text{O}_3$ films through texture, *Appl. Phys. Lett.* 109 (2016) 131905. doi:10.1063/1.4963348.
- [120] W. Kreider, A.H. Nayfeh, Experimental investigation of single-mode responses in a fixed-fixed buckled beam, *Nonlinear Dyn.* 15 (1998) 155–177.
<https://doi.org/10.1023/A:1008231012968>.
- [121] K.R. Oldham, J.S. Pulskamp, R.G. Polcawich, M. Dubey, Thin-film PZT lateral actuators with extended stroke, *J. Microelectromechanical Syst.* 17 (2008) 890–899. doi:10.1109/JMEMS.2008.927177.
- [122] N. Ledermann, P. Murali, J. Baborowski, S. Gentil, K. Mukati, M. Cantoni, A. Seifert, N. Setter, {100}-Textured, piezoelectric $\text{Pb}(\text{Zr}_x\text{Ti}_{1-x})\text{O}_3$ thin films for MEMS: integration, deposition and properties, *Sensors Actuators A Phys.* 105 (2003) 162–170. doi:10.1016/S0924-4247(03)00090-6.
- [123] D.M. Potrepka, M. Rivas, H. Yu, M. Aindow, G.R. Fox, R.G. Polcawich, Effect of IrO_2/Pt , IrO_2 , and Pt bottom electrodes on the structure and electrical properties of PZT based piezoelectric microelectromechanical system devices, *J. Mater. Sci.*

- Mater. Electron. 29 (2018) 11367–11377. doi:10.1007/s10854-018-9224-8.
- [124] COMSOL Multiphysics, (2018). www.comsol.com.
- [125] M. Rivas, Iridium oxide (IrO₂) as a top electrode for ferroelectric micro-electro-mechanical systems (MEMS) devices for radiation rich environments, 2018.
- [126] S. Yagnamurthy, I. Chasiotis, J. Lambros, R.G. Polcawich, J.S. Pulskamp, M. Dubey, Mechanical and ferroelectric behavior of PZT-based thin films, J. Microelectromechanical Syst. 20 (2011) 1250–1258. doi:10.1109/JMEMS.2011.2167666.
- [127] K.N. Jonnalagadda, I. Chasiotis, S. Yagnamurthy, J. Lambros, J. Pulskamp, R. Polcawich, M. Dubey, Experimental investigation of strain rate dependence of nanocrystalline Pt films, Exp. Mech. 50 (2010) 25–35. doi:10.1007/s11340-008-9212-7.
- [128] A. Adami, M. Decarli, R. Bartali, V. Micheli, N. Laidani, L. Lorenzelli, Mechanical characterization of thin TiO₂ films by means of microelectromechanical systems-based cantilevers, Rev. Sci. Instrum. 81 (2010) 015109. doi:10.1063/1.3292942.
- [129] C. Ottermann, J. Otto, U. Jeschkowski, O. Anderson, M. Heming, K. Bange, Stress of TiO₂ thin films produced by different deposition techniques, MRS Proc. 308 (1993) 69. doi:10.1557/PROC-308-69.
- [130] K.E. Petersen, Silicon as a mechanical material, Proc. IEEE. 70 (1982) 420–457.

doi:10.1109/PROC.1982.12331.

- [131] Y. Okada, Y. Tokumaru, Precise determination of lattice parameter and thermal expansion coefficient of silicon between 300 and 1500 K, *J. Appl. Phys.* 56 (1984) 314–320. doi:10.1063/1.333965.
- [132] C. Tsou, Y.S. Huang, H.C. Chang, On the determination of thermal expansion coefficient of thermal oxide, *NSTI-Nanotech.* 3 (2005) 339–342.
doi:10.1617/2912143632.021.
- [133] Institute Fur Struktur-Und Funktionskeramic, Classical Laminate Theory (CLT), (n.d.). <http://www.isfk.at/de/1428/>.
- [134] W.R. Cook, D.A. Berlincourt, F.J. Scholz, Thermal expansion and pyroelectricity in lead titanate zirconate and barium titanate, *J. Appl. Phys.* 34 (1963) 1392–1398.
doi:10.1063/1.1729587.
- [135] H. Tada, A.E. Kumpel, R.E. Lathrop, J.B. Slanina, P. Nieva, P. Zavracky, I.N. Miaoulis, P.Y. Wong, Thermal expansion coefficient of polycrystalline silicon and silicon dioxide thin films at high temperatures, *J. Appl. Phys.* 87 (2000) 4189–4193. doi:10.1063/1.373050.
- [136] W. Fang, C.-H. Lee, H.-H. Hu, On the buckling behavior of micromachined beams, *J. Micromechanics Microengineering.* 9 (1999) 236–244.
doi:10.1088/0960-1317/9/3/304.
- [137] R. Keech, S. Shetty, M.A. Kuroda, X. Hu Liu, G.J. Martyna, D.M. Newns, S.

- Trolier-McKinstry, Lateral scaling of $\text{Pb}(\text{Mg}_{1/3}\text{Nb}_{2/3})\text{O}_3\text{-PbTiO}_3$ thin films for piezoelectric logic applications, *J. Appl. Phys.* 115 (2014). doi:10.1063/1.4882025.
- [138] G. Abadias, E. Chason, J. Keckes, M. Sebastiani, G.B. Thompson, E. Barthel, G.L. Doll, C.E. Murray, C.H. Stoessel, L. Martinu, Review article: stress in thin films and coatings: current status, challenges, and prospects, *J. Vac. Sci. Technol. A Vacuum, Surfaces, Film.* 36 (2018) 020801. doi:10.1116/1.5011790.
- [139] A.M. Korsunsky, J. Guénoilé, E. Salvati, T. Sui, M. Mousavi, A. Prakash, E. Bitzek, Quantifying eigenstrain distributions induced by focused ion beam damage in silicon, *Mater. Lett.* 185 (2016) 47–49. doi:10.1016/j.matlet.2016.08.111.
- [140] U. Pietsch, H. Metzger, S. Rugel, B. Jenichen, I.K. Robinson, Depth-resolved measurement of lattice relaxation in $\text{Ga}_{1-x}\text{In}_x\text{As}/\text{GaAs}$ strained layer superlattices by means of grazing-incidence x-ray diffraction, *J. Appl. Phys.* 74 (1993) 2381–2387. doi:10.1063/1.354724.
- [141] E.A. Kondrashkina, S.A. Stepanov, M. Schmidbauer, R. Opitz, R. Köhler, H. Rhan, High-resolution grazing-incidence x-ray diffraction for characterization of defects in crystal surface layers, *J. Appl. Phys.* 81 (1997) 175–183. doi:10.1063/1.363838.
- [142] P. Colombi, P. Zanola, E. Bontempi, R. Roberti, M. Gelfi, L.E. Depero, Glancing-incidence X-ray diffraction for depth profiling of polycrystalline layers, *J. Appl. Crystallogr.* 39 (2006) 176–179. doi:10.1107/S0021889805042779.

- [143] M.B. Kelman, P.C. McIntyre, B.C. Hendrix, S.M. Bilodeau, J.F. Roeder, S. Brennan, Structural analysis of coexisting tetragonal and rhombohedral phases in polycrystalline $\text{Pb}(\text{Zr}_{0.35}\text{Ti}_{0.65})\text{O}_3$ thin films, *J. Mater. Res.* 18 (2003) 173–179. doi:10.1557/JMR.2003.0024.
- [144] C. Zhu, X. Niu, Y. Fu, N. Li, C. Hu, Y. Chen, X. He, G. Na, P. Liu, H. Zai, Y. Ge, Y. Lu, X. Ke, Y. Bai, S. Yang, P. Chen, Y. Li, M. Sui, L. Zhang, H. Zhou, Q. Chen, Strain engineering in perovskite solar cells and its impacts on carrier dynamics, *Nat. Commun.* 10 (2019). doi:10.1038/s41467-019-08507-4.
- [145] A.E. Maniadaki, G. Kopidakis, I.N. Remediakis, Strain engineering of electronic properties of transition metal dichalcogenide monolayers, *Solid State Commun.* 227 (2016) 33–39. doi:10.1016/j.ssc.2015.11.017.
- [146] S.O. Hruszkewycz, C.M. Folkman, M.J. Highland, M. V. Holt, S.H. Baek, S.K. Streiffer, P. Baldo, C.B. Eom, P.H. Fuoss, X-ray nanodiffraction of tilted domains in a poled epitaxial BiFeO_3 thin film, *Appl. Phys. Lett.* 99 (2011) 232903. doi:10.1063/1.3665627.
- [147] M. Schmidbauer, M. Hanke, A. Kwasniewski, D. Braun, L. von Helden, C. Feldt, S.J. Leake, J. Schwarzkopf, Scanning X-ray nanodiffraction from ferroelectric domains in strained $\text{K}_{0.75}\text{Na}_{0.25}\text{NbO}_3$ epitaxial films grown on (110) TbScO_3 , *J. Appl. Crystallogr.* 50 (2017) 519–524. doi:10.1107/S1600576717000905.
- [148] N.I. Khamidy, V. Kovacova, A. Bernasconi, G. Le Rhun, N. Vaxelaire, In situ 2D

- diffraction as a tool to characterize ferroelectric and piezoelectric thin films, *Mater. Res. Express.* 4 (2017) 084002. doi:10.1088/2053-1591/aa5e5a.
- [149] M. Bartosik, R. Daniel, C. Mitterer, I. Matko, M. Burghammer, P.H. Mayrhofer, J. Keckes, Cross-sectional X-ray nanobeam diffraction analysis of a compositionally graded CrN_x thin film, *Thin Solid Films.* 542 (2013) 1–4.
doi:10.1016/j.tsf.2013.05.102.
- [150] J. Keckes, M. Bartosik, R. Daniel, C. Mitterer, G. Maier, W. Ecker, J. Vila-Comamala, C. David, S. Schoeder, M. Burghammer, X-ray nanodiffraction reveals strain and microstructure evolution in nanocrystalline thin films, *Scr. Mater.* 67 (2012) 748–751. doi:10.1016/j.scriptamat.2012.07.034.
- [151] M. Stefenelli, J. Todt, A. Riedl, W. Ecker, T. Müller, R. Daniel, M. Burghammer, J. Keckes, X-ray analysis of residual stress gradients in TiN coatings by a Laplace space approach and cross-sectional nanodiffraction: a critical comparison, *J. Appl. Crystallogr.* 46 (2013) 1378–1385. doi:10.1107/S0021889813019535.
- [152] N. Jäger, S. Klima, H. Hruby, J. Julin, M. Burghammer, J.F. Keckes, C. Mitterer, R. Daniel, Evolution of structure and residual stress of a FCC/hex-AlCrN multilayered system upon thermal loading revealed by cross-sectional X-ray nanodiffraction, *Acta Mater.* 162 (2019) 55–66. doi:10.1016/j.actamat.2018.09.031.
- [153] A. Zeilinger, J. Todt, C. Krywka, M. Müller, W. Ecker, B. Sartory, M. Meindlhumer, M. Stefenelli, R. Daniel, C. Mitterer, J. Keckes, In-situ observation

of cross-sectional microstructural changes and stress distributions in fracturing TiN thin film during nanoindentation, *Nat. Publ. Gr.* (2016) 1–14.

doi:10.1038/srep22670.

[154] S.J.B. Kurz, S.R. Meka, N. Schell, W. Ecker, J. Keckes, E.J. Mittemeijer, Residual stress and microstructure depth gradients in nitrided iron-based alloys revealed by dynamical cross-sectional transmission X-ray microdiffraction, *Acta Mater.* 87 (2015) 100–110. doi:10.1016/j.actamat.2014.12.048.

[155] H. Simons, A.C. Jakobsen, S.R. Ahl, C. Detlefs, H.F. Poulsen, Multiscale 3D characterization with dark-field x-ray microscopy, *MRS Bull.* 41 (2016) 454–459. doi:10.1557/mrs.2016.114.

[156] H. Simons, S.R. Ahl, A.C. Jakobsen, C. Yildirim, P.K. Cook, C. Detlefs, H.F. Poulsen, Multi-scale 3D imaging of strain and structure with dark-field X-ray microscopy, *Microsc. Microanal.* 24 (2018) 72–75. doi:10.1017/s1431927618012758.

[157] H. Simons, A. King, W. Ludwig, C. Detlefs, W. Pantleon, S. Schmidt, F. Stöhr, I. Snigireva, A. Snigirev, H.F. Poulsen, Dark-field X-ray microscopy for multiscale structural characterization, *Nat. Commun.* 6 (2015) 6098. doi:10.1038/ncomms7098.

[158] K.T. Murray, A.F. Pedersen, I. Mohacsi, C. Detlefs, A.J. Morgan, M. Prasciolu, C. Yildirim, H. Simons, A.C. Jakobsen, H.N. Chapman, H.F. Poulsen, S. Bajt,

Multilayer Laue lenses at high X-ray energies: performance and applications, *Opt. Express*. 27 (2019) 7120. doi:10.1364/OE.27.007120.

- [159] D.M. Marincel, S. Troler-mckinstry, THE INFLUENCE OF CRYSTAL DEFECTS ON DOMAIN WALL MOTION IN THIN FILM $\text{Pb}(\text{Zr}, \text{Ti})\text{O}_3$ by, PSU, 2014. [http://www.mri.psu.edu/faculty/STM/Student theses/Marincel-Dissertation-Final.pdf](http://www.mri.psu.edu/faculty/STM/Student%20theses/Marincel-Dissertation-Final.pdf).
- [160] G.A. Rossetti, A.G. Khachatryan, Inherent nanoscale structural instabilities near morphotropic boundaries in ferroelectric solid solutions, *Appl. Phys. Lett.* 91 (2007) 072909. doi:10.1063/1.2771095.
- [161] A.Y. Emelyanov, N.A. Pertsev, S. Hoffmann-eifert, U. Bottger, R. Waser, Grain-boundary effect on the curie-weiss law of ferroelectric ceramics and polycrystalline thin films: calculation by the method of effective medium, *J. Electroceramics*. 9 (2002) 5–16.
- [162] W.Y. Park, C.S. Hwang, Film-thickness-dependent Curie-Weiss behavior of thin-film capacitors having Pt electrodes, *Appl. Phys. Lett.* 85 (2004) 5313. doi:10.1063/1.1828583.

Appendix

Matlab Codes for Data Processing

A.1. Capacitor in Series Seed Layer Correction

```
function [Out] = RayleighSeedCorrection(x,y,freq,t,afilm,aseed,minpts,maxpts,maxi)
% x is the file name for the sample of interest that needs correction
% y is the file name for the seed sample
% afilm is the surface area of the electrode on the film
% aseed is the surface area of the electrode on the seed which may be different
f1=find(x.swp.FREQUENCY_set==freq);
f2=find(y.swp.FREQUENCY_set==freq);
M1=[x.swp.AC_set,x.meas.CD0.real(:,1:3,f1)];
M2=[y.swp.AC_set,y.meas.CD0.real(:,1:3,f2)];

% convert numerical array to dataset array stored in matlab
Out.film = mat2dataset(M1);
film = Out.film;
Out.seed = mat2dataset(M2);
seed = Out.seed;

% Calculate dielectric constants 'totalk' meaning the dielectric (k) of the film before the
correction
% Calculate dielectroc constant 'seedk' meaning the dielectric (k) of the seed layer
for i=1:30;
    totalk(i,1)=(film{i,2}*(t*10^-6))/(8.854e-12*(afilm*10^-4));
    totalk(i,2)=(film{i,3}*(t*10^-6))/(8.854e-12*(afilm*10^-4));
    totalk(i,3)=(film{i,4}*(t*10^-6))/(8.854e-12*(afilm*10^-4));
end
Out.totalk=totalk;
% Calculate dielectric constants 'totalk' meaning the dielectric (k) of the film before the
correction
% Calculate dielectroc constant 'seedk' meaning the dielectric (k) of the seed layer
for i=1:30;
    seedk(i,1)=(seed{i,2}*(0.057*10^-6))/(8.854e-12*(aseed*10^-4));
    seedk(i,2)=(seed{i,3}*(0.057*10^-6))/(8.854e-12*(aseed*10^-4));
    seedk(i,3)=(seed{i,4}*(0.057*10^-6))/(8.854e-12*(aseed*10^-4));
end
Out.seedk=seedk;
% correct the dielectric constant of the film using capacitor in series model
% the two capacitors in series are the seed layer (1% Mn doped) and the rest of the
film(2% Nb doped)
% new film represents the new matrix that has the corrected capacitance of the film
for i=1:30;
    newfilm(i,1)=film{i,1}*10/t; % applied field on film (not seed)
```

```

newfilm(i,2)=(t-0.06)*totalk(i,1)*seedk(i,1)/((t*seedk(i,1))-(0.06*totalk(i,1)));
newfilm(i,3)=(t-0.06)*totalk(i,2)*seedk(i,2)/((t*seedk(i,2))-(0.06*totalk(i,2)));
newfilm(i,4)=(t-0.06)*totalk(i,3)*seedk(i,3)/((t*seedk(i,3))-(0.06*totalk(i,3)));
end
Out.newfilm = newfilm;

%Create variables
E = newfilm(:,1);
newk1 = newfilm(:,2);
newk2 = newfilm(:,3);
newk3 = newfilm(:,4);
newk23 = (newk2+newk3)/2;

%Input sample parameters
t = input('How thick is your sample (microns):');
a = input('How big is your contact (cm^2):');
mini = input('What point do you wish to start at:');

%Find number of data points
n=numel(newk2);

%Create variable placeholders that will be worse than first fit
bestslopediff=1000;
bestslope=1;
bestrsq=0;
X=[E,ones(size(E))];

%Start fit from specified to point 12.
for i=1:maxi,

    %End fit from point 15 to the last data point.
    for j=round(maxi/2):n,

        %While minimum number of points is true.
        if abs(j-i)>=minpts && j>i && abs(j-i)<=maxpts

            %Calculate fit from i:j for run 2
            [b2,b2int,r2,r2int,stats2]=regress(newk2(i:j),X(i:j,:));
            %Calculate fit from i:j for run 3
            [b3,b3int,r3,r3int,stats3]=regress(newk3(i:j),X(i:j,:));

            %See if average R^2 is better than existing average R^2
            if bestrsq < (stats3(1)+stats2(1))/2

                %Check if difference in slope over average slope is smaller than
                %the existing best difference
                %if (bestslopediff/bestslope) > ((abs(p3(1)-p2(1)))/((p3(1)+p2(1))/2)),

```

```

    %Apply values to new best
    bestslopediff=abs(b2(1)-b3(1));
    besti=i;
    bestj=j;
    bestslope=(b3(1)+b2(1))/2;
    bestrsq=(stats2(1)+stats3(1))/2;
    bestint=(b3(2)+b2(2))/2;
    bestconf=(b3int+b2int)/2;
    %end

end
end
end

end
bestconfinterval=(bestconf(:,2)-bestconf(:,1))/2;

% Write out the values
disp(['Best i: ' num2str(besti)])
disp(['Best j: ' num2str(bestj)])
disp(['Best average slope (cm/kV): ' num2str(bestslope)])
disp(['Best average intercept: ' num2str(bestint)])
disp(['Best average R^2: ' num2str(bestrsq)])
disp(['Best confidence interval (95%): '])
bestconfinterval
%Recalculate fits for run 2 and 3 using best i and j values
p2=polyfit(E(besti:bestj),newk2(besti:bestj),1);
p3=polyfit(E(besti:bestj),newk3(besti:bestj),1);

% Average the two slopes and intercepts
plotp=(p2+p3)/2;

%Clear Plot
clf
%Plot data
plot(E,newk2,'.',E,newk3,'.'),
hold on;
%Plot best fit line
plot(E,polyval(plotp,linspace(E(1),E(n),n)),'-')
hold on;
%Plot bounds of best fit line
plot(E(besti),newk2(besti),'rs',E(bestj),newk2(bestj),'rs','MarkerSize',15)
%Labels
legend('Run 2','Run 3','Best fit','Fit Bounds')
xlabel('Electric Field (kV/cm)'), ylabel('Dielectric Constant')
title('Rayleigh data fitting')

end

```

A.2. Rayleigh Analysis for Large Frequency Sweeps

```

function [Out] = Rayleigh(x,freq,t,a,minpts,maxpts,maxi)
f=find(x.swp.FREQUENCY_set==freq);
M=[x.swp.AC_set,x.meas.CD0.real(:,1:3,f)];

%Transpose matrix
dim=size(M);
if dim(1) < dim(2),
    M=M.';
end

%Create variables
V = M(:,1);
C1 = M(:,2);
C2 = M(:,3);
C3 = M(:,4);

%Input sample parameters
%t = input('How thick is your sample (microns):');
%a = input('How big is your contact (cm^2):');
%mini = input('What point do you wish to start at:');

%Calculate field and dielectric constants
E=V*10/t;
k1=(C1*(t*10^-6))/(8.854e-12*(a*10^-4));
k2=(C2*(t*10^-6))/(8.854e-12*(a*10^-4));
k3=(C3*(t*10^-6))/(8.854e-12*(a*10^-4));
k23=(k2+k3)/2;

%Find number of data points
n=numel(k2);

%Create variable placeholders that will be worse than first fit
bestslopediff=1000;
bestslope=1;
bestrsq=0;
X=[E,ones(size(E))];
%Start fit from specified to point 12.
for i=1:maxi,

    %End fit from point 15 to the last data point.
    for j=round(maxi/2):n,

        %While minimum number of points is true.

```

```

if abs(j-i)>=minpts && j>i && abs(j-i)<=maxpts

    %Calculate fit for run 2
    [b2,b2int,r2,r2int,stats2]=regress(k2(i:j),X(i:j,:));
    %Calculate fit for run 3
    [b3,b3int,r3,r3int,stats3]=regress(k3(i:j),X(i:j,:));

    %See if average R^2 is better than existing average R^2
    if bestrsq < (stats3(1)+stats2(1))/2

        %Apply values to new best
        bestslopediff=abs(b2(1)-b3(1));
        besti=i;
        bestj=j;
        bestslope=(b3(1)+b2(1))/2;
        bestrsq=(stats2(1)+stats3(1))/2;
        bestint=(b3(2)+b2(2))/2;
        bestconf=(b3int+b2int)/2;
        %end

    end
end
end

end
bestconfinterval=(bestconf(:,2)-bestconf(:,1))/2;

% Write out the values
disp(['Best i: ' num2str(besti)])
disp(['Best j: ' num2str(bestj)])
disp(['Best average slope (cm/kV): ' num2str(bestslope)])
disp(['Best average intercept: ' num2str(bestint)])
disp(['Best average R^2: ' num2str(bestrsq)])
disp(['Best confidence interval (95%): '])
bestconfinterval
%Recalculate fits for run 2 and 3 using best i and j values
p2=polyfit(E(besti:bestj),k2(besti:bestj),1);
p3=polyfit(E(besti:bestj),k3(besti:bestj),1);

% Average the two slopes and intercepts
plotp=(p2+p3)/2;

% Clear Plot
clf
%Plot data
plot(E,k2,'.',E,k3,'.'),
hold on;
%Plot best fit line

```

```

plot(E,polyval(plotp,linspace(E(1),E(n),n)),'-')
hold on;
%Plot bounds of best fit line
plot(E(besti),k2(besti),'rs',E(bestj),k2(bestj),'rs','MarkerSize',15)
%Labels
legend('Run 2','Run 3','Best fit','Fit Bounds')
xlabel('Electric Field (kV/cm)'), ylabel('Dielectric Constant')
title('Rayleigh data fitting')

Out=[E,k1,k2,k3,k23]

```

A.3. File Conversion to Matlab Files from .diel

```

function dat=diel2mat()
% Get file path and names
[file_name,load_path]=uigetfile('*.diel','Load Gadd File','C:/path');
load_name = file_name;
% Load .diel File
filename = [load_path load_name];
fileID = fopen([load_path load_name]);
textt = fgetl(fileID);
dat.name = filename;
% Import Program (Sweeps and Measurements)

for i = 1:1:3
    textt = fgetl(fileID);
end

i=1;
j=1;
n(1)=1;
dat.swp.none = [1];
name{1}='none';

while strcmp(textt,'*****') == 0
    if strcmp(textt,'SWEEP') == 1
        j = j+1;
        textt = fgetl(fileID);
        name{j} = strtok(textt, char(9));
        sweep_vals = str2num(fgetl(fileID));
        [u,v] = size(sweep_vals);
        dat.swp.(name{j}) = reshape(sweep_vals,v,u);
        n(j) = size(dat.swp.(name{j}),1);
    elseif strcmp(textt,'ENDSWEEP') == 1
        j = j-1;
    else
        names.tot(i) = {textt};
        i=i+1;
    end
end

```

```

[tok,remain] = strtok(textt);
dat.meas.(strtrim(remain)).type = tok;
if j>1
    dat.meas.(strtrim(remain)).size = flipdim(n(2:j),2);
    dat.meas.(strtrim(remain)).swp = flipdim(name(2:j),2);
else
    dat.meas.(strtrim(remain)).size = n(1:j);
    dat.meas.(strtrim(remain)).swp = name(1:j);
end
val.(strtrim(remain)) = [];
end

textt = fgetl(fileID);
end

% Import Data

while strcmp(textt, '*****') == 0
    textt = fgetl(fileID);
end

textt = fgetl(fileID);

while textt ~= -1
    [~,remain] = strtok(textt);
    val.(strtrim(remain)) = vertcat(val.(strtrim(remain)),str2num(fgetl(fileID)));
    textt = fgetl(fileID);
end

fclose('all');

% Sort Data

names.meas = fieldnames(dat.meas);
num_var = size(names.meas);

for i = 1:1:num_var
    j = size(val.(names.meas{i}),1);
    k = dat.meas.(names.meas{i}).size;
    if numel(k) == 1
        k = [k 1];
    end

    if strcmp(dat.meas.(names.meas{i}).type, 'REAL') == 1
        if prod(k) == j
            dat.meas.(names.meas{i}).real = reshape(val.(names.meas{i}),k);
        else
            dat.meas.(names.meas{i}).real = val.(names.meas{i});
        end
    end
end

```

```
else
    if prod(k) == j
        dat.meas.(names.meas{i}).real = reshape(val.(names.meas{i})(:,1),k);
        dat.meas.(names.meas{i}).imag = reshape(val.(names.meas{i})(:,2),k);
    else
        dat.meas.(names.meas{i}).real = val.(names.meas{i})(:,1);
        dat.meas.(names.meas{i}).imag = val.(names.meas{i})(:,2);
    end
end
end
end

% Save Data Structure as .mat

save([filename '.mat'],'dat');
end
```

VITA

Lyndsey M. Denis

Lyndsey Michele Denis was born on February 2nd, 1991 in Orlando, Florida to Francisco and Donna Denis. Lyndsey grew up in Altamonte Springs, Florida with her younger brother, Brandon Denis. Starting in 2009, she attended the University of Florida in Gainesville, Florida to pursue a bachelor of science in Chemical Engineering. Two weeks after graduation, she started her Ph.D. studies in Materials Science and Engineering at the Pennsylvania State University under the guidance of Professor Susan Trolier-McKinstry. Outside of research and her studies, Lyndsey enjoys a variety of hobbies including cooking, baking, salsa dancing, glass blowing, painting, hiking, swimming, board games and traveling. Upon graduation, she will be joining Dr. Peter Finkel's research group in the Materials Science and Technology Division at the Naval Research Laboratory in Washington, D.C. studying the electric field and temperature induced phase transition in PIN-PMN-PT single crystals and strain coupled magnetoelectric switching in ferromagnetic-ferroelectric composites.